

NEURAL MODELING CASE STUDIES AT BIOPHYSICAL,
MACHINE LEARNING, AND AUTOMATION LEVELS

A Dissertation presented to
The Faculty of the Graduate School
University of Missouri – Columbia

In Partial Fulfillment
of the Requirement for the Degree
Doctor of Philosophy

by
TYLER J. BANKS

Dr. Satish S. Nair, Dissertation Supervisor

DECEMBER 2023

The undersigned, appointed by the dean of the Graduate School, have examined the dissertation entitled

**NEURAL MODELING CASE STUDIES AT BIOPHYSICAL, MACHINE LEARNING
AND AUTOMATION LEVELS**

Presented by Tyler Banks,

A candidate for the degree of Doctor of Philosophy,

And hereby certify that, in their opinion, it is worthy of acceptance.

Professor Satish S. Nair

Professor Jianlin Cheng

Professor Dominic Ho

Professor Jeffrey Scherrer

Professor Petros Veletas

ACKNOWLEDGEMENTS

I would like to first thank my family: Sam, Morgan, Noah, Elijah, Mom, Dad, Jonathan, Nicolas, Joshua, Alyssa, Grandma Jill, Grandpa Roger, Grandma Sandy and Great Grandma Dee for their unconditional love and support. This has been a long, and sometimes difficult process, and I thank you for everything over the years. I do all of this with you in mind. I also thank Christopher Knutson for his friendship and motivation.

I would like to send a special thanks to my dissertation advisor Dr. Nair. You are more than my advisor, but also a friend. I appreciate the patience you've shown with me and all the wisdom you've imparted to me. Thank you.

I also thank lab mates, Ben Latimer, Feng Feng, Greg Glickert, Vladimir (Walt) Omelyusik, and Ziao Chen. It has been a pleasure to work with all of you.

I thank all of those who served as an advisor and/or mentor during my research. Specifically, Dr. Scherrer and Dr. Uhlmann. A special thanks to my committee members Dr. Cheng, Dr. Ho and Dr. Valettas for taking the time out to review my research.

TABLE OF CONTENTS

ACKNOWLEDGMENTS	ii
LIST OF FIGURES	v
ABSTRACT	vi
CHAPTER 1: INTRODUCTION AND OBJECTIVES	1
1.1 Background and Motivation	1
1.2 Chapter Overview	1
CHAPTER 2: PREDICTING OPIOID USE DISORDER BEFORE AND AFTER THE OPIOID PRESCRIBING PEAK IN THE UNITED STATES: A MACHINE LEARNING TOOL USING ELECTRONIC HEALTHCARE RECORDS ...	3
2.1 Introduction	4
2.2 Methods	7
2.3 Results	17
2.4 Discussion	28
2.5 Conclusions	31
2.6 References	32
CHAPTER 3: ANATOMICAL AND COMPUTATIONAL INVESTIGATION OF BASAL FOREBRAIN INNERVATION OF THE AMYGDALA	35
3.1 Introduction	36
3.2 Materials and Method	39
3.3 Results	56
3.4 Discussion	72
3.5 Conclusions	76
3.6 Tables	79

3.7 References	83
CHAPTER 4: PIPELINE FOR BIOPHYSICAL MODELING OF A LARGE CLASS OF NEURONS	90
4.1 Introduction	92
4.2 Methods	96
4.3 Results	104
4.4 Discussion and Conclusion	111
4.5 References	116
4.6 Tables	117
4.7 Figures	120
CHAPTER 5: SUMMARY, CONTRIBUTIONS, AND FUTURE WORK	125
PUBLICATIONS	127
VITA	129

LIST OF FIGURES

Figure	Page
2.1 Eligibility criteria for Veterans Heath Administration patient population	9
2.2 Relative AUC score using a subset of dataset-1 on the deep neural network classifier.....	14
2.3 Feature importance stratified by age, using random forest classifier for dataset 1	23
2.4 Feature importance stratified by age, using random forest classifier for dataset-2	24
3.1 Retrobead injections and resulting retrograde labeling in the basal forebrain and preoptic nuclei	58
3.2 Confocal microscopic images of retrogradely labeled BF neurons	61
3.3 Distribution and proportion of retrogradely labeled neurons in the observed basal forebrain nuclei	62
3.4 Synaptic connectivity of the network, single unit activity of model cells, and VP/SI inputs	64
3.5 Single cell firing properties in experimental cases	66
3.6A Power spectrum of the amygdala neuronal population	67
3.6B Theta phase-couplings of different principal neuron and interneuron groups.	69
3.7 Coherence of different amygdala neuronal units	70
3.8 Ablation experiments	71
4.1 Cartoon illustrating segregation of currents	120
4.2 Schematic of the two ACT prediction pipelines.	121
4.3 Comparisons between predicted models from the two pipelines for example case 1 (Burster-1)	122
4.4 Comparisons between predicted models from the two pipelines for example case 2 (Buster-2)	122
4.5 Comparisons between predicted models from the two pipelines for example case 3 (tonic spiker with oscillatory potentials)	123
4.6 Comparisons between predicted models from the two pipelines for example case 4 (highly adaptive cell with oscillatory potentials)	124

NEURAL MODELING CASE STUDIES AT BIOPHYSICAL, MACHINE LEARNING, AND AUTOMATION LEVELS

Tyler J. Banks

Dr. Satish S. Nair, Dissertation Supervisor

ABSTRACT

This dissertation reports three case studies using machine learning, biophysical, and automation frameworks to study neural engineering challenges. The first study utilized machine learning with a clinical dataset to predict the risk of future opioid use disorder (OUD). The model achieved a high level of predictive accuracy and highlighted the most impactful variables that predicted the risk. The second study implemented recent tract-tracing data predicting the existence of a motif that generated the theta rhythm, similar to that in the hippocampus in the amygdala. This was done via the development of a biophysical model of the rodent amygdala that demonstrated how the theta rhythm could be engendered by an external theta-rhythmic inhibitory projection from the ventral pallidum and substantia innominata. The third study developed an automation pipeline using biophysical and machine learning schemes, to assist in the development of biophysical models of neurons. The approach implemented recent insights developed in our group related to currents being grouped into modules based on their neurocomputational signatures.

CHAPTER 1

INTRODUCTION AND OBJECTIVES

BACKGROUND AND MOTIVATION

This dissertation seeks to contribute to a deeper understanding of brain circuitry and its relation to behavior. A tight relationship exists between architectures in neuroscience and machine learning, which is not well understood presently. Since the studies use different types of software and platforms for modeling as well as analyses, software automation was found to be an important enabler for this research. It is only through such a combination that progress in neuroscience will be possible. These approaches provide varying levels of informed insight into fundamental principles of the brain.

Beyond the dissertation we expect that by having a generalized understanding of these model architectures, hybrid models will be feasible.

CHAPTER OVERVIEW

Chapter 2 – Existing predictive models of opioid use disorder (OUD) may change as the rate of opioid prescribing decreases. Using Veterans Administration’s EHR data, we developed machine-learning predictive models of new OUD diagnoses and ranked the importance of patient features based on their ability to predict a new OUD diagnosis in 2000–2012 and 2013–2021. Using patient characteristics, the three separate machine learning techniques were comparable in predicting OUD, achieving an accuracy of >80%. Using the random forest classifier, opioid prescription features such as early refills and

length of prescription consistently ranked among the top five factors that predict new OUD. Younger age was positively associated with new OUD, and older age inversely associated with new OUD. Age stratification revealed prior substance abuse and alcohol dependency as more impactful in predicting OUD for younger patients. There was no significant difference in the set of factors associated with new OUD in 2000–2012 compared to 2013–2021. Characteristics of opioid prescriptions are the most impactful variables that predict new OUD both before and after the peak in opioid prescribing rates. Predictive models should be tailored to age groups. Further research is warranted to determine if machine learning models perform better when tailored to other patient subgroups.

Chapter 3 – We develop a biologically realistic model of the Basolateral Amygdala (BLA) to show that by severing either the cholinergic or the GABAergic Basal Forebrain (BF) input to the BLA theta power decreases in the BLA, whereas removing the rhythmic GABAergic input together with either the non-rhythmic cholinergic or the thalamic/cortical input leads to complete cessation of theta rhythms in the BLA.

Chapter 4 – Automating the process of developing biophysical conductance-based neuronal models involves the selection of numerous interacting parameters, making the overall process computationally intensive, complex, and often intractable. A recently reported insight into the possible grouping of currents into distinct biophysical modules associated with specific neurocomputational properties also simplifies the process of automated selection of parameters. We show how our proposed grouping of currents into modules facilitates the development of a pipeline that automates the biophysical modeling of single neurons that exhibit multiple neurocomputational properties.

Chapter 2 - Predicting Opioid Use Disorder before and after the Opioid Prescribing Peak in the United States: A Machine Learning Tool using Electronic Healthcare Records

Tyler J. Banks¹, Tung D. Nguyen¹, Jeffrey K. Uhlmann¹, Satish S. Nair¹, Jeffrey F. Scherrer²

¹Electrical Engineering & Computer Science, University of Missouri, Columbia MO, USA

² Saint Louis University School of Medicine, Medicine, Saint Louis, MO, USA

Published in *Health Informatics Journal*. 2023;29(2). doi:[10.1177/14604582231168826](https://doi.org/10.1177/14604582231168826)

ABSTRACT

Existing predictive models of opioid use disorder (OUD) may change as the rate of opioid prescribing decreases. Using Veterans Affair's EHR data, we developed machine-learning predictive models of new OUD diagnoses and ranked the importance of patient features based on their ability to predict a new OUD diagnosis in 2000-2012 and 2013-2021. Using patient characteristics, the three separate machine learning techniques were comparable in predicting OUD, achieving an accuracy of >80%. Using the random forest classifier, opioid prescription features such as early refills and length of prescription consistently ranked among the top five factors that predict new OUD. Younger age was positively associated with new OUD, and older age inversely associated with new OUD. Age stratification revealed prior substance abuse and alcohol dependency as more impactful in predicting OUD for younger patients. There was no significant difference in the set of factors associated with new OUD in 2000-2012 compared to 2013-2021. Characteristics of opioid prescriptions are the most impactful variables that predict new OUD both before and after the peak in opioid prescribing rates. Predictive models should

be tailored to age groups. Further research is warranted to determine if machine learning models perform better when tailored to other patient subgroups.

INTRODUCTION

Opioid prescription rates and doses have declined since 2012 [1; 2]. However, a large number of patients remain on long-term opioid therapy, which increases the risk for opioid use/dependence (OUD). One out of four patients receiving long-term opioid therapy in primary care have OUD [3] and 4.7% of all pain patients prescribed an opioid will develop prescription OUD [4]. About 6 to 7 million persons in the United States suffer from OUD, not limited to prescription opioids [5] Among the commercially insured, the annual rate of OUD is approximately 0.4% [6].

Screening tools and urine drug screens (UDS) can be used to identify patients with OUD. [7; 8]. However, these tools are not perfect and patients who are seeking opioids can provide inaccurate reports of their opioid use and UDS screens miss many positive cases when obtained without a visual witness [9]. Thus, the likelihood of a significant number of patients with undetected OUD is high. Left undetected and untreated, patients have an increased risk for opioid overdose and other adverse outcomes.

Machine learning using electronic health record (EHR) data has the potential to predict OUD and accurate models can be incorporated into the EHRs to aid OUD detection in the clinical setting. The models that have used machine learning have typically used either EHR data or data related to medical claims. A study by Che et al. [10] used a large

sample of medical records and generated an AUC=0.80 in a model predicting OUD. Medical claims data have a comparatively lesser level of individual patient detail but have been successfully used to develop machine learning models to predict opioid use disorder. Commercial medical claims data have been utilized to develop a machine learning algorithm to predict opioid use disorder, with a c-statistic of 0.96 [11] and major contributing factors included duration of opioid use, overlapping opioid prescriptions, benzodiazepine prescriptions, and specific pain conditions. A recent study utilized the Canadian administrative health records billing data to achieve a balanced accuracy score of 86%, and found opioid-related poisoning, sedative hypnotic-related disorders, and polysubstance-related disorders to be predictive of OUD [12]. Their billing data did not include prescription/refill variables. EHR data contains more patient level variables (e.g., pain scores, laboratory results), and may out-perform models developed using medical claims data.

We are aware of two existing studies using EHR data in a machine learning model of new OUD. The first used Veterans Health Affairs (VHA) data from 829,827 patients with encounters from 2006 to 2016 [13]. Using 10,292 inpatient and 13,512 outpatient diagnoses as independent variables, this study developed a model that predicted cross-validated opioid use well for both inpatient (AUC = 0.822), and outpatient (AUC = 0.817) cases [13]. Similarly, EHR measures of laboratory values, pharmacy data and clinical characteristics from 716,533 patients were used to develop a machine learning classifier which produced an excellent predictive value for substance use disorder, not specific to OUD, with an AUC of 0.92 [13]. Dong and colleagues [14] used Cerner inpatient and

outpatient EHR records between 2008 to 2017 in a deep-learning model that had excellent precision in predicting OUD (AUC=0.937).

Because the literature is sparse and opioid prescribing has declined over the past decade, further research is needed to determine if the same set of factors predict OUD in the time period when opioid prescribing was increasing (2000-2012) compared to when it was decreasing (2013-2021). Because greater exposure to opioids should result in a higher rate of OUD, we expect a stronger association between prescription opioid characteristics and OUD from 2000-2012. In contrast, as access to opioids became more restricted, factors such as depression and past substance use disorder diagnosis which are associated with drug seeking and more severe and chronic pain, may be stronger predictors of OUD between 2013 and 2021. In addition, studies are needed that report on the predictive importance of individual variables. We used VHA EHR data to develop a predictive machine learning model of diagnosed OUD and determined if the set of important predictors of OUD differed between patients receiving opioids from 2000-2012 compared to those treated from 2013-2021. We used a pre-processing algorithm to re-structure the large datasets prior to developing the machine learning models. Second, we stratified analyses by three age groups. Third, we determined the relative importance of each predictor variable in predicting OUD.

METHODS

Variables were created from VHA administrative EHR data. Because data was de-identified, this work was reviewed and approved by the VA and academic affiliates IRBs as expedited. This data includes *International Classification of Disease, 9th and 10th Revisions, Clinical Modification* (ICD-9-CM and ICD-10-CM) diagnostic codes, laboratory results, prescription records, vital signs, and demographic information (Table 1). Detailed variable definitions are shown in the appendix, e-table 1.

Eligible patients had to be free of HIV and cancer pain, be regular VHA users (defined as having at least two annual visits) and starting a new period of prescription opioid use. New opioid use was defined by excluding patients with opioid fills for two years prior to 1/1/2002. Patients must have been without diagnosed OUD prior to 1/1/2002 for the pre-2012 cohort and for two years prior to 1/1/2015 for the post-2012 cohort. This allowed us to model risk factors for new onset OUD following the start of a new period of prescription opioid use. The 2-year look-back period has been shown to improve classification of new medication users and reduce the number of ineligible subjects [15]. Patients with missing demographic data were excluded. In patients with OUD, an individual's conditions that occurred after OUD diagnosis were censored. Figure 1 illustrates the sampling approach for the two time periods.

Table 1: Variables used for the models, grouped into three clusters. Boxed variable is the predicted output.

VARIABLE	DESCRIPTION
<i>Demographics variables (5; scrssn only for index)</i>	
scrssn	Scrambled Social Security number for index
is_male	1=Male, 0=Female
age	Age of patient
is_white	Race, 1=Yes, 0=No
is_married	Currently married, 1=Yes, 0=No
va_ins	Has and uses VA insurance, 1=Yes, 0=No
<i>Patient-condition variables (24 + 1 output that is boxed below)</i>	
adhd4depend	Had ADHD before opioid dependence
adjustmentreactb4depend	Adjustment reaction before opioid dependence
alcoholb4depend	Alcohol use before opioid dependence
amphetamineb4depend	Amphetamine use/dependence before opioid dependence
anxietyb4depend	Anxiety before opioid dependence
arthritisb4depend	Arthropathies before opioid dependence
backpainb4depend	Had back pain before opioid dependence
bipolarb4depend	Had bipolar disorder before opioid dependence
cannabisb4depend	Used cannabis before opioid dependence
cerebrovascularb4depend	Cerebrovascular disease before opioid dependence
cocaineb4depend	Cocaine use/dependence before opioid dependence
depressionb4depend	Depression before opioid dependence
hallucinogenb4depend	Hallucinogen use/dependence before opioid dependence
musculoskelpainb4depend	Musculoskeletal pain before opioid dependence
neuropathyb4depend	Neuropathy before opioid dependence
obesityb4depend	Obese before opioid dependence
othersubstb4depend	Other substance use/dependence before opioid dependence
overweightb4depend	Overweight before opioid dependence
schizophreniab4depend	Schizophrenia before opioid dependence
smokingb4depend	Smoker before opioid dependence
ptsdb4depend	PTSD before opioid dependence
personalitydisb4depend	Personality disorder before opioid dependence
tbib4depend	Traumatic Brain Injury before opioid dependence
unspecifieddrugb4depend	Unspecified drug use/dependence before opioid dependence
opioid_dep	Target indicator, OUD, op_dep and/or op_use; MODEL OUTPUT
<i>Prescription-fill variables (6)</i>	
total_op_days_early	Total number of days patient was early in picking up prescriptions before last rx end date
total_op_days_late	Total number of days patient was late in picking up prescription after last rx end date
max_op_days_early	Maximum days early for prescription refill
max_morph_dose	Maximum morphine equivalent dosage use
op_use_length	Opioid use length in days
op_dose_x_change	Change multiplier from beginning of opioid use to end (before possible dependence)

Cohort Eligibility

Dataset-1 comprised of 602,394 patients from 2000-2012, with 24,117 patients diagnosed with OUD. Age groups in this cohort were 18-34 years (n=40,480), 35-64 years (n=408,871), and >64 years (n=153,043).

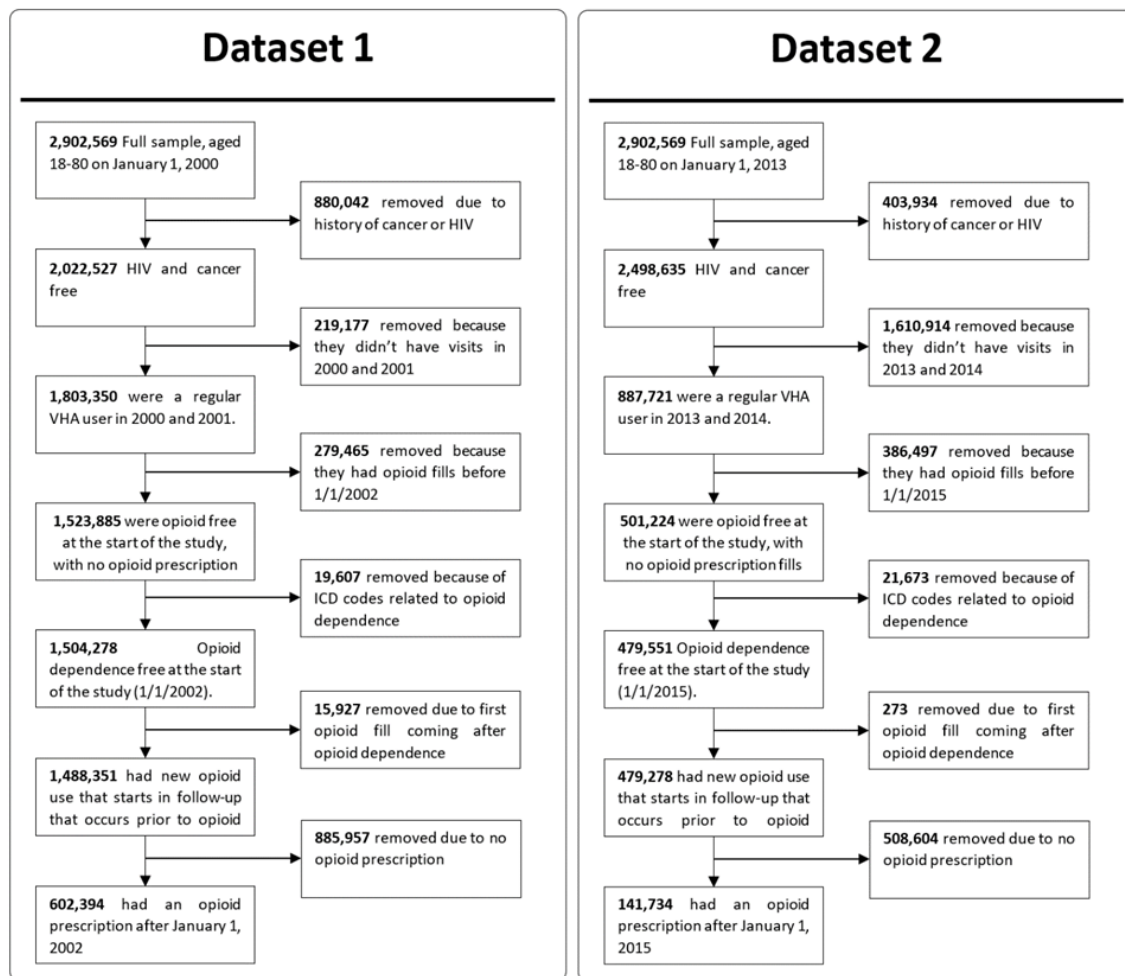


Figure 1: Eligibility criteria for Veterans Health Administration patient population. Each dataset was subject to the selection criteria outlined. For each dataset and at each stage, patients were removed, and the counts were noted.

Dataset-2 had 141,734 patients from 2013-2021, with 4,221 patients diagnosed with OUD. Also, the 2013-2021 dataset did not include new patients enrolled during 2013-

2021. Based on the selection criteria (figure 1), this dataset shared 84,603 patients from *dataset-1* and 57,131 new patients from the entire dataset. For dataset 2, the sample size by age group was 18-34 years (n=387), 35-64 years (n= 93,515), and >64 years (n=47,835). These age groups were selected because risk for opioid use disorder decreases with age across similar age groups [16].

Variable definitions

Opioid use, dose, and dose change

New opioid prescriptions included the following opioids, in immediate and long-term release formulations at any dose and duration: codeine, fentanyl, hydrocodone, hydromorphone, levorphanol, meperidine, morphine, oxycodone, oxymorphone, and pentazocine. Morphine milligram equivalent (MME) dose was computed with State of Washington Agency Medical Directors Group website opioid calculator (<http://agencymeddirectors.wa.gov/mobile.html>). We used the maximum MME received as a predictor variable. Continuous usage in days was defined as the use from the original opioid fill to the first occurrence of a gap in fills greater than 30 days or study end date. Dosage change is defined as the final opioid dosage divided by first opioid dosage. Methods to define dose and duration of prescription opioid use in this cohort have been reported previously [17].

Predictor variables

Predictor variable domains were selected because they have been associated with OUD [18; 19] Demographics included sex, age (at the beginning of the study Jan 1, 2000, and

Jan 1, 2013, respectively, for dataset-1 and dataset-2), race, marital status, and insurance. Insurance was defined as a binary variable (VHA vs. other types of health insurance). We used ICD-9-CM and ICD-10-CM codes to define psychiatric conditions which included: depression, attention deficit hyperactivity disorder (ADHD), posttraumatic stress disorder (PTSD), bipolar disorder, schizophrenia, personality disorder, adjustment reaction, and any anxiety disorder which was the presence of any of the following conditions: panic disorder, generalized anxiety disorder, social phobia, obsessive compulsive disorder or any other anxiety disorder not specified. We modeled alcohol use disorder, any non-opioid drug use disorder (including amphetamines, cannabis, hallucinogens, or unspecified), and nicotine dependence or a history of smoking. Physical comorbidities included overweight, and obesity defined by ICD-9-CM or ICD-10-CM code or body mass index. Painful conditions included arthritis, traumatic brain injury, neuropathy, musculoskeletal pain, and back pain. These conditions were created by combining groups of ICD-9-CM or ICD-10-CM codes from over 900 conditions for which an opioid may be prescribed [20; 21].

Prescription characteristics included the total number of days early a patient refilled their prescription, duration of opioid use in days, the maximum number of days a patient refilled early considering all refills, and the total number of days a prescription was refilled late. For a more consistent comparison of variables between decades, we scaled summed variables (such as the total number of days early an individual was to refill their opioid prescription) by the individual's overall duration of opioid use.

All covariates had to occur prior to new OUD. In total, thirty-five possible predictor variables were selected. Table 1 lists the variables and their definitions.

Outcome variable

OUD diagnosis (defined by ICD-9 and ICD-10 codes) was defined by diagnoses for opioid abuse only (ICD-9 305.5 and ICD-10 F11.10), or opioid dependence only (ICD-9 304.0 or 304.7 and ICD-10 F11.20 or F19.20) or both.

Improved data pre-processing.

In machine learning techniques that use large datasets, the issue of pre-processing data becomes significant. This is because databases typically have a very large number of dissimilar variables, including of multi-modal types as in patient health data. To address this pre-processing challenge, an algorithm was recently proposed to normalize the variables and was found to enhance performance compared to existing techniques such as Principal Components Analysis (PCA) and MinMax [22-24]. This algorithm was used to normalize the variables for the datasets in this study prior to the development of the different machine learning models. Specifically, the algorithm uses a unit-consistent (UC) matrix completion (MC) approach to rigorously estimate unknown quantities based on the information available. The UC matrix completion approach presumes the existence of unknown units on relevant state variables and then estimates unknown values in a manner that preserves those units, i.e., changing of units will produce the same UC completion but in the new units [22-24]. Briefly, from an original matrix A of patient data, the UC-transformed matrix $TA=DAE$, for positive diagonal matrices D and E, is uniquely

determined with the product of known elements in each row or column equal to 1. The completed matrix, A' , is then obtained by filling the unknown entries of TA with 1, i.e., preserving the product of elements in each row and column, and transforming back by pre-multiplying by inverse (D) and post-multiplying by inverse (E). This is the matrix completion (MC) process.

For our application, UC presumes that information contained in patient evaluations is implicitly derived from a set of incommensurate variables defining the state of a system, i.e., the health state of each patient. The UC algorithm determines imputed values in a way that provably ensures that the new values are consistent with the unknown units. For example, if the measurement process were to scale some subset of the units by arbitrary values, the imputed values from the UC algorithm will be the same up to the scaled values. This natural constraint is not preserved by other methods, e.g., that minimize an arbitrary norm such as squared error. This UC guarantee ensures that prediction results are consistent and robust in the sense that they are not sensitive to arbitrary choices of units applied during acquisition of patient data.

Experiments were carried out to test the robustness of this approach by removing a random set of variables for each training run, and comparing results with those from MinMax, PCA and UC-MC techniques. Figure 2 shows how the method exhibits smoother results, which shows robust exploitation of information as it becomes available. More importantly, it plateaus at a level above that of PCA, which indicates that UC-MC can extract more of the available information. Furthermore, the relative score of UC-MC after removing one variable was consistently higher and displays how it maintains robust prediction compared to the other two methods. Testing for the significance of results

given differing pre-processing methods, we found that the results with UC-MC were significantly better than those with PCA ($p<0.001$). However, no significance was found for the UC-MC vs MinMax case ($p\sim 0.25$) although the results remained consistently better (Figure 2). In summary, the UC-MC method was used consistently to pre-process the datasets including imputing values for three variables.

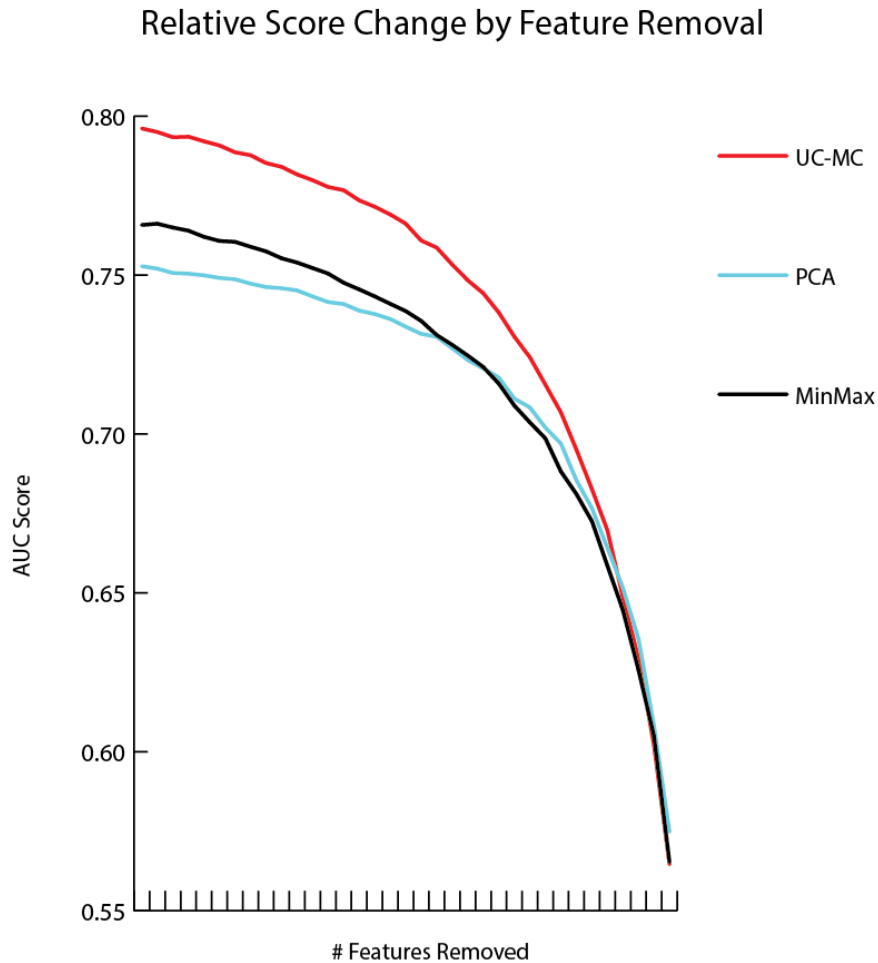


Figure 2: Relative AUC score using a subset of *dataset-1* on the deep neural network classifier. Features were randomly removed sequentially from a subset of *dataset-1* that consisted of 100,000 patients (remove 1 feature, remove 2 features, etc. – x-axis) and performance of three preprocessing methods were compared. The UC-MC approach showed consistently better performance compared to PCA and MinMax schemes ($p<0.001$ and $p\sim 0.25$ respectively).

Machine Learning Techniques

Before training each model, variables were scaled between 0 and 1 using the UC-MC scaler. Datasets were first split (80:20; by patient) for training/validation and holdout. Of the training/validation data, K-fold cross validation of models (K=5) was used to systematically repeat the train and validation split procedure (70:30; by patient) five times to obtain a more accurate representation of the model's ability to learn the dataset. The holdout dataset, that the model had not seen, was then used to judge the performance of the trained network. Area Under the Curve (AUC) was the primary metric chosen for quantifying the accuracy of the models. Logistic regression provided a baseline score for comparison with the deep neural network and random forest classifiers which are popular models with deep neural networks typically providing higher accuracy. Of these, the random forest classifier has an inbuilt feature to perform sensitivity analysis while the others require user-developed code for sensitivity analyses. All OUD cases were used during this process and a randomly selected subset of non-OUD were used to keep classification classes balanced such that the number of dependent patients matched the number of non-dependent patients to not bias the algorithm in any direction. Similarly, classification weighting is a viable and available alternative to achieve similar results.

Cross-tabulation tables, mean and standard deviation for all covariates were calculated for correctly classified, false positive and false negative entries in the datasets. To improve model results, principal component analysis (PCA) was computed which revealed 31 out of 35 variables were necessary to explain 95% of the data. The use of PCA improved the deep neural network results above the MinMax scaler but UC-MC

outperformed PCA, by an average of 0.025 AUC. We also explored the use of a convolutional input layer in the deep neural network model but found no difference.

Statistical Tools. Statistical significance of variables across subgroups were determined using the StatsModels python package. Significance (p-value) was computed using a generalized linear model with a binomial distribution [25] or t-test as appropriate (e.g., for the same patient in some tables) and is indicated with the specific test. The logistic regression model was implemented using ScikitLearn. The solver was lbfgs with a max iteration of 200 and a square error loss function. For our deep neural network model, a four-layer network (input, dense relu, dense relu, sigmoid output) was chosen. Optimal hyperparameter tuning was provided by ScikitLearn’s GridSearchCV. The random forest model utilized ScikitLearn and consisted of 100 estimators with a max depth of 40.

Software tools developed for data retrieval, processing, and analyses, are available upon request.

RESULTS

The overall characteristics of datasets 1 and 2, including the patient variables were determined and are listed first, followed by results from the machine learning models.

Characteristics of patient data across two time periods 2002-2012 and 2013-2021

Among the 602,394 patients with clinic encounters between 2000 and 2012, 24,117 had OUD and 578,277 were non-OUD. Of the patients with OUD, the mean age was 45.30 years (range 18 to 80), with 91.93% (22,127) being male and 8.1% (1945) female. Of these, 40.01% (9,675) had prior non-opioid substance use disorder recorded (compared to 7.79% in non-opioid dependent patients), and 75.26% (18,150) had reported depression before OUD (compared to 47.22% in non-OUD patients). Among the 141,734 patients with clinic encounters between 2013 and 2021, 4,221 had OUD and 137,513 were non-OUD. Of the OUD patients, the mean age was 57.25 years (range 31 to 80), with 89.5% (3,776) male and 10.5% (445) female. Of these 40.42% (1,706) had prior drug use recorded (compared to 12.2% in non-OUD patients), and 84.32% (3,559) had reported depression before OUD (compared to 65.42% in non-opioid dependent patients). A full report of overall patient characteristics can be found in Table 2.

Table 2. Patient characteristics, overall and by time period.

	Overall/total sample (n=659,525)	Time period 1 2000—2012 (n=602,394)	Time period 2 2013-2021 (n=141,734)
Age			
18-34 years	4.78% (n=31,551)	6.72% (n=40,480)	0.27% n=387
35-64 years	65.13% (n=429,576)	67.87% (n=408,871)	65.98% n=93,513
65+ years	30.08% (n=198,398)	25.41% (n=153,043)	33.75% n=47,834

Male gender	91.68% (n=604,660)	91.9% (n=553,610)	88.41% (n=125,313)
Race			
White	58.23% (n=384,023)	58.82% (n=354,312)	55.22% (n=78,260)
Other	17.26% (n=113,832)	17.28% (n=104,081)	19.9% (n=28,199)
Not reported	24.51% (n=161,670)	23.9% (n=144,001)	24.89% (n=35,275)
Currently married	47.89% (n=315,829)	48.2% (n=290,332)	42.09% (n=59,652)
Not reported	3.56% (n=23,462)	3.41% (n=20,553)	5.39% (n=7,640)
Only VA insurance	86.88% (n=572,965)	86.17% (n=519,091)	95.44% (n=135,273)
Comorbidities prior to opioid use/dependence			
Pain diagnoses			
Arthropathies	85.00% (n=560,571)	84.13% (n=506,824)	92.96% (n=131,759)
Back pain	71.64% (n=472,482)	69.65% (n=419,547)	87.21% (n=123,605)
Musculoskeletal	69.04% (n=455,354)	66.73% (n=401,978)	85.57% (n=121,278)
Neuropathic	38.36% (n=252,970)	36.04% (n=217,101)	51.85% (n=73,492)
Psychiatric disorders			
ADHD	0.99% (n=6,552)	0.8% (n=4,819)	2.05% (n=2,907)
Anxiety disorder	39.68% (n=261,709)	37.18% (n=223,960)	56.42% (n=79,964)
Adjustment disorder	19.85% (n=130,895)	17.71% (n=106,703)	32.44% (n=45,978)
PTSD	25.88% (n=170,678)	24.06% (n=144,928)	40.32% (n=57,149)
Bipolar disorder	14.96% (n=98,650)	13.22% (n=79,616)	25.55% (n=36,208)
Schizophrenia	8.13% (n=53,608)	7.92% (n=47,683)	10.44% (n=14,798)
Personality disorder	9.07% (n=59,809)	8.05% (n=48,511)	15.74% (n=22,314)
Depression	50.25% (n=331,385)	48.34% (n=291,194)	65.98% (n=93,523)
Alcohol use disorder	24.34% (n=160,529)	23.3% (n=140,341)	31.37% (n=44,467)
Amphetamine use disorder	1.45% (n=9,571)	1.25% (n=7,507)	2.54% (n=3,598)
Cannabis use disorder	7.3% (n=48,152)	6.53% (n=39,366)	12.25% (n=17,358)
Cocaine use disorder	6.77% (n=44,644)	6.54% (n=39,403)	9.5% (n=13,459)

Hallucinogen use disorder	0.16% (n=1,076)	0.15% (n=908)	0.25% (n=353)
Unspecified drug use disorder	3.79% (n=25,013)	3.7% (n=22,287)	5.03% (n=7,130)
Other drug use disorder	9.43% (n=62,179)	9.08% (n=54,723)	12.99% (n=18,413)
Nicotine dependence/smoking	46.12% (n=304,143)	44.74% (n=269,538)	55.59% (n=78,797)
Physical disorders			
Cerebrovascular disease	22.75% (n=150,010)	21.84% (n=131,545)	23.05% (n=32,675)
Overweight	7.29% (n=48,065)	5.3% (n=31,909)	16.26% (n=23,039)
Obesity	43.05% (n=283,954)	40.93% (n=246,571)	58.02% (n=82,239)
Traumatic brain injury	1.54% (n=10,138)	1.15% (n=6,956)	3.16% (n=4,483)
Prescription opioid characteristics [Mean (\pmSD)]			
Total days early fill	69.79 (\pm 295.51)	84.26 (\pm 342.16)	74.90 (\pm 317.65)
Maximum days early fill	7.87 (\pm 12.18)	8.76 (\pm 12.93)	7.33 (\pm 11.12)
Total days late fill	842.22 (\pm 1,064.89)	1,024.24 (\pm 1,190.59)	579.61 (\pm 771.27)
Maximum morphine equivalent dose	147.45 (\pm 222.63)	163.04 (\pm 232.22)	115.08 (\pm 197.98)
Duration in days - opioid use	1,181.65 (\pm 1,309.36)	1,407.37 (\pm 1,468.33)	974.96 (\pm 1,058.91)

Table 3 provides the sample sizes used for each model. Of the three modeling approaches, logistic regression, random forest, and deep neural network models, the random forest classifier was found to perform the best, with AUC measures in the range of 0.75-0.82 for all the cases. In general, the other classifiers also performed reasonably well, indicating that the dataset was self-consistent.

Table 3: AUC, precision (P), recall (R), and F1 performance scores of trained machine learning algorithms for the two datasets. Holdout scores presented.

CLASSIFIER	Dataset-1		Dataset-2	
Size OUD patients	602,394 (24,117)		141,734 (4,221)	
Logistic Regression	AUC: 0.7794 F1: 0.7740	P: 0.7692 R: 0.7789	AUC: 0.7612 F1: 0.7601	P: 0.7795 R: 0.7416
Random Forest	AUC: 0.7911 F1: 0.7985	P: 0.7862 R: 0.8112	AUC: 0.8118 F1: 0.8181	P: 0.7901 R: 0.8482
Deep Neural Network	AUC: 0.7723 F1: 0.7966	P: 0.7304 R: 0.8760	AUC: 0.758 F1: 0.7704	P: 0.7350 R: 0.8096

For each dataset the demographics and patient numbers with OUD diagnoses are listed.

For example, column 2 (dataset-1) in Table 3 lists the total number of patients and the subset with OUD diagnoses, 602,394 and 24,117 respectively. Precision (P) measured how accurate the positive predictions were, i.e., what percentage of positive predictions were correct, while recall (R) measured how well the classifier found the actual positives, i.e., which percentage of actual positive samples were correctly classified. For all of our models, we balanced the dataset (see Methods). In general, our models had a higher recall, compared to precision. We tried to minimize the risk of not warning a patient who may be at risk by minimizing the Miss Rate/False Negative Rate $FNR = FN / P = 1 - Recall$. F1 score is the harmonic mean of precision and recall, thus the F1 score shows the model's balanced ability to both capture positive cases (recall) and be accurate with the cases it does capture (precision). In our case it's just another validation, similar to AUC.

Stratification by age reveals differences in variable importance numbers

Because the random forest classifier provided the best performance, we used this scheme to develop individual models for each of the age stratified subgroups of dataset-1 and dataset-2.

The random forest classifier provides a utility to calculate Gini feature importance for each of the inputs by ranking its importance in predicting the output [26; 27], similar to ranking schemes used previously [28-30]. The relative importance of each variable is provided by its ranking which sum to 100 for all the variables. That is, all the relative importance numbers in the figure for the 35 variables in each of the three age categories add up individually to 100. For this reason, the higher the importance number of a variable, the more its relative importance in predicting the output. This was performed for both datasets 1 and 2, with results shown in Figures 2 and 3, respectively. Such an analysis provides important insights for the user and adds the attribute of ‘explainability’ that is sought from machine learning models [31]. The relative importance of the various variables in predicting OUD was explored for each of the models developed when stratifying the datasets by age (figures 2 and 3).

The results of random forest modeling to rank the importance of the variables in predicting OUD in dataset-1 are shown in Figure 3, for the three age categories 18-34, 35-64, and >64 yrs. Interestingly, four out of the top five features as far as importance were related to prescriptions, with the feature of age in the fifth place. The prescription features included the total number of days of early refills, duration of opioid use, the maximum duration of early refills, and the total duration of late refills. The order was largely the same in all three age groups. The predictive importance for these five variables were significantly higher compared to those of the next five in the group listed in figure 3 ($p<0.001$). Age within each stratified group, which was fifth in rankings, was

itself an important predictor of OUD. This prediction with age had a positive correlation for patients 18-34 years and a positive correlation for those >64 years. Furthermore, we found that the prescription-fill features of opioid use length, total opioid days late, and maximum opioid days early were significantly more important for the >64 age group compared to younger groups ($p<0.001$ and $p<0.001$ respectively). While maximum morphine dose was not a top 5 predictor, it was significantly more important for patients >64 years and had a 1.23 times higher importance number, compared to those younger ($p<0.001$). The model revealed that prior substance use disorder diagnoses (othersubstb4depend variable) was significantly more important in predicting opioid use disorder for younger (18-34) and mid-age (35-64) groups, compared to the older >64 years patient group (5.91x; $p<0.001$ and 8.04x; $p<0.001$, respectively). The same was true for cocaine use disorder as it was significantly more important in predicting OUD for younger (18-34) and mid-age (35-64) groups, compared to the older >64 years patient group (8.24x; $p<0.001$ and 8.84x; $p<0.001$, respectively). Another insight from the model was that alcohol use disorder was significantly more important for the younger age group compared to the older groups (18-34 vs 35-64: 2.59x, and 35-64 vs >64: 2.01x; p-values of 0.001 and 0.001, respectively).

Feature Importance Stratified by Age (Dataset 1)

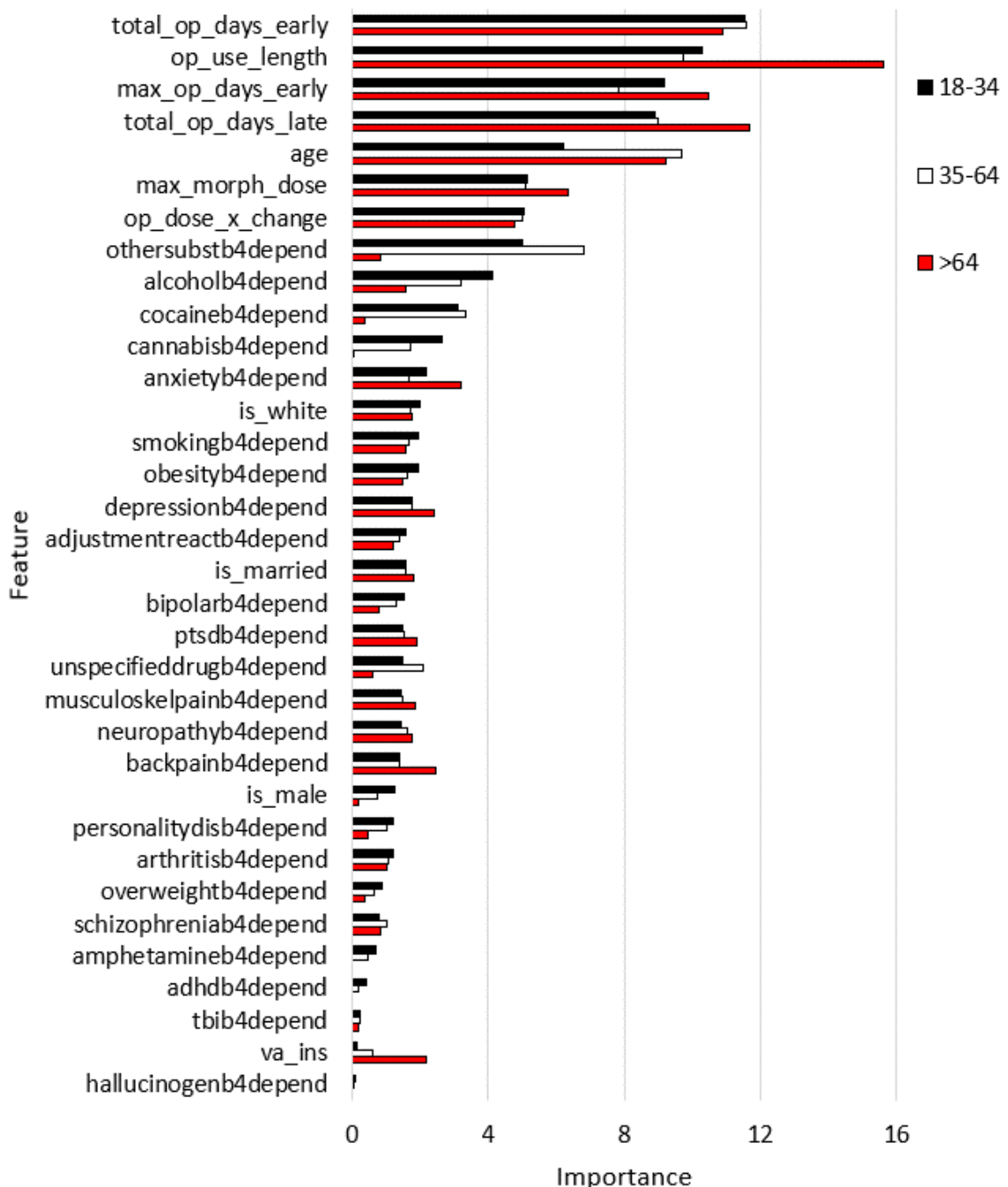


Figure 3 Variable importance stratified by age, using random forest classifier. For dataset-1, we determined the feature importance for three distinct age groups: 18-34, 35-64, and >64 yrs. (ordered by importance number for the 18-34 age group). The X axis is the relative feature importance determined by random forest while the Y axis denotes each feature.

Feature Importance Stratified by Age (Dataset 2)

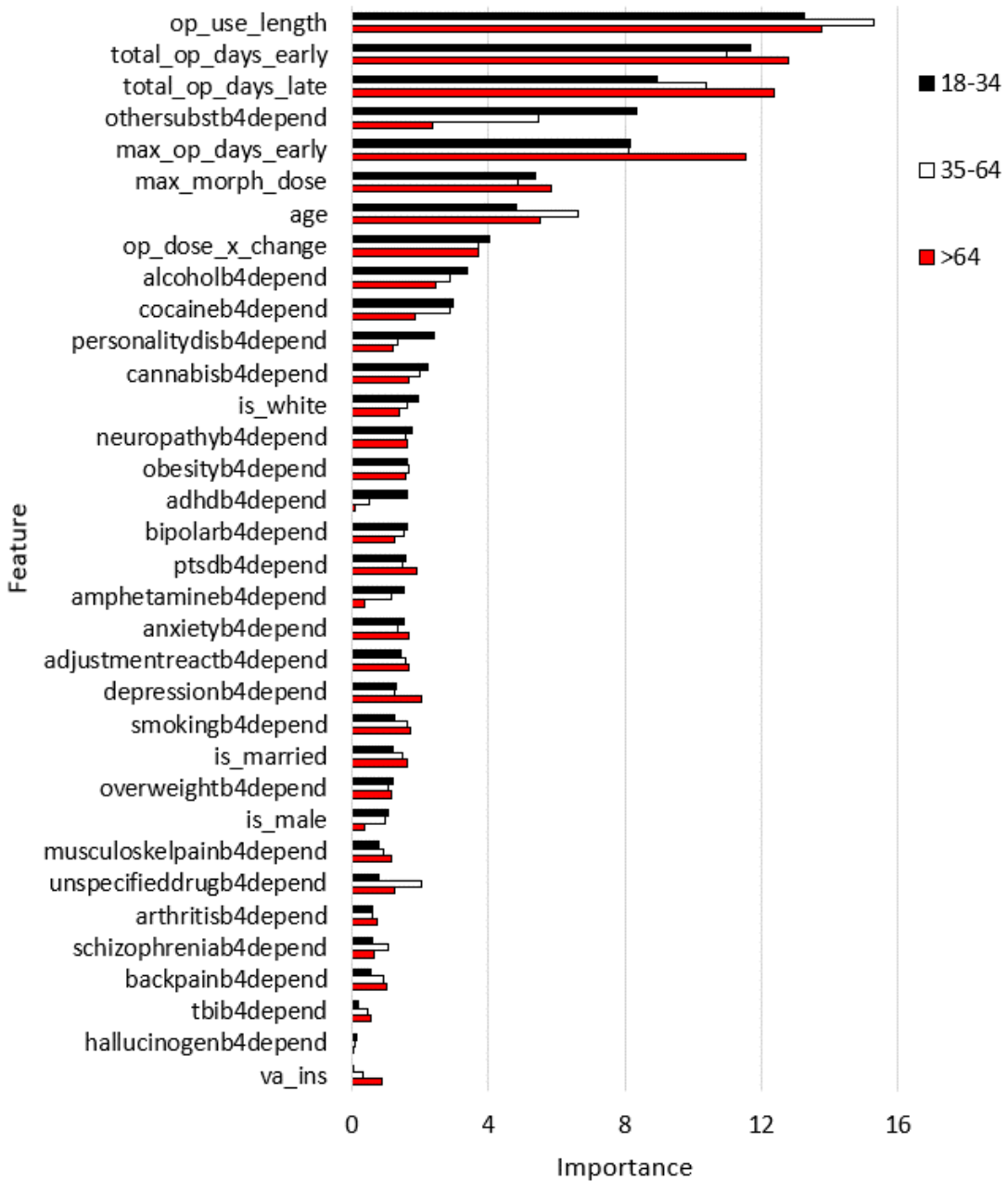


Figure 4: Feature importance stratified by age, using random forest classifier for dataset 2.

For dataset-2, we determined the feature importance for three distinct age groups: 18-34, 35-64, and >64 yrs. (ordered by importance number for the 18-34 age group) in Figure 4. The X axis is the relative feature importance determined by random forest while the y axis denotes each feature.

Predictor variable importance numbers were largely consistent across decades

Datasets-1 and *2* enabled comparisons of variables as they relate to OUD prediction performance to determine if indicators may have changed between 2001-2012 and 2013-2021. *Dataset-2* had 84,603 patients that were shared with *dataset-1*, with 3,120 OUD cases. Note that OUD cases from 2000-2012 were excluded from *dataset-2* (see Fig. 1 and methods). Similar to the analysis in the previous dataset, we stratified *dataset-2* by age, and trained the random forest classifier for each of the stratified datasets separately, and then generated variable importance numbers for the age stratified categories as shown in figure 4. Prescription-fill variables were again the top variables in all stratified subsets of *dataset-2*. As noted earlier, *dataset-2* shared 59% of the patients with *dataset-1* which accounts for lower numbers of patients in the 18-34 category and the >64 category. Nevertheless, prescription-fill variables clearly dominated the importance number rankings in *datasets 1* and *2*, confirming their overall importance in predicting future OUD.

Table 4 Change in prescription variables across decades.

Percent change in mean values from Decade 1 to Decade 2	OUD Diagnosed Patients*	Non-OUD Patients*
Total opioid pickup days early	37.19%	13.09%
Total opioid pickup days late	-38.16%	-15.86%
Maximum opioid pickup days early	-13.78%	-15.54%
Maximum morphine dose	-40.62%	-28.53%
Opioid use length	-48.80%	-29.55%
Opioid dose change	-53.05%	-28.78%

* the differences were significant ($p<0.001$) for all variables listed

Raw prescription-related variables for each decade were extracted for OUD diagnosed patients, and non-OUD diagnosed patients. The values shown are changes in prescription variables across decades (datasets 1 and 2 for decades 1 and 2, respectively). Percent change was calculated for each group OUD and non-OUD for each case [(mean value in dataset 1 – mean value in dataset 2)/(mean value in dataset 1)]. Paired sample t-test was used to assess changes in the same patient.

Given the importance of prescription-fill variables in predicting OUD, we explored how the raw measures of these variables compared across decades 2000-2012 (dataset 1; decade-1) vs 2013-2021 (dataset 2; decade-2). Table 4 lists the results of this analysis. Changes in the raw measures of the prescription-fill variables indicated an increased urgency in obtaining prescriptions in 2013-2021 compared to 2000-2012, i.e., patients came earlier or delayed less.

An investigation of the changes in characteristics for the *same patient* between time periods when they did not have OUD (2000-2012; decade-1) vs when they did (2013-2021; decade-2) revealed that for the same patient, the means of the raw prescription-fill variable related to total opioid days late was significantly lower in decade-2 compared to decade-1 (0.3098 vs 0.5275, -41.3%, p<0.0001; t-test). Similarly, the total number of early refills days was significantly higher in decade-2 compared to decade-1 (0.1982 vs 0.1472; +34%, p<0.0001; t-test); (ii) the difference in means for depression was significantly higher in decade-2 compared to decade-1 (normalized means – 1=observed, 0=not observed; 0.8455 vs 0.7862, +7.5%, p<0.0001); (iii) Other substance use disorder was also higher in decade-2 compared to decade-1 (0.3897 vs 0.3356; +16.1%, p=0.0001;

t-test). In addition to yielding further insights, these longitudinal changes in the raw measures for four of the variables deemed important in predicting OUD (Figure 3), and similar findings in Table 4, provide validation for the ranking of predictor variables in their ability to forecast OUD (Figures 3 and 4).

DISCUSSION

Machine learning models using EHR data were found to be viable in predicting OUD. Duration of opioid use, total days from early opioid fills, and total number of late opioid fill days were the most important predictors of OUD. These findings were consistent for both the period when the opioid epidemic was worsening (2000-2012) and during the period of declining opioid prescription rates and doses (2013-2021).

Unexpectedly, other forms of substance use disorders and common psychiatric disorders, e.g., depression, did not have the same magnitude of contribution to OUD as the prescription characteristics. However, the present findings are consistent with prior studies demonstrating that after the publication of the CDC guideline, more potent and high dose opioids continue to be prescribed to patients at greatest risk for OUD [17]. This indicates that modifiable factors, (e.g., duration of opioid prescriptions) are key contributors to OUD. Because early fills and long duration prescriptions continue to predict OUD following decreases in opioid prescribing [1; 2] and the release of the 2016 CDC's opioid prescribing guideline [32] further interventions designed to reduce long duration opioid prescribing and early refills to patients at risk for adverse opioid outcomes is warranted [33].

Our results are consistent with a machine learning algorithm which identified that opioid use duration and overlapping opioid prescriptions distinguished OUD in a large cohort of medical claims data from 2006 to 2018 [11]. Our findings are largely consistent with an analyses of private sector EHR data which observed opioid medications were the 4th most

important measurement predicting OUD(Dong et al). Direct comparisons between our findings and this prior study is limited because we modeled multiple opioid medication measures, including early refills while Dong and colleagues modeled any opioid prescription. In addition, VHA patients tend to stay within the VHA system as compared to private sector patients who are more likely to change providers as their source of health insurance varies over time. Using VHA data should reduce misclassification of outcome and predictor diagnoses relative to data from private sector health care systems where fragmented health care could generate more missed diagnoses when patients move from one healthcare system to another. Including the duration of an opioid prescription and early refills in our predictive model better captures risk factors for OUD, specifically long-term opioid use and using more than prescribed leading to early fills are indicators of the development of problem opioid use. These are stronger predictors of OUD as compared to exposure to any opioid medication.

Our findings differ from a predictive model using commercial EHR data, which observed mood disorder to be the most important predictor of diagnosed substance use disorder, not specific to OUD [13]. This suggests machine learning algorithms should be tailored to the type of substance use disorder (SUD), and factors contributing to OUD may not be the same as those which predict other types of substance use disorder.

Additional research is needed to establish the accuracy of predicting OUD in different patient populations. Predictive models should be validated by determining how well the model predicts undiagnosed OUD. By administering diagnostic interviews to patients

with and without a medical record diagnosis for OUD a true gold standard can be obtained. The model should be re-calibrated after predicting OUD cases confirmed by diagnostic interview.

Because the strongest predictors of OUD are characteristics of the opioid prescription, the clinical utility could be very high. EHR best practice alerts could caution prescribers when the combination of opioid dose, duration and other factors found to predict OUD indicate high risk

Limitations

It was not determined if the opioids were taken as prescribed, taken with other prescriptions obtained outside the VA or supplemented with illicit opioids. Retrospective medical record data is vulnerable to misclassification and the contribution of some diagnoses may be decreased to the degree that patients with a condition (e.g., depression) are misclassified as unaffected. The VHA patient population is predominately male and has a high rate of comorbidity, therefore results may not generalize to non-VHA patients. It is possible that the results from Veterans Health Administration data may not generalize to private sector health care systems. However, numerous studies using VHA data on topics ranging from the association between long-term opioid use and new onset depression [17] to the link between metformin and dementia [34] and vaccinations and dementia [35-37] have been replicated in private sector medical record and medical claims data.

Compared to manual chart abstraction, the validity of OUD diagnoses in the medical record ranges from fair to good [38-41] and depending on which elements of the medical chart are used to count toward an OUD diagnosis, the agreement between medical record and diagnoses is 80% or better. However, this does not distinguish between primary prescription OUD vs. other OUD types such as heroin use disorder.

Our study did not use a pure data mining approach. We selected potential predictors of OUD based on theory or previous literature. Further research is needed to compare the utility of predictive algorithms that are completely data driven and those that are developed with user input.

Conclusions. Our results point to modifiable prescribing behavior as the key contributor to OUD. Replication in other healthcare systems is needed and comparisons to data driven models warranted. Overall, results hold promise that machine learning models can reasonably predict OUD and could be incorporated in the electronic health record as a clinical decision aid.

REFERENCES

1. Bohnert ASB, Guy GP, Jr., Losby JL (2018) Opioid prescribing in the united states before and after the centers for disease control and prevention's 2016 opioid guideline, *Ann Intern Med* 169, 367-375. PMC6176709.
2. Guy GP, Jr, Zhang K, Schieber LZ, Young R, Dowell D (2019) County-level opioid prescribing in the united states, 2015 and 2017, *JAMA Internal Medicine* 179, 574-576.
3. Centers for disease control and prevention. Opioid basics.
<Https://www.Cdc.Gov/drugoverdose/opioids/prescribed.Html>. Accessed 9 august 2022.
4. Higgins C, Smith BH, Matthews K (2018) Incidence of iatrogenic opioid dependence or abuse in patients with pain who were exposed to opioid analgesic therapy: A systematic review and meta-analysis, *Br J Anaesth* 120, 1335-1344.
5. Keyes KM, Rutherford C, Hamilton A, Barocas JA, Gelberg KH, Mueller PP, Feaster DJ, El-Bassel N, Cerdá M (2022) What is the prevalence of and trend in opioid use disorder in the united states from 2010 to 2019? Using multiplier approaches to estimate prevalence for an unknown population size, *Drug Alcohol Depend Rep* 3. PMC9248998.
6. Kirson NY, Shei A, Rice JB, Enloe CJ, Bodnar K, Birnbaum HG, Holly P, Ben-Joseph R (2015) The burden of undiagnosed opioid abuse among commercially insured individuals, *Pain Med* 16, 1325-1332.
7. Katz NP, Sherburne S, Beach M, Rose RJ, Vielguth J, Bradley J, Fanciullo GJ (2003) Behavioral monitoring and urine toxicology testing in patients receiving long-term opioid therapy, *Anesth Analg* 97, 1097-1102.
8. Heit HA, Gourlay DL (2004) Urine drug testing in pain medicine, *J Pain Symptom Manage* 27, 260-267.
9. Mallya A, Purnell AL, Svrankic DM, Lovell AM, Freedland KE, Gott BM, Sayuk GS, Cicero TJ, Brawer PA, Trafton JA, Scherrer JF, Lustman PJ (2013) Witnessed versus unwitnessed random urine tests in the treatment of opioid dependence, *The American Journal on Addictions* 22, 175-177.
10. Che Z, St Sauver J, Liu H, Liu Y (2017) Deep learning solutions for classifying patients on opioid use, *AMIA Annu Symp Proc* 2017, 525-534. PMC5977635.
11. Segal Z, Radinsky K, Elad G, Marom G, Beladev M, Lewis M, Ehrenberg B, Gillis P, Korn L, Koren G (2020) Development of a machine learning algorithm for early detection of opioid use disorder, *Pharmacology Research & Perspectives* 8, e00669.
12. Liu YS, Kiyang L, Hayward J, Zhang Y, Metes D, Wang M, Svenson LW, Talarico F, Chue P, Li X-M, Greiner R, Greenshaw AJ, Cao B (2023) Individualized prospective prediction of opioid use disorder, *The Canadian Journal of Psychiatry* 68, 54-63.
13. Ellis RJ, Wang Z, Genes N, Ma'ayan A (2019) Predicting opioid dependence from electronic health records with machine learning, *BioData Min* 12, 3. PMC6352440.
14. Dong X, Deng J, Rashidian S, Abell-Hart K, Hou W, Rosenthal RN, Saltz M, Saltz JH, Wang F (2021) Identifying risk of opioid use disorder for patients taking opioid medications with deep learning, *J Am Med Inform Assoc* 28, 1683-1693. PMC8324214.
15. Roberts AW, Dusetzina SB, Farley JF (2015) Revisiting the washout period in the incident user study design: Why 6-12 months may not be sufficient, *J Comp Eff Res* 4, 27-35. PMC4410733.
16. Han B, Compton WM, Blanco C, Crane E, Lee J, Jones CM (2017) Prescription opioid use, misuse, and use disorders in u.S. Adults: 2015 national survey on drug use and health, *Ann Intern Med* 167, 293-301.
17. Scherrer JF, Salas J, Copeland LA, Stock EM, Ahmedani BK, Sullivan MD, Burroughs T, Schneider FD, Buchholz KK, Lustman PJ (2016) Prescription opioid duration, dose, and increased risk of depression in 3 large patient populations, *The Annals of Family Medicine* 14, 54-62.

18. Webster LR (2017) Risk factors for opioid-use disorder and overdose, *Anesth Analg* 125, 1741-1748.
19. Peltier MR, Sofuoglu M, Petrakis IL, Stefanovics E, Rosenheck RA (2021) Sex differences in opioid use disorder prevalence and multimorbidity nationally in the veterans health administration, *J Dual Diagn* 17, 124-134. PMC8887838.
20. Scherrer J.F., Svrakic D.M., Freedland K.E., Chrusciel T., Balasubramanian S., Bucholz K.K., Lawler E.V., P.J. L (2014) Prescription opioid analgesics increase the risk of depression, *J Gen Intern Med* 29, 491-499.
21. Seal KH, Shi Y, Cohen G, Cohen BE, Maguen S, Krebs EE, Neylan TC (2012) Association of mental health disorders with prescription opioids and high-risk opioid use in us veterans of iraq and afghanistan, *JAMA* 307, 940-947.
22. Nguyen T, Uhlmann J (2022) A unit-consistent tensor completion with applications in recommender systems. , CoRR abs/220401815.
23. Nguyen T, Uhlmann J (2021) Canonical tensor scaling, *Journal de Ciencia e Ingenieria* 13, 13-21.
24. Zhang B, Uhlmann J (2019) Applying a unit-consistent generalized matrix inverse for stable control of robotic systems, *Journal of Mechanisms and Robotics* 11.
25. Nelder JA, Wedderburn RWM (1972) Generalized linear models, *Journal of the Royal Statistical Society: Series A (General)* 135, 370-384.
26. Breiman L (2001) Random forests, *Machine Learning* 45, 5-32.
27. Hastie T, Tibshirani R, Friedman J (2001) *The elements of statistical learning* (New York, NY, USA: Springer New York Inc.).
28. Swamidass PM, Nair SS, Mistry SI (1999) The use of a neural factory to investigate the effect of product line width on manufacturing performance, *Management Science* 45, 1524-1538.
29. Reid JC, Nair SS, Mistry SI, Beitman BD (1996) Effectiveness of stages of change and adinazolam sr in panic disorder: A neural network analysis, *J Anxiety Disord* 10, 331-345.
30. Kashani JH, Nair SS, Rao VG, Nair J, Reid JC (1996) Relationship of personality, environmental, and dica variables to adolescent hopelessness: A neural network sensitivity approach, *J Am Acad Child Adolesc Psychiatry* 35, 640-645.
31. Burkart N, Huber M (2021) A survey of the explainability of supervised machine learning, *Journal of Artificial Intelligence Research* 70.
32. Dowell D, Haegerich TM, Chou R (2016) Cdc guideline for prescribing opioids for chronic pain--united states, 2016, *JAMA* 315, 1624-1645. PMC6390846.
33. Scherrer JF, Salas J, Schnurr PP (2020) Repeated assessment of posttraumatic stress disorder severity and the risk of mortality, *JAMA Netw Open* 3, e1920493.
34. Scherrer JF, Salas J, Floyd JS, Farr SA, Morley JE, Dublin S (2019) Metformin and sulfonylurea use and risk of incident dementia, *Mayo Clin Proc* 94, 1444-1456. PMC7029783.
35. Scherrer JF, Salas J, Wiemken TL, Jacobs C, Morley JE, Hoft DF (2021) Lower risk for dementia following adult tetanus, diphtheria, and pertussis (tdap) vaccination, *J Gerontol A Biol Sci Med Sci* 76, 1436-1443.
36. Scherrer JF, Salas J, Wiemken TL, Hoft DF, Jacobs C, Morley JE (2021) Impact of herpes zoster vaccination on incident dementia: A retrospective study in two patient cohorts, *PLoS One* 16, e0257405. PMC8597989.
37. Wiemken TL, Salas J, Morley JE, Hoft DF, Jacobs C, Scherrer JF (2022) Comparison of rates of dementia among older adult recipients of two, one, or no vaccinations, *J Am Geriatr Soc* 70, 1157-1168. PMC9300193.
38. Palumbo SA, Adamson KM, Krishnamurthy S, Manoharan S, Beiler D, Seiwel A, Young C, Metpally R, Crist RC, Doyle GA, Ferraro TN, Li M, Berrettini WH, Robishaw JD, Troiani V

- (2020) Assessment of probable opioid use disorder using electronic health record documentation, JAMA Network Open 3, e2015909-e2015909.
- 39. Howell BA, Abel EA, Park D, Edmond SN, Leisch LJ, Becker WC (2021) Validity of incident opioid use disorder (oud) diagnoses in administrative data: A chart verification study, J Gen Intern Med 36, 1264-1270. PMC8131432.
 - 40. Ranapurwala S, Alam I, Clark M, Carey T, Chelminski P, Pence B, Korte J, L-T W, Wolfson M, Christensen S, Capata M, Douglas H, Greenblatt L, Bowlby L, Spangler J, Marshall S (2021) 0108 limitations of opioid use disorder (oud) icd codes: Development and validation of a new oud identification algorithm in electronic medical records, Inj Prev 27, A31-A32.
 - 41. Lagisetty P, Garpestad C, Larkin A, Macleod C, Antoku D, Slat S, Thomas J, Powell V, Bohnert ASB, Lin LA (2021) Identifying individuals with opioid use disorder: Validity of international classification of diseases diagnostic codes for opioid use, dependence and abuse, Drug Alcohol Depend 221, 108583. PMC8409339.

Chapter 3 - Anatomical and Computational Investigation of Basal Forebrain Innervation of the Amygdala

Tugce Tuna^{1#}, Tyler J. Banks^{2#}, Greg Glickert², Cem Sevinc¹, Satish S. Nair^{2*}, Gunes Unal^{1*}

¹Behavioral Neuroscience Laboratory, Department of Psychology, Boğaziçi University, 34342 Istanbul, Turkey

²Neural Engineering Laboratory, Department of Electrical Engineering and Computer Science, University of Missouri, Columbia, MO 65211, USA

#Equal contribution

*Corresponding authors: SSN: nairs@missouri.edu; GU: gunes.unal@boun.edu.tr

Acknowledgements: This research was funded by an EMBO Installation Grant and Health Institutes of Türkiye (TUSEB) research grant (Project no: 24530) to GU, and NIH MH122023 and NSF OAC-1730655 to SSN. The authors thank Aybüke Akkaya for contributing to the surgical procedures.

In the final stages of preparation to be submitted to *Brain Structure and Function*.

Introduction

Cholinergic, GABAergic, glutamatergic and peptidergic neuronal groups in the basal forebrain (BF) innervate a wide array of cortical and subcortical limbic regions, including the hippocampal formation and the amygdaloid complex (Mesulam et al. 1983; Frotscher and Léránth 1985; Freund and Antal 1988; Zaborszky et al. 1999, 2015; Mascagni and McDonald 2009; Muller et al. 2011; McDonald et al. 2011; Agostinelli et al. 2019). Medial septal cholinergic and GABAergic innervation of the hippocampus are well-studied for their role in several *cognitive* functions and in hippocampal oscillatory rhythms (Frotscher and Léránth 1985; Freund and Antal 1988; Pang et al. 2001; Buzsáki 2002; Xu et al. 2004; Yoder and Pang 2005; McNaughton et al. 2006; Roland and Savage 2009; Hangya et al. 2009; Vega-Flores et al. 2014; Roland et al. 2014; Király et al. 2023). The BF gives rise to equally dense projections to the amygdaloid complex from the ventral pallidum (VP) and the substantia innominata (SI) (Carlsen et al. 1985; Mascagni and McDonald 2009; McDonald et al. 2011; Agostinelli et al. 2019; Fu et al. 2020). However, the mechanistic role of BF projections in amygdala oscillations and the *affective* processes orchestrated by the amygdaloid complex remains to be elucidated. Here, we utilized a two-fold approach to characterize the anatomical structure and functional role of the BF innervation of the amygdaloid complex. We first carried out retrograde labeling and immunohistochemical characterization of BF neurons that project to various nuclei of the amygdala and the bed nucleus of stria terminalis (BNST). Once we revealed the major source of cholinergic and non-cholinergic innervation of the amygdaloid complex, we developed a biophysically realistic amygdala network model, and tested the role of BF in the emergence of basolateral amygdala network activity and theta oscillations *in silico*.

A subpopulation of GABAergic neurons located in the VP and SI target the basal (BL); and to a lesser degree, the lateral (LA), basomedial (BM) and the central nuclei (CeA) of the amygdaloid complex, as well as the BNST (Carlsen et al. 1985; Mascagni and McDonald 2009; McDonald et al. 2011; Mongia et al. 2016; Agostinelli et al. 2019). The cholinergic to non-cholinergic ratio of the basolateral amygdala-projecting BF neurons is estimated to be approximately 3:1 (Carlsen et al. 1985), with GABAergic neurons making up at least 10% of the complete projections (Mascagni and McDonald 2009). Septo-hippocampal GABAergic projections are known to exclusively (Freund and Antal 1988b; Unal et al. 2015) target GABAergic interneurons in the hippocampus, contributing to and leading the theta activity by forming an interneuron-type and time (oscillatory phase)-specific, complex disinhibitory circuit with pyramidal neurons (Tóth et al. 1997; Yoder and Pang 2005; Hangya et al. 2009; Király et al. 2023). As with the GABAergic septo-hippocampal neurons, large majority of VP/SI GABAergic amygdalopetal projection neurons form synapses selectively with GABAergic interneurons in the amygdala (McDonald et al. 2011). This suggests that BF GABAergic projections that target different limbic structures may share common structural properties and circuit-level functions with the septo-hippocampal system (Tóth et al. 1997; Unal et al. 2018).

Based on the anatomical commonalities between the septo-hippocampal GABAergic pathway and the amygdaloid-complex-targeting VP/SI GABAergic projections, we theorize that BF GABAergic neurons carry out a uniform function in all downstream limbic structures via formation of similar interneuron-type and oscillatory phase-specific disinhibitory circuits (Tóth et al. 1997; Yoder and Pang 2005; Hangya et al. 2009). As septo-hippocampal GABAergic projections are required for several forms of

hippocampal functioning, we hypothesize that VP GABAergic innervation of the amygdala is required for regulating fear learning-related theta oscillations (Seidenbecher et al. 2003; Lesting et al. 2011; Stujenske et al. 2014; Davis et al. 2017) in the amygdala.

Here, we present an anatomical-computational investigation of this theory by utilizing retrograde tract-tracing coupled to fluorescent immunohistochemistry, and a biophysical network model of the BLA. In anatomical experiments, we identify and quantify parvalbumin (PV)- or calbindin (CB)-immunoreactive (+) putative GABAergic, and choline acetyltransferase (ChAT)-immunoreactive cholinergic BF neuronal subgroups that target the “input” (LA and BL) and “output” centers (CeA and BNST) of the amygdaloid complex. Based on our findings and previous anatomical data, we develop a 1000-cell computational BLA network model (Hummos and Nair 2017; Feng et al. 2019) that incorporates principal neurons and 3 different BLA interneuron types, rhythmic GABAergic and non-rhythmic cholinergic VPSI afferents, and constant excitatory thalamic/cortical inputs of the BLA. We utilize this model to investigate the involvement of these BF projections on the network oscillations of the BLA, which stands at the center of the so-called “fear circuit” (Sah and Westbrook 2008; Shin and Liberzon 2010). We show that BF projections play a key role in BLA theta genesis, and that cholinergic projections modulate theta’s power minimally.

Materials and Methods

Neuroanatomical Experiments

Animals

Adult male Wistar rats (280-380 g; n = 9) were housed in cages of four with *ad libitum* access to food and water under controlled laboratory conditions (21 ± 1 °C; 40 – 60% humidity; 12:12 day/night cycle, lights on at 8:00 AM). All experimental procedures were approved by the Boğaziçi University Institutional Ethics Committee for the Use of Animals in Experiments (BÜHADYEK) and carried out by licensed personnel.

Stereotaxic surgery and retrograde tract-tracing

Animals were deeply anesthetized with IP injections of a ketamine (80 mg/kg) - xylazine (13.3 mg/kg) mixture. Following induction of anaesthesia, a local anaesthetic (Vemcaine, 10%) and an povidone-iodine solution were applied to the shaved head before placing the animal to the stereotaxic frame (Kopf Instruments, USA). A homeothermic heating pad was used to monitor and maintain the body temperature at 36 °C. Two unilateral craniotomies were performed above the anterior-posterior (AP) and medial-lateral (ML) coordinates of the target nuclei. Red (diluted in saline by 1:2, volume = 200 nl) and green (undiluted, volume = 200 nl) fluorescent latex microspheres (Retrobeads, Lumafluor Inc., USA) were injected into the LA (AP = -2.80, ML = ±5.30, DV = -7.30), BL (AP = -2.80, ML = ±4.60, DV = -8.20), CeA (AP = -2.40, ML = ±4.20, DV = -8.00), and the central BNST (cBNST) (AP = -0.48, ML = ±1.40, DV = -6.00) (coordinates in mm are based on the rat brain atlas of (Paxinos and Watson, 2007); Fig. 1A-B).

In each animal, we injected one color of Retrobeads into one of the amygdaloid nuclei, (LA, BL or CeA) and the other into the cBNST (n = 3 animals for each pairing).

We counterbalanced the target hemispheres, ensuring that same number of animals received injections in the right and left hemisphere. The tracers (green or red Retrobeads) were counterbalanced for each target region (Fig. 1A-B). Injections were made with a microinjection syringe pump and a 1 μ L micro-injection syringe (Hamilton, NV, USA). Each tracer injection took 5 minutes (40 nl/s), after which the syringe was maintained at the target location for 10 minutes before retrieval to minimize dorsal diffusion. Once the incision was sutured, a local analgesic (Anestol pomade, 5% lidocaine and Jetokain, 5 mg/kg) was applied to the cranial surface before the animal was removed from the stereotaxic apparatus. The animals underwent a 5-day post-surgical recovery period in order to ensure maximal axonal transport of the Retrobeads.

Perfusion-fixation and tissue preparation

Following the recovery period, animals were deeply anesthetized by IP injections of the ketamine (80 mg/kg) - xylazine (13.3 mg/kg) mixture, and perfused transcardially with 0.9% saline and 4% depolymerized paraformaldehyde (PFA) in 0.1M PBS. Removed brains were post-fixed in the same fixative solution for 24-48 h at 4 °C. They were thoroughly rinsed following post-fixation and transferred to 0.1 M PB for slicing. Serial 60-80 μ m thick coronal sections were obtained using a Leica VT 1000S vibratome (Leica Microsystems, Germany).

Immunohistochemistry

We employed the immunofluorescence labelling protocol from Unal et al., 2015. PBS with 0.3% Triton X-100 (PBS-TX) was used in all solutions and rinsing procedures to achieve tissue penetration. Coronal sections were rinsed 3 times (10 min each) in PBS-TX, followed by 1 h blocking at RT in 20% Normal Horse Serum (NHS) or Normal Goat

Serum (NGS), depending on the secondary antibody. The sections were then incubated for 72 h at 4 °C in PBS-TX containing the primary antibodies and 1% NHS/NGS (refer to Table I for details of primary antibodies). Following 3x10 min of rinsing, the sections were incubated in the secondary antibody solution containing 1% NHS/NGS in PBS-TX for 4 h at RT. Sections were subsequently mounted and cover-slipped using methyl salicylate (Sigma-Aldrich, MO, USA) and examined using an epifluorescence (Olympus BX43) or confocal microscope (Leica SP8, Leica Microsystems).

--- insert Table I here ---

Retrogradely labeled neurons were tested for different molecules listed in Table I. PV, CB, or AT-rich sequence-binding protein-1 (SATB1) immunoreactivity was tested to determine non-cholinergic, putative GABAergic neurons. ChAT immunoreactivity was tested to determine the cholinergic projection neurons. Leu-enkephalin was used as regional marker for VP (Fig. 1B). We used the following secondary antibodies: goat anti-rabbit Alexa Fluor 405 (1:250; A31556, Invitrogen), donkey anti-rabbit Alexa Fluor 488 (1:250; ab150073; Abcam), donkey anti-goat Cy3 (1:250; 705-165-147; Jackson ImmunoResearch Laboratories), donkey anti-goat DyLight650 (1:1000, ab96938, Abcam).

A set of sections from each brain were stained with DAPI or cresyl violet to aid histological identification of the injection sites and cytological differentiation of the BF nuclei. DAPI staining was performed by incubating sections in the DAPI solution (1:2000, D3571, ThermoFisher) for 10 minutes. The sections were rinsed in PBS 3 times (10 min each) at RT and cover-slipped. For cresyl violet staining, the sections were mounted on slides 3 days before the procedure and incubated for 1 min at 40 °C immediately before the staining. Slides were transferred through 100% ethanol (EtOH) (2 min), two sets of xylenes

(2 min each), 100% EtOH (2 min), 70% EtOH (2 min), 20% EtOH (2 min), dH₂O (1 min), cresyl violet solution (0.5 g cresyl violet acetate and 15 ml acetic acid in 500 ml dH₂O, 15 min), differentiation solution containing 70% EtOH and 10% acetic acid (10 s), differentiation solution containing 100% EtOH and 10% acetic acid (10 s), 100% EtOH (5 min) and two set of xylenes (5 min each). Slides were then cover-slipped using Entellan new (Merck) mounting medium and examined under a light microscope.

Microscopy

Initial observations were performed with Olympus cellSens Imaging Software v2.2 using an epifluorescence microscope (Olympus BX43) equipped with a monochrome CCD camera (Olympus XM10). The images were obtained with 4x (Plan Apochromat, N.A. = 0.02, Nikon), 10x (Plan Fluor, N.A. = 0.30, Nikon), and 20x (Plan Fluor, N.A. = 0.50, Nikon) objective lenses. The 4x objective lens was used for histological analysis, and 10x and 20x objective lenses were used to locate retrogradely labeled neurons in the target basal forebrain nuclei. Four fluorescent filter sets (for DAPI, Alexa Fluor 488, Cy3, and Cy5) were used for the detection of Alexa Fluor 405 fluorophores and DAPI, Alexa Fluor 488 fluorophores and green Retrobeads, Cy3 fluorophores and red Retrobeads, and DyLight 650 fluorophores respectively.

Following wide-field epifluorescence microscopic observations, multichannel fluorescence images were acquired with a Leica SP8 confocal microscope (Leica Microsystems, Wetzlar, Germany) using the LAS X software (Leica Microsystems) at a minimum pixel resolution of 1024x1024. The images were obtained with 20x (Plan Fluotar, N.A. = 0.4, dry, Leica Microsystems) or 40x (Plan Apochromat, N.A. = 1.10,

water-immersion, Leica Microsystems) objective lenses. We used four distinct lasers at wavelengths of 405, 488, 552, and 638 nm in conjunction with PMT or HyD sensors to visualize the fluorescence signal. The pinhole size was set at 1 Airy unit. When z-stacks were acquired, we set the z-stack step size at half the optical section thickness. Post-acquisition brightness and contrast adjustments were performed uniformly on the whole image using the “FIJI” (Schindelin et al. 2012) distribution of the ImageJ software. No non-linear or selective image adjustments were made on the acquired images.

Cell quantification

Retrogradely labeled neurons were manually counted in every other coronal section spanning the target basal forebrain nuclei: VP, SI, horizontal diagonal band (hDB), lateral preoptic nucleus (LPO), and hypothalamic medial preoptic nucleus/area (MPO/MPA). Neuron quantification in the rostral-most parts of the extended amygdala was included in the SI. Cell counts were added together to obtain a total labeled neuron value for each region of interest. Normalized counts were derived by dividing the total number of labeled somata quantified in each nucleus by the number of observed sections. A similar quantification method was followed for the immunolabeled neurons. For each section, we counted all the cell bodies that were immunoreactive for a molecular marker in each region and noted the number of neurons that show colocalization with Retrobeads. For each BF nucleus, we then calculated the percentage of neurons expressing each tested molecular marker among the observed retrogradely labeled neurons projecting to the LA, BL, CeA

or the cBNST. Drawings depicting the distribution of labeled neurons in the BF were made with a camera lucida. All figures were created using Adobe Illustrator (v 25.0).

Model Implementation

BLA network model Based on our observations in the anatomical study showing that there were significant non-cholinergic inputs from the BF with a dense putative GABAergic projection to the basolateral amygdala and utilizing previous anatomical information, we developed a 1000-neuron BLA network model using cellular and microcircuit parameters that include intrinsic (within BLA) and extrinsic (afferents to BLA) connectivity and synaptic strengths. The network model was run on the parallel NEURON 7.7 simulator (Carnevale and Hines 2006) and the Allen Institute's Brain Modeling Toolkit (BMTK) with a fixed time step of 0.1 μ s. We used the python package "BMTools" to verify network connectivity parameters and generate plots. For the neuron power spectrum density and frequency analyses, we calculated spectrums using the Welch Periodogram method (pwelch in MATLAB). Additional analysis and plots were generated in python. The full model is available for download through GitHub at <https://github.com/tjbanks/AmygdalaTheta>.

Single cell models

Principal neurons (PN) of the BLA ($n = 800$) were modeled in addition to three groups of interneurons: PV+ Basket cells ($n = 93$), CR+ interneurons that include interneuron-specific interneurons (ISI) and small cholecystokinin (CCK)-expressing cells ($n = 56$), and somatostatin (SOM)-expressing interneurons that include neurogliaform cells (NGFC; $n = 51$). Model neuron parameters are provided in Table III.

Principal neurons had three compartments: soma (diameter 24.75 μm , length 25 μm), a proximal dendrite (diameter 3 μm ; length 270 μm), and an apical dendrite (diameter 5 μm ; length 555 μm) to match passive properties. Values of specific membrane resistance, membrane capacity and cytoplasmic (axial) resistivity were, respectively, $R_m = 40 \pm 5 \text{ k}\Omega\text{-cm}^2$, $C_m = 2.4 \mu\text{F/cm}^2$, and $R_a = 150 \Omega\text{-cm}$. Leakage reversal potential (E_L) was set to -75 $\pm 4 \text{ mV}$. The resulting V_{rest} was $-66 \pm 4 \text{ mV}$ for both types A and C cells, and the input resistance (R_{IN}) was $140 \pm 20 \text{ M}\Omega$ and $360 \pm 20 \text{ M}\Omega$, and time constant (τ_m) was $\sim 30 \text{ ms}$ and $\sim 20 \text{ ms}$, for Type-C and Type-A cells, respectively. All of these values were within the ranges reported in physiological studies (Washburn and Moises 1992). Soma and dendrite compartments had the following currents: leak (I_L), voltage-gated persistent muscarinic (I_M), high-voltage activated Ca^{2+} (I_{Ca}), spike-generating sodium (I_{Na}), potassium delayed rectifier (I_{DR}), A-type potassium (I_A) (Li et al. 2009; Power et al. 2011) and hyperpolarization-activated nonspecific cation (I_h) current. In addition, the soma had a slow apamin-insensitive, voltage-independent afterhyperpolarization current (I_{sAHP}) (Power et al. 2011; Alturki et al. 2016). The axonal compartments had the following currents: leak (I_L), high-threshold sodium ($I_{Na1.2}$), low-threshold sodium ($I_{Na1.6}$), and potassium delayed rectifier (I_{DR}) (Hu et al. 2009). PNs in the model had Type-A (adapting) and Type C (continuous) adaptation characteristic generated by adjusting magnitude of Ca^{2+} -dependent K^+ current, either 50 or 0.2 mS/cm^2 , respectively (Kim et al. 2013). PN models contained properties for low- and high- threshold oscillation to mimic physiological parameters as closely as possible (Pape et al. 1998; Li et al. 2009; Kim et al. 2013; Feng et al. 2016).

The PV+ interneuron model contained two compartments; a soma+axon (diameter 15 μm ; length 15 μm) and a dendrite (diameter 10 μm ; length 150 μm). Each compartment contained a fast Na⁺ (I_{Na}) and a delayed rectifier K⁺ (I_{KDR}) current. Passive membrane properties of PV+ interneurons were $R_m = 20 \pm 1$ and $20 \pm 1 \text{ k}\Omega\text{-cm}^2$, $C_m = 1$ and $1 \mu\text{F/cm}^2$, $R_a = 3375$ and $150 \Omega\text{-cm}$, for soma and dendrite, respectively. The resulting V_{rest} was -70 mV, input resistance (R_{IN}) was $371 \text{ M}\Omega$, and time constant (τ_m) was 20 ms. The passive properties and current injection responses (F-I curve) were all within the ranges in biological reports (Faber et al., 2001; Sah et al., 2003)

The CR+ interneuron model contained three compartments; a soma+axon (diameter 10 μm ; length 20 μm) and two dendrites (diameter 3 μm ; length 250 μm). Each compartment contained l-calcium current, fast Na⁺ (I_{Na}), persistent Na⁺ (I_{NaP}), h channel (I_h), potassium delayed rectifier current (I_{KDR}), voltage-independent afterhyperpolarization current (I_{sAHP}), voltage-gated persistent muscarinic current (I_M), and persistent Ca²⁺ current (I_{CaS}). Passive membrane properties were $R_m = 80 \pm 1 \text{ k}\Omega\text{-cm}^2$, $C_m = 1 \mu\text{F/cm}^2$ and $R_a = 150 \Omega\text{-cm}$. The resulting V_{rest} was -60 mV, input resistance (R_{IN}) was $321 \text{ M}\Omega$, and time constant (τ_m) was 20 ms. These passive properties and current injection responses (F-I curve) were all within the ranges in biological reports (Caputi et al. 2008)

The SOM+ interneuron model contained three compartments; a soma+axon (diameter 10 μm ; length 20 μm) and two dendrites (diameter 3 μm ; length 250 μm). Each compartment contained l-calcium current, fast Na⁺ (I_{Na}), persistent Na⁺ (I_{NaP}), h channel (I_h), potassium delayed rectifier current (I_{KDR}), voltage-independent afterhyperpolarization current (I_{sAHP}), voltage-gated persistent muscarinic current (I_M), and persistent Ca²⁺ current (I_{CaS}). Passive membrane properties were $R_m = 80 \pm 1 \text{ k}\Omega\text{-cm}^2$, $C_m = 1.3 \mu\text{F/cm}^2$

and $R_a = 150 \Omega\text{-cm}$. The resulting V_{rest} was -70 mV, input resistance (R_{IN}) was $290 \text{ M}\Omega$, and time constant (τ_m) was 19 ms. These passive properties and current injection responses (F-I curve) were all within the ranges in biological reports (Fanselow et al. 2010)

--- insert Table II here: Model neuron parameters ---

Intrinsic and Synaptic currents

The dynamics for each compartment (soma or dendrite) followed the Hodgkin-Huxley formulation as previously described (D. Kim et al., 2013) in eqn. 1,

$$C_m dV_s/dt = -g_L(V_s - E_L) - g_c(V_s - V_d) - \sum I_{cur,s}^{int} \sum I_{cur,s}^{syn} I_{inj} \quad (1)$$

where V_s/V_d are the somatic/dendritic membrane potential (mV), $I_{cur,s}^{int}$ and $I_{cur,s}^{syn}$ are the intrinsic and synaptic currents in the soma, I_{inj} is the electrode current applied to the soma, C_m is the membrane capacitance, g_L is the conductance of the leak channel, and g_c is the coupling conductance between the soma and the dendrite (similar term added for other dendrites connected to the soma). The intrinsic current $I_{cur,s}^{int}$ was modeled as $I_{cur,s}^{int} = g_{cur} m^p h^q (V_s - E_{cur})$, where g_{cur} is its maximal conductance, m its activation variable (with exponent p), h its inactivation variable (with exponent q), and E_{cur} its reversal potential (a similar equation is used for the synaptic current $I_{cur,s}^{syn}$ but without m and h). The kinetic equation for each of the gating variables x (m or h) takes the form but without m and h). The kinetic equation for each of the gating variables x (m or h) takes the form

$$\frac{dx}{dt} = \frac{x_\infty(V, [Ca^{2+}]_i) - x}{\tau_x(V, [Ca^{2+}]_i)} \quad (2)$$

where x_∞ is the steady state gating voltage- and/or Ca^{2+} - dependent gating variable and τ_x is the voltage- and/or Ca^{2+} - dependent time constant. The equation for the dendrite follows the same format with ‘ s ’ and ‘ d ’ switching positions in eqn. 1.

Excitatory transmission was mediated by AMPA and NMDA receptors, while inhibitory transmission by GABA_A receptors. The corresponding ionic currents were modelled by dual exponential functions (Destexhe et al. 1994; Durstewitz et al. 2000), as shown in eqns. 3-5

$$\begin{aligned} I_{AMPA} &= w \times G_{AMPA} \times (V - E_{AMPA}) \\ G_{AMPA} &= g_{AMPA,max} \times F_{AMPA} \times r_{AMPA} \\ r_{AMPA} &\doteq \alpha T_{max,AMPA} \times ON_{AMPA} \times (1 - r_{AMPA}) - \beta_{AMPA} \times r_{AMPA} \end{aligned} \quad (3)$$

$$\begin{aligned} I_{NMDA} &= w \times G_{NMDA} \times (V - E_{NMDA}) \\ G_{NMDA} &= g_{NMDA,max} \times F_{NMDA} \times s(V) \times r_{NMDA} \\ r_{NMDA} &\doteq \alpha T_{max,NMDA} \times ON_{NMDA} \times (1 - r_{NMDA}) - \beta_{NMDA} \times r_{NMDA} \end{aligned} \quad (4)$$

$$\begin{aligned} I_{GABAa} &= w \times G_{GABAa} \times (V - E_{GABAa}) \\ G_{GABAa} &= g_{GABAa,max} \times F_{GABAa} \times r_{GABAa} \\ r_{GABAa} &\doteq \alpha T_{max,GABAa} \times ON_{GABAa} \times (1 - r_{GABAa}) - \beta_{GABAa} \times r_{GABAa} \end{aligned} \quad (5)$$

where V is the membrane potential (mV) of the compartment (dendrite or soma) where the synapse is located, I is the current injected into the compartment (nA), G is the synaptic conductance (μS), w is the synaptic weight (unitless), and E is the reversal potential of the synapse (mV). $g_{x,max}$ is the maximal conductance (μS), F implements short-term plasticity and r_x determines the synaptic current rise and decay time constants based on the terms αT_{max} and β (Destexhe et al. 1994). The voltage-dependent variable $s(V)$ which

implements the Mg²⁺ block was defined as: $s(V) = [1 + 0.33 \exp(-0.06 V)]^{-1}$ (Zador et al. 1990). The terms ON_{NMDA} and ON_{AMPA} are set to 1 if the corresponding receptor is open, else to 0. Previously published data were used to model reversal potential, rise/decay time constants and conductance (Feng et al. 2019; Galarreta and Hestrin 1997; Porter et al. 1998; Mahanty and Sah 1998; Thomson and Deuchars 1997; Weisskopf et al. 1999). For all connections, synaptic weight w was distributed log-normally with a cut off of three times the mean to prevent non-physiological values. The ionic current parameters are available in Table IV.

--- insert Table IV here: Ionic current parameters ---

Intrinsic connectivity

A 1000-neuron homogenous network model of the BLA was generated with a neuronal composition of 56.9% PN_A (n = 569), 23.1% PN_C (n = 231), 9.3% PV INs (n = 93), 5.6% CR+ (n = 56) and 5.1% SOM+ (n = 51). The PNs have mutual connections with all interneuron groups. PV+ interneurons target somata of the PNs and SOM+ interneurons and other PV+ cells, but not the CR+ group. CR+ interneurons form inhibitory synapses on all other neuron types, similar to PNs. SOM+ interneurons only target PNs and avoid other interneuron groups. Connectivity with interneurons were restricted to ~300 µm. The probability of unidirectional or reciprocal synaptic connections between PNs and interneurons was set to 16%. Axonal conduction delay was distance-dependent using a conduction velocity of 500 µm/ms. Synaptic connectivity parameters are listed in Table II.

In order to combat edge effects, a “shell” of virtual neurons was generated around the “core” of true biophysical neurons. Virtual shell neurons were distributed uniformly in

the same way core neurons were and were connected to core neurons using the same synaptic parameters and connectivity rules as core-to-core neurons were. Shell neurons fire at a Poisson rate coinciding with network quiet-waking firing rates (mean, sigma for PNs: 1, 0.8; PV+ interneurons: 30, 13; CR+ interneurons: 20, 4; SOM+ interneurons: 2, 1).

--- insert Table III here: Synaptic connectivity parameters ---

Extrinsic connectivity

Input 1: Thalamic/cortical glutamatergic afferents

Thalamo-cortical afferents were glutamatergic and were modeled as independent 2 Hz Poisson trains, delivered to each PN, SOM, and CR cell, but not PV cell (Fig. 1)

Input 2: Cholinergic innervation

The effects of ACh were simulated by changing the relevant synaptic conductances, following prior work (Hummos et al. 2014). For affected synapses, the synaptic current was multiplied by a factor as listed below, for both i_{amp} and i_{GABA} . For example, in the case of i_{amp} , we get Eqn. 7 below (replace amp with GABA for the inhibitory synapses),

$$i_{amp} = i_{amp} * (1 + b_{ACh} * (ACH - 1)) \quad (7)$$

In Eqn. 7, b_{ACh} and ACH together control the strength and sign for the various ACH cases. For instance, via the equation, an ACH value of 2 allows b_{ACh} to influence i_{amp} positively, to make no change with $ACH = 1$, and to influence i_{amp} negatively with $ACH = -0.2$. The specific b_{ACh} values (same for all ACH cases) and the corresponding synapses were as follows: 0.3 for all the thalamo-cortical afferent synapses, 0.3 for PV-PN and VP/SI-PN, 0.4 for SOM-PN and CR-PN, and 0.3 for VP/SI-PV synapses.

Input 3: VP/SI GABAergic rhythmic innervation

Rhythmic GABAergic input from the VP was designed using methods described by (Fink et al. 2015). Input was set to a specified frequency, and each cell responded to the input with "jitter" to represent intercellular variability. Jitter was Gaussian normal distributed (N) for each cell, with zero mean and SD σ_{jitter}^2 . The time of the jth event of neuron i was given by:

$$t_j^i = jT + N(0, \sigma_{jitter}^2) \quad (8)$$

A total of 893 afferent cells were designed to individually exhibit independent 2 Hz Poisson activity. The afferents project onto 800 PN and 93 Int Basket cells with an average convergence of 1 and 10.1 cells, respectively. Two states were considered for these afferents, the non-modulated with each afferent being independent at 2 Hz as above. For the theta-modulated state the firing rate of the afferents were modulated with a sine wave:

$$r[t] = A * (\sin(2 * \pi * f * t) + \phi) + off \quad (9)$$

where $A = \frac{off}{d-1}$, f is the frequency, t is a vector representing time, ϕ is the phase, off is the offset firing rate of the spike train being modulated and $0 < d < 1$ is the depth of modulation which represents the amplitude of the sine wave relative to off . We used a depth of modulation 0.7. To generate the spike train, a random vector $x[t]$ was generated with values uniformly distributed between 0 and 1. A spike was generated if $x[t] \leq r[t]dt$ where dt in our case was 0.1.

For experiments with theta-modulated VP input, jitter was applied at 8Hz. For all other experiments, no jitter was applied and VP input was 2Hz Poisson.

Input 4: Background input to all cells

To reproduce membrane potential fluctuation seen *in vivo*, we used a point conductance input onto the soma to imitate stochastic background synaptic activity using the Ornstein–Uhlenbeck process (Destexhe et al., 2001). Specifically, stochastic background input had two independent components, excitatory and inhibitory, for PNs and PVs, SOMs, and CR cells, as modeled previously by our group (Feng et al 2019). Conductance values, mean(std), for excitatory and inhibitory inputs for the cell types were as follows: PNa: 0.0032(0.003), 0.021(0.008); PNc: 0.0032(0.003), 0.021(0.008); PV: 0.00121(0.00012), 0.00573(0.00264); SOM: 0.00121(0.00012), 0.00573(0.00264); CR: 0.0032(0.003), 0.021(0.008).

Conduction delays

Conduction delays between cells were calculated and assigned in a distance-dependent manner:

$$D = \frac{\sqrt{(x_1-x_2)^2 + (y_1-y_2)^2 + (z_1-z_2)^2}}{A_V} \quad (6)$$

Where (x_1, y_1, z_1) and (x_2, y_2, z_2) are the coordinates of the pre and postsynaptic cells, respectively. A_V is the axonal conduction velocity (0.5 m/s).

Short-term plasticity

Modeled AMPA and GABA synapses exhibited short-term synaptic plasticity. We used previous reports to model short-term depression between PNs (Silberberg et al. 2004; Feng et al. 2019), and between PNs and interneurons (Cauli et al. 2014; Mahanty and Sah 1998; Silberberg et al. 2004; Fanselow et al. 2008; Woodruff and Sah 2007). Short-term facilitation was also implemented between PNs and interneurons (Ali and Thomson 1998; Cauli et al. 2014; Silberberg and Markram 2007; Minneci et al. 2007; Riedemann 2019).

For facilitation, the factor F was calculated using the equation: $\tau_F * dF/dt = 1 - F$ and was constrained to be ≥ 1 . After each stimulus, F was multiplied by a constant, f (≥ 1) representing the amount of facilitation per pre-synaptic action potential and updated as $F \rightarrow F*f$. Between stimuli, F recovered exponentially back toward 1. A similar scheme was used to calculate the factor D for depression: $\tau_D * dD/dt = 1 - D$ and D constrained to be ≤ 1 . After each stimulus, D was multiplied by a constant d (≤ 1) representing the amount of depression per pre-synaptic action potential and updated as $D \rightarrow D*d$. Between stimuli, D recovered exponentially back toward 1. We modelled depression using two factors d₁ and d₂ with d₁ being fast and d₂ being slow subtypes, and $d = d_1 * d_2$ and was constrained to be ≥ 1 . After each stimulus, F was multiplied by a constant, f (≥ 1) representing the amount of facilitation per pre-synaptic action potential and updated as $F \rightarrow F^*$.

LFP calculation

Transmembrane ionic currents from each compartment of the model neurons were produced by using the *extracellular mechanism* in NEURON (Carnevale and Hines 2006; Parasuram et al. 2016). The extracellular potential arising from each neuronal compartment was then calculated using the line source approximation method, which provides a better approximation than using point sources (Gold et al. 2006; Schomburg et al. 2012). The extracellular potential of a line compartment was estimated as

$$\phi_{EP} = \frac{I}{4\pi\sigma\Delta s} \log \left| \frac{\sqrt{h^2+r^2}-h}{\sqrt{l^2+r^2}-l} \right| \quad (9)$$

where, I denotes the transmembrane current from that compartment, Δs the length of the line compartment, r the radial distance from the line, h the longitudinal distance from the end of the line, and $l = \Delta s + h$ the distance from the start of the line (Parasuram et al.

2016). We chose conductivity σ of the extracellular medium as 0.3 S/m (Goto et al. 2010; Einevoll et al. 2013). The individual extracellular potentials were summed linearly (Lindén et al. 2014) at 0.5 ms resolution, to obtain \emptyset_{LFP_S} (eqn.10) as the LFP for an N -neuron network with n -compartment-cells.

$$\emptyset_{LFP_S} = \sum_{N=1}^{N_neurons} \sum_{i=1}^{n_source} \frac{I_{Ni}}{4\pi\sigma\Delta s_{Ni}} \log \left| \frac{\sqrt{h_{Ni}^2 + r_{Ni}^2 - h_{Ni}}}{\sqrt{l_{Ni}^2 + r_{Ni}^2 - l_{Ni}}} \right| \quad (10)$$

where N_i denotes i^{th} compartment of N^{th} neuron in the network.

Entrainment to LFPs

For calculating the entrainment and preferred phase of cells, we bandpass filtered the LFPs in the frequency band of 4 to 12 Hz using a 2 pole Butterworth filter implemented with the MATLAB function *filtfilt*, which performs forward and backward filtering to minimize phase distortion. A Hilbert transform of the resulting signal was then computed to determine the phase and amplitude at each instant (Amir et al., 2018). This was used to assign a phase to each spike from a neuron.

Computational Experiments

A series of computational experiments, labeled as Cases 1-6 below, were performed to characterize the roles of cell types and afferents in creating and modulating the theta rhythm in the amygdala. Each simulation run lasted 15 seconds, of which only the last 10 seconds were retained to avoid transients in the initial part. Each case was run with 10 random seeds and the averaged results are reported as mean and SD.

Case 1. Baseline state with 2 Hz Poisson input from the thalamocortical afferents, and a 2 Hz non-modulated Poisson input from VP/SI, both delivered as indicated in an earlier section (also see Fig. 1). This baseline case had cholinergic tone with ACH=1.

Case 2. Same as Case 1, but with the inhibitory VP/SI inputs as rhythmic with jitter as indicated earlier.

Case 3. Same as Case 2, but with cholinergic tone increased by setting ACH=2.

Case 4. Same as Case 2, but with cholinergic tone decreased by setting ACH=-0.2

Case 5. Same as Case 1 (without rhythmicity in the VP/SI input), but with cholinergic tone increased by ACH=2, instead of 1.

Case 6. Same as Case 1, but with cholinergic tone decreased by setting ACH=-0.2

Relative contributions of cell types to theta power

In this set of experiments, we inactivated different cell types sequentially to investigate their relative contributions to the peak theta power in the LFP. This was done by disconnecting all efferents from that particular cell type (see schematics). This causes the firing rates of the PNs to increase, and to bring them down to baseline levels for a fair comparison, we reduced the thalamo-cortical input to the PNs appropriately. We were successful in matching baseline firing rates using such a procedure as shown in the inset table in Fig. 6.

Results

Neuroanatomical Characterization

Retrograde labeling

Histological assessment revealed that the surgeries resulted in successful local injections into the target nuclei with negligible diffusion of Retrobeads to neighboring regions (see Fig. 1A-F). Retrobeads were observed to be retrogradely transported into the cell bodies of BF neurons following injections into the amygdaloid complex (Fig. 2A) and to other regions known to provide dense projections to the amygdaloid complex. Overall, we quantified 8485 basal forebrain neurons projecting to the LA (1243 cells from n = 3 animals), BL (795 cells from n = 4 animals), CeA (3040 cells from n = 2 animals), and the cBNST (3407 cells from n = 9 animals). The results showed that both the target amygdaloid nuclei and the cBNST received projections of varying density from each of the observed basal forebrain and preoptic nuclei (Fig. 1G-J), namely the VP, SI, hDB, LPO, and MPO/MPA.

The LA, BL, and CeA received the densest basal forebrain input from the SI (39% of labeled cells for the LA, 41% for the BL, and 43% for the CeA; Fig. 1G-I). VP constituted the second largest source of BF innervation for the amygdaloid nuclei (26% of labeled cells for both the LA and the BL, and 13% for the CeA, Fig. 1G-I). The LA-projecting neurons of the BF were overwhelmingly located (87%) in the non-hypothalamic BF nuclei with sparse labeling in the LPO (7%) and, MPO (6%). BF innervation of the BL followed a similar pattern: relatively dense SI (41%) and VP (26%) projections were followed by axonal projections arising from the LPO (13%), hDB (10%), and MPO/MPA (9%). CeA-projecting neurons were mostly located in the SI (43%). The CeA received

projections of relatively similar density from the MPO/MPA (17%), HDB (15%), and VP (13%).

The densest projections targeting the cBNST, unlike the amygdaloid nuclei, originated from the MPO/MPA (average of 25.74 cells per section, 56% of labeled cells; Fig. 1J). This was followed by projections from the LPO (14%), hDB (12%), and SI (12%) with a relatively small density of connections from the VP (average of 2.57 cells per section, 6% of labeled cells; Fig. 1J). The majority of the cBNST-targeting neurons of the SI was located in the dorsal, as opposed to the ventral, portions of SI.

We observed multiple instances of proximal labeling of red and green beads (Fig. 1K-M), but only 2 out of 8485 neurons were co-labeled with red and green beads in their cell bodies in the hDB (not shown). This suggests that the axonal processes of the amygdala- or cBNST-targeting BF neurons rarely bifurcate to target both structures, however, there may exist double cBNST- and amygdaloid nuclei-targeting neurons in other brain regions that we have not tested.

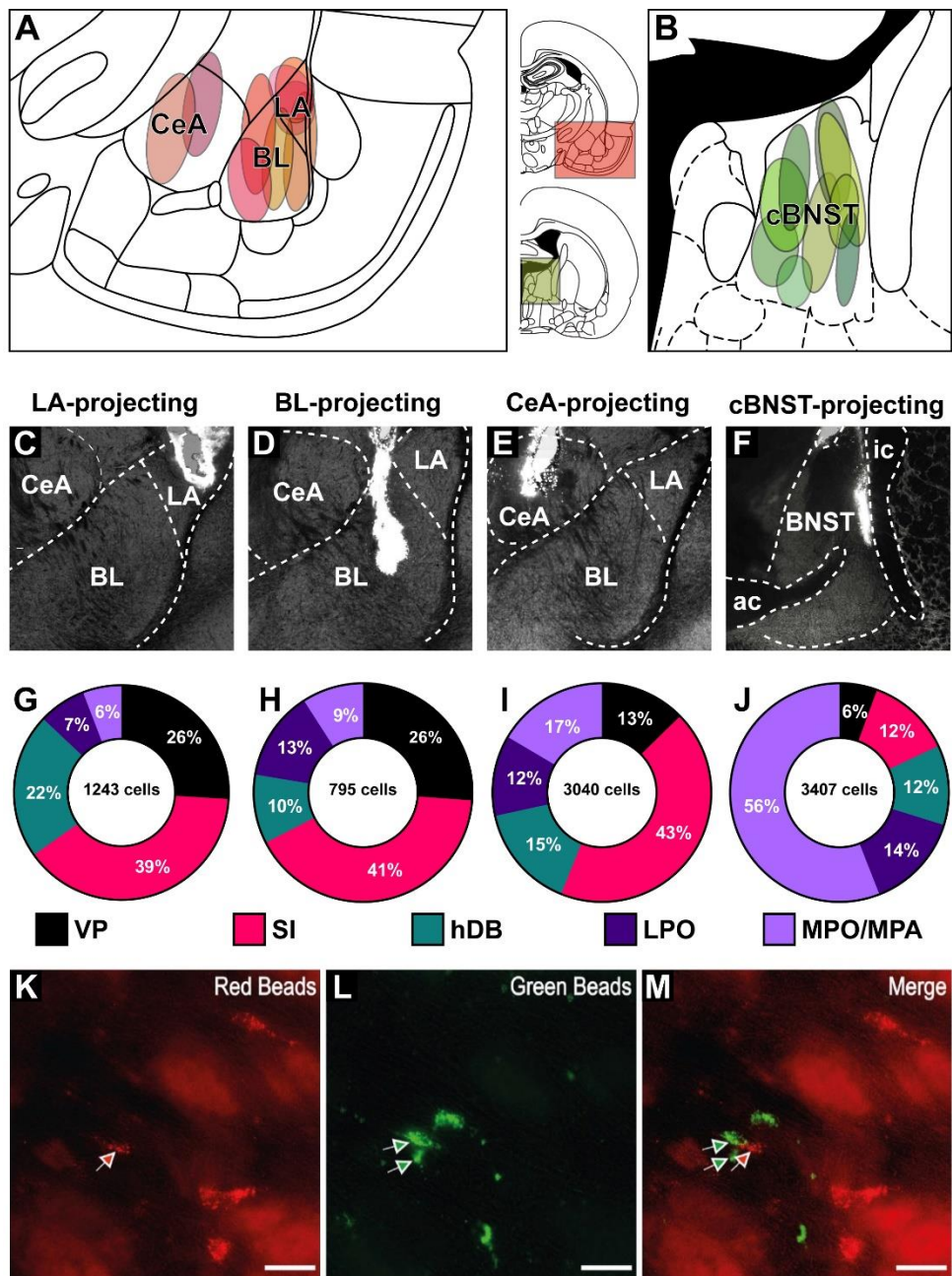


Figure 1 Retrobead injections and resulting retrograde labeling in the basal forebrain and preoptic nuclei. **A-B** Injection sites targeting the amygdala nuclei (A) and the cBNST (B). **C-F** Brightfield photographs of representative injections in the LA (C), BL (D), CeA (E) and cBNST (F). **G-J** Donut charts demonstrating the percentage of LA (G), BL (H), CeA (I) and cBNST (J) targeting neurons in the observed basal forebrain and preoptic nuclei. **K-M** Fluorescent micrographs of retrogradely labeled neurons with red (K) or green (L) Retrobeads. ac, anterior commissure; ic, internal capsule.

Neurochemical characterization

Neurochemical profiles of the retrogradely labeled BF neurons were identified with immunohistochemistry for ChAT and biomarker molecules that are localized in subpopulations of putative GABAergic neuron. We tested a total number of 2226 neurons that were labeled in the VP, SI, or hDB following Retrobeads injections into the LA (582 neurons from n = 2 animals), BL (313 neurons from n = 2 animals), CeA (1068 neurons from n = 2 animals) and the cBNST (753 neurons from n = 7 animals) for PV (1062 neurons), CB (1073 neurons), ChAT (489 neurons) or SATB1 (91 cells) immunoreactivity (Table V).

Our observations showed that, overall, ChAT-immunopositive neurons constituted 23.9% of all amygdaloid-nuclei- or cBNST-targeting basal forebrain neurons in the VP, SI and HDB. We observed that 1.3% of the tested BF neurons projecting to the LA, BL, CeA, or cBNST showed immunoreactivity for PV, while 5.5% of all tested basal forebrain projection neurons were CB-immunoreactive (Table V). No retrogradely labeled neuron was immunoreactive to SATB1. We did not observe any double labelling of PV and ChAT or CB and ChAT in any of the double-labelled sections we have observed.

--- insert Table V here ---

When we tested amygdaloid nuclei- or cBNST-projecting neurons for ChAT immunoreactivity (Table V), we found that a major portion of the projecting cells were ChAT+ irrespective of the source or target region of the projection. The BL received the densest cholinergic projection, such that 46.9% of all BL-projecting BF cells in the VP, SI and hDB were ChAT+ (47.6% in the VP, 44.8% in the SI, 43.8% in the HDB). This was followed by LA- (overall 22.6%; 29.5% in the VP, 29.2% in the SI, 13.1% in the hDB), cBNST- (overall 18.4%; 12.5% in the VP, 18.2% in the SI, 20.0% in the hDB), and CeA

projecting (overall 16.3%; 15.3% in the VP, 15.7% in the SI, 20.8% in the hDB) ChAT+ BF neuronal subpopulations.

Our immunohistochemical investigations (Fig. 2B-P, Table V) further revealed that 5.25% of LA-projecting neurons and 4.1% of BL-projecting neurons in the VP were immunoreactive for PV, whereas 7.5% of the BL-targeting SI neurons were PV+ (Fig. 2E-H, Fig. 3A-D, Fig. 3I-L). Interestingly, none of the tested LA-projecting SI neurons were PV+. We also did not observe any PV+ LA- or BL-projecting neurons in the hDB. Amongst the CeA-projecting BF neurons, approximately 1% of labeled cells in the SI and 1.5% in the hDB were immunopositive for PV, whereas no PV+ CeA-targeting neuron was observed in the VP. In contrast to amygdala-targeting BF neurons among which subpopulations of PV+ neurons existed, not a single cBNST-projecting neuron in any of the observed nuclei (VP, SI, and hDB) showed immunoreactivity for PV.

When we tested the basal forebrain projection neurons labeled with Retrobeads for CB immunoreactivity, we found that a considerable portion of the retrogradely labeled cells were CB+ in several regions (Fig. 3E-L, Table V). Most significantly, CB+ neurons constituted 21.2% of all projections to the BL originating from the VP and 6.5% of those originating from the SI. Similarly, 6.8% of LA-projecting SI neurons were immunopositive for CB, whereas no labeled LA-projecting cell in the VP was CB+. In the hDB, a very small portion of LA-projecting neurons were immunopositive for CB (1.3%), but none of the observed BL projecting neurons were CB+. Small subsets of CeA-projecting neurons in all tested nuclei express CB (7.8% in the VP, 7.4% in the SI, 4.4% in the hDB). The cBNST-targeting CB+ basal forebrain neurons were mostly localized to the SI with CB+ neurons making up 5.7% of the cBNST-projecting-neurons in SI. Virtually no other

cBNST-projecting BF neuron was immunopositive for CB (0.0% in the VP, 0.7% in the hDB).

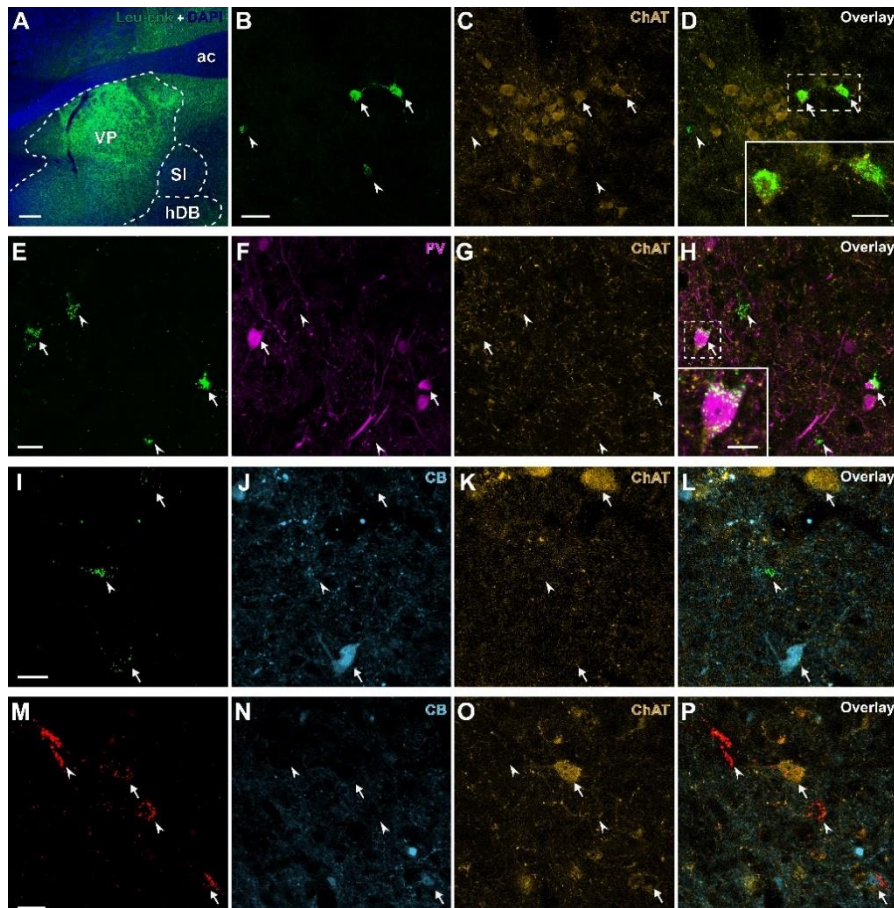


Figure 2 Confocal microscopic images of retrogradely labeled BF neurons (green or red) tested for ChAT (orange), PV (magenta) and CB (cyan) immunoreactivity. Arrows and arrowheads respectively point to retrogradely labeled neurons immunopositive or immunonegative for tested biomarker molecules. **A** Confocal microscopic tile-scan image showing dense labeling of Leu-enkephalin fibers in the VP. **B-D** LA-targeting neurons (B) tested for ChAT (C). Two retrogradely labeled ChAT+ neurons (D) are enlarged in the inset. **E-H** BL-targeting neurons (E) tested for PV (F) and ChAT (G). One of the two labeled PV+ neurons (H) is enlarged in the inset. **I-L** CeA-targeting neurons (I) tested for CB (J) and ChAT (K), showing one CB+ and one ChAT+ retrogradely labeled neuron. **M-P** cBNST-targeting neurons (M) tested for CB (N) and ChAT (O), showing one CB+ and one ChAT+ retrogradely labeled neuron. Scale bars: A, 200 µm; B-D, 40 µm; D inset, 20 µm; E-H, 20 µm; H inset, 10 µm; I-L, 15 µm; M-P, 20 µm. ac, anterior commissure; hDB, nucleus of horizontal limb of the diagonal band of Broca; SI, substantia innominata; VP, ventral pallidum

There exists a subpopulation of non-cholinergic SATB1-positive neurons in the hDB (Huang et al. 2011). We observed that a significant portion of the cBNST-targeting non-hypothalamic basal forebrain neurons (approximately 40%) were located in the hDB. To explore whether these non-cholinergic SATB1+ neurons project to the cBNST, we tested cBNST-targeting basal forebrain neurons ($n = 91$) for SATB1 immunoreactivity. Among the cBNST-projecting neurons tested for SATB1, we did not observe any neurons that were immunopositive for SATB1 in the VP, SI or the hDB.

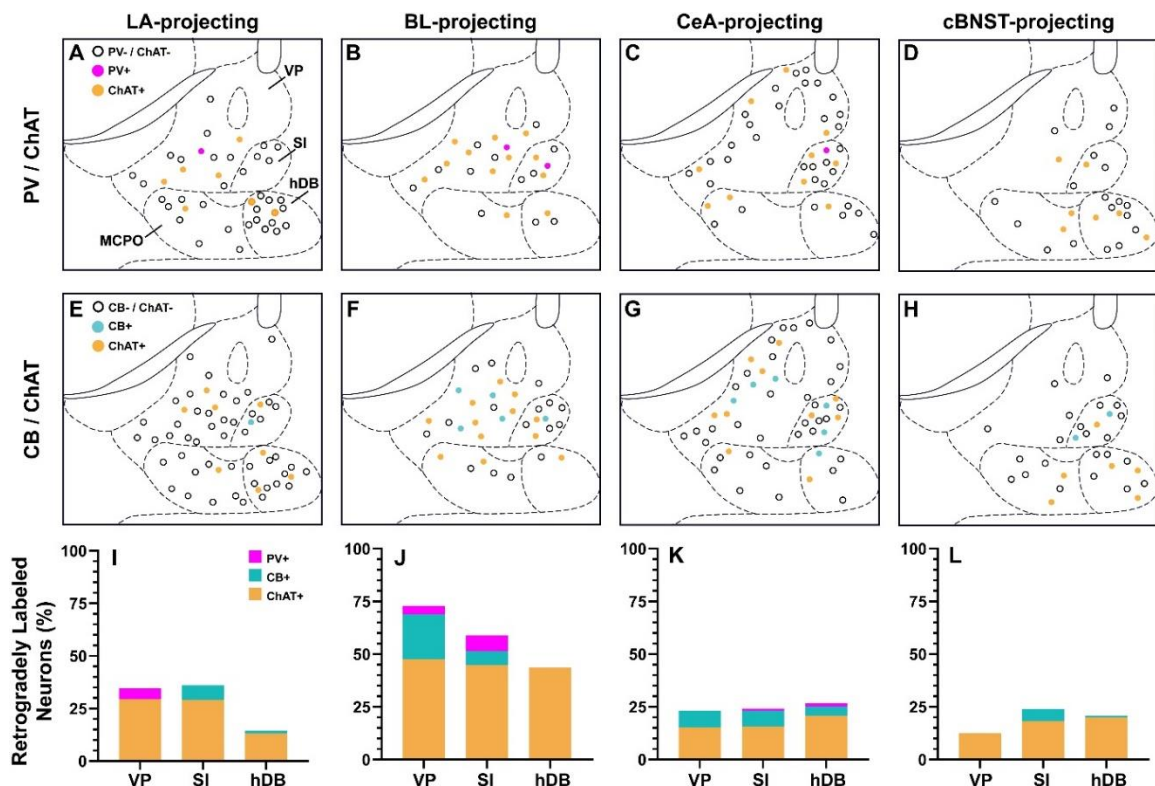


Figure 3 Distribution and proportion of retrogradely labeled neurons in the observed basal forebrain nuclei. **A-H** Schematic maps depicting LA (A, E), BL (B, F), CeA (C, G) and cBNST (D, H) targeting neurons tested for PV and ChAT (A-D) or CB and ChAT (E-H). Labeled cells in neighboring structures are omitted. **I-L** Percentage of PV (magenta), CB (cyan) and ChAT (orange) immunopositive cells within the tested LA (I), BL (J), CeA (K) and cBNST (L) targeting neurons.

Computational Investigation

Development and validation of amygdala network model to study role of VP/SI projection

We developed a biophysically model of the BLA based on known anatomy, and channel and synaptic neurophysiology, as detailed in methods. The model included both high and low adapting PNs, and two interneuron types, fast spiking PV and low-threshold spiking SOM and CR cells, adapted from our prior models (Feng et al., 2016 Neuroscience; Feng et al., 2019, eNeuro). These represent known cell types implicated in oscillatory dynamics in the amygdala (Feng et al., 2019, eNeuro). The three afferents relevant to our hypothesis were random Poisson type from the thalamocortical regions, and rhythmic GABAergic as well as cholinergic from the VP/SI region (Fig.1). Excitatory transmission was mediated by AMPA/NMDA receptors, and inhibitory transmission by GABA_A receptors. Model synapses in all intrinsic connections also exhibited short term pre-synaptic plasticity (STP). Excitatory synapses from PN to FSI and FSI to PN had depression while those from PN to LTS and LTS to PN had facilitation (**Fig. 1C**). Electrical synapses (gap junctions) were included within FSI, LTS cell populations. Local field potential (LFP) was calculated at the center of the network using line source approximation. To account for lack of afferents in the edge of the model, a shell of ‘virtual’ cells (Billeh, Yazan N., et al., 2020) surrounds the network. These virtual cells do not contribute to calculated properties such as average firing rates and LFP.

The passive and current injection properties of single cells matched reports in the literature. Sample current injection plots for the five cell types are provided in Figure 4 (see methods for values related to the properties).

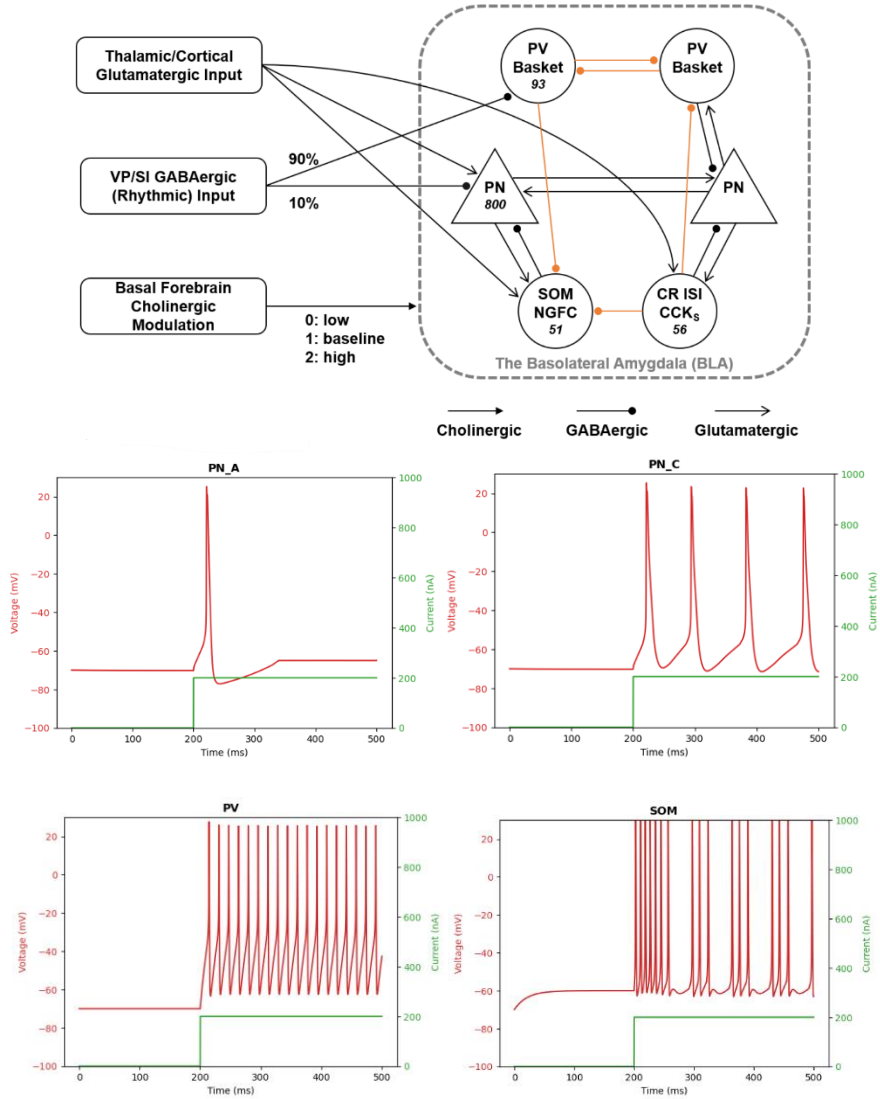


Figure 4 Synaptic connectivity of the network, single unit activity of model cells, and VP/SI inputs **A** Schematic showing the synaptic connectivity of the network. PN denotes Principal Neurons. Three most populous interneuron groups of the amygdala are included: parvalbumin- (PV), somatostatin- (SOM), and calretinin- (CR) containing interneurons. **B** Action potential firing patterns of model amygdala neurons (PN_A, PN_C, PV, SOM, CR). **C-D** Activity of neurons constituting the external VP/SI GABAergic input in the baseline (C) and theta-modulated (D) cases.

Rhythmic GABAergic and cholinergic projections from VP/SI alter BLA dynamics differentially.

Results related to the firing rates of cell types, and the PSD from the LFP plots for the six cases highlighting our hypothesis are listed next. In the various cases described

below, the network configuration and parameters remain the same (see methods for numbers) unless specified otherwise, with only the synaptic weights between specific connections changed.

Raster plots of the cell types in the network for the six different cases (Fig. 5) show considerable variation. For baseline case 1, where the VP/SI input was 2 Hz random Poisson without modulation, no rhythmicity in firing is seen among the cell types. With modulation added, case-2, rhythmicity begins to appear, and gets stronger in case-2 with ACH-High. Then it diminishes with ACH-Low in case-4, and in cases 5 (no VP/SI input, ACH-High) and 6 (no VP/SI and ACH-Low), theta power is completely abolished.



Figure 5 Single cell firing properties in experimental cases. **A** Example spike raster plots of different amygdala principal neuron and interneuron types in the 6 experimental cases. **B** Histogram plots of the firing rates of different amygdala principal neuron and interneuron types in the 6 experimental cases.

To further characterize the modulation of theta by the amygdala network, we calculated the PSD of the local field potential. PNs are the primary contributors to the LFP and so the PSD plots reflect the power contributed to the specific bands by synchronous firing among the PNs. As expected, without rhythmicity in the VP/SI inputs, theta was

absent in the PSD for case 1 (panels A2, A3). However, with the introduction of rhythmicity in the VP/SI input in Case 2, theta is evident in the PSD in the baseline ACH case (panel A3). Higher cholinergic tone (ACH=3, Case 3), more than doubled the theta power (panel A3), and a lower cholinergic tone (ACH=0, Case 4) decreased it to baseline levels. We then investigated the effect of removal of the rhythmic component of the VP/SI input at the high (ACH=2; Case 5) and low (ACH=0) levels. This decreased the theta power considerably and brought the theta power to baseline levels in both cases 5 and 6. This indicates that ACH had no effect on power in the theta band in the absence of the theta rhythm in VP/SI input.

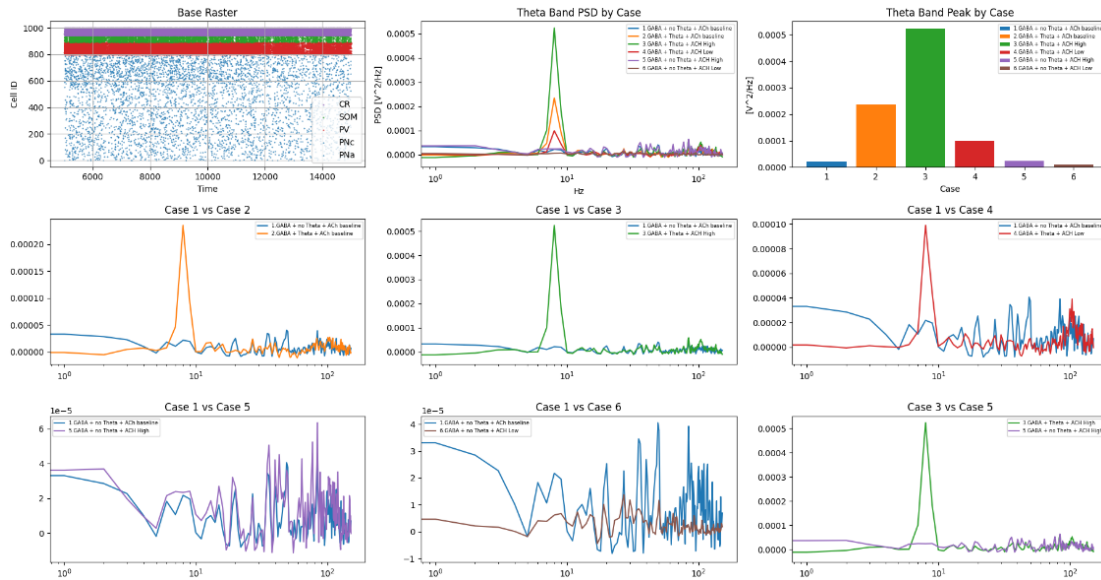


Figure 6A Power spectrum of the amygdala neuronal population. The resulting average population power spectra of the 6 experimental cases over 10 network instantiations.

We next explored the entrainment of the various cell types to the amygdalar theta using the Hilbert transform (see methods). As expected, both types of PNs spiked at the trough of theta when inhibition waned (Fig. 6-left; Feng et al., 2019 eNeuro). The raster plots in the right panels of Fig. 6 provide an estimate of the temporal spread of entrainment.

PVs cells spiked about 45^0 after the trough consistent with the fact that they received most of their drive from PNs. The SOM cells follow them and spike around the peak of the theta rhythm, and CR cells seem to spike in between PV and SOM cells.

Finally, the VP/SI input did not entrain to theta since the LFT theta rhythm had varying frequencies through time due to the interactions between the various cell types (Fig. 6B, bottom). An analysis of the theta cycles in the LFP revealed that the frequencies and amplitudes of varied considerably, with frequency variation of 8 ± 4 Hz. This results in the VP/SI afferents, with their narrow-band frequency of 8 ± 1 Hz (left-bottom panel of Fig. 6) not exhibiting any phase preference.

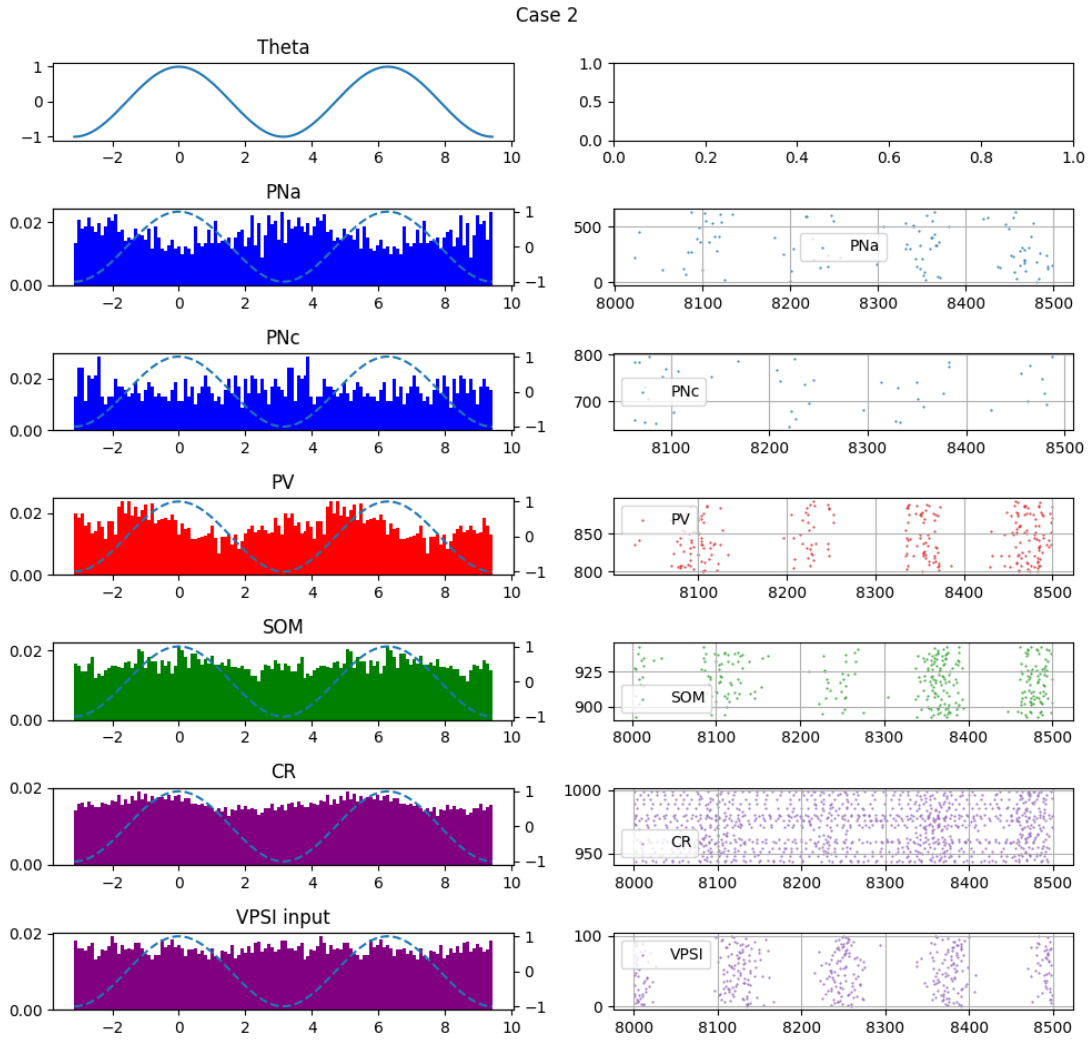


Figure 6B Theta phase-couplings of different principal neuron and interneuron groups. Plots showing the firing patterns and theta-phase precession/succession tendencies of the modeled amygdala neuronal subpopulations.

We explored the phase preferences of the amygdala cell types further using cross-correlation and coherence measures (Fig. 7, top and bottom rows). Cross-correlation estimates revealed that the PNs precede the PV, SOM, and CR cells by 4.5, 6 and 6 ms, respectively. Also, the PV cells were found to precede the SOM cells by 3 ms.

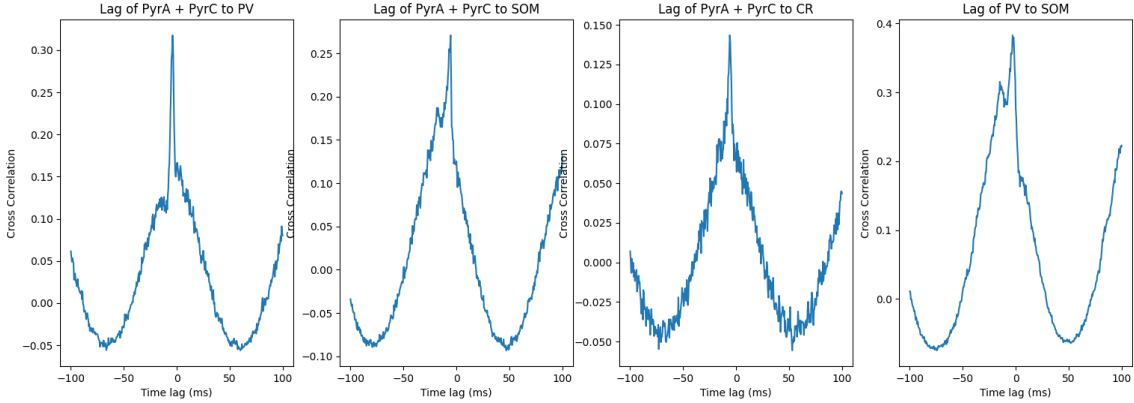


Figure 7 Coherence of different amygdala neuronal units. **A.** Cross correlation of units in the baseline and theta-modulated VP/SI + high ACh cases (*2 cases to be graphed in the same plot*).

The theta rhythm from VP/SI is modulated by the microcircuitry in the amygdala as shown in Figures 6 and 7. We explored the relative contributions of each cell type to this modulation by inactivating different cell types sequentially and documenting the effect on the peak power in LFP theta. Since the contribution to the LFPs is almost solely from PNs, they were not inactivated. Instead, in each inactivation experiment involving other cell types, we adjusted the thalamo-cortical input to PN cells to restore PN firing rates to baseline levels with each inactivation, for a fair comparison. For instance, when inactivating the PV cells, the thalamo-cortical firing rates to PNs were adjusted to bring their average firing rate of PNa and PNC cell types to baseline levels of 0.45 and 0.6 Hz, respectively. Results from this model experiment runs are shown in Figure 8, with the inset table listing the firing rates of the various cell types for the different cases. The PV cells contributed the most to theta power. This was perhaps a consequence of the afferent connectivity from VP/SI converging primarily onto PVs (Fig. 4), forming a key pathway for amygdala to entrain to theta. On the other hand, SOM cells were found to contribute

minimally to theta. Paradoxically, inactivation of CR+ cells increased theta compared to baseline levels perhaps due to increased activity of PV cells caused by the disinhibitory effect.

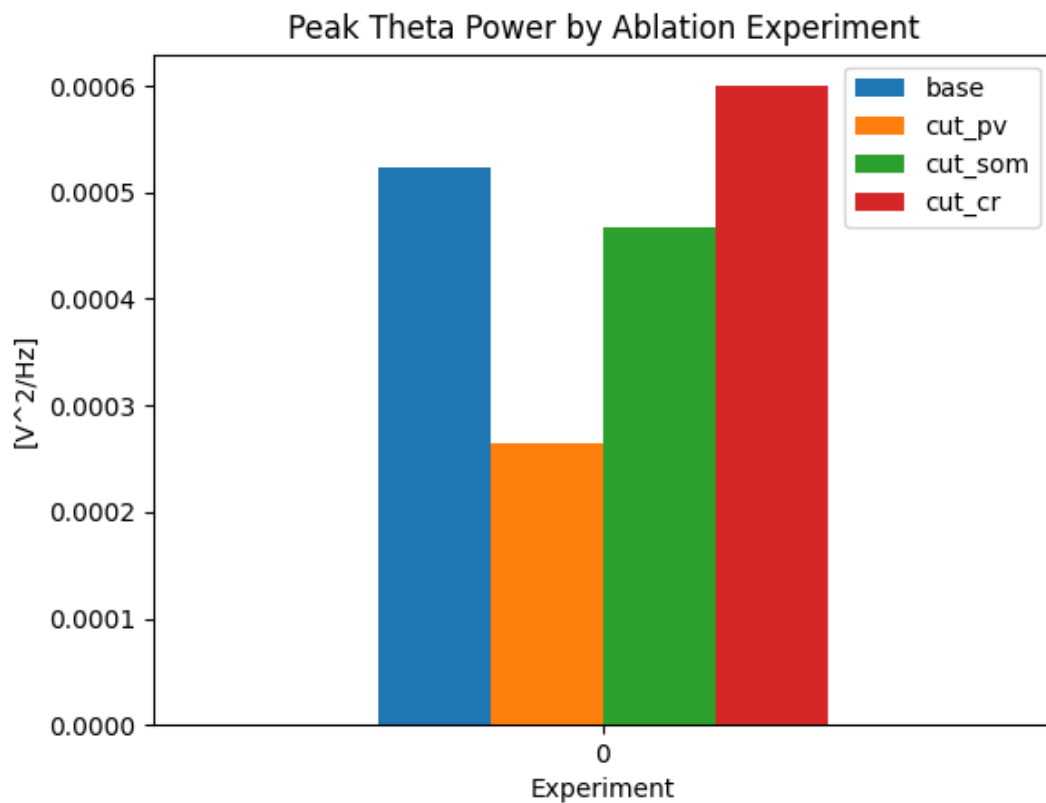
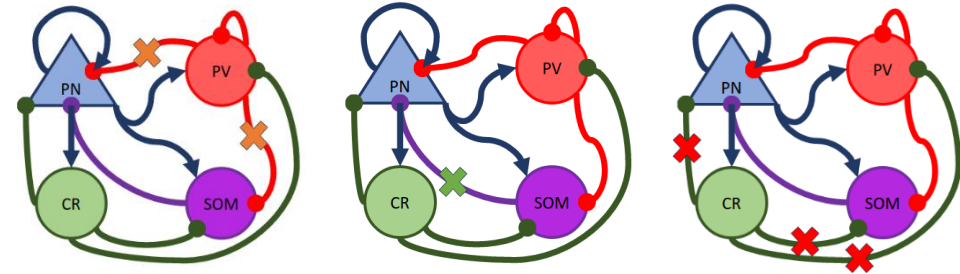


Figure 8 Ablation experiments, removing cell types sequentially to check their contributions to peak theta power in case 3 (VP/SI ACh high). Cases A-D: peak theta power at baseline (blue), and inactivation of PV (orange), SOM (green) and CR+ (red) cells, respectively.

Discussion

We show that there are at least two different subpopulations of non-cholinergic projection neurons in the VP/SI targeting different amygdaloid complex subregions. PV+ putative GABAergic and CB+ putative GABAergic or glutamatergic projection neurons did not co-express ChAT, but they made up approximately 25% of BL-targeting SI neurons and 14% of BL-targeting SI neurons. Moreover, we observed that the BL-targeting basal forebrain neurons in several subnuclei were less frequent compared to original reports of up to 3:1 (Carlsen et al. 1985). Specifically, in VP and SI, we observed that approximately 45-48% of BL-targeting neurons are ChAT+, suggesting an approximate 1:1 ratio of cholinergic to non-cholinergic projection neurons. Another study using Retrobeads (Aitta-aho et al. 2018) had also found that the cholinergic to non-cholinergic ratio among the BL-projecting nucleus basalis of Meynert neurons in mice was closer to 64:36, which amounts to less than 2:1, instead of 3:1.

The proportions of PV+ projection neurons that we report here are within the range of previous works suggesting that approximately 4-13.1% of the amygdalopetal VP neurons targeting the BL are PV+ (Mascagni and McDonald 2009). We found that, in the basal forebrain, approximately 4.1% of BL afferents from the VP and 7.5% of those from the SI arises from PV+ putative GABAergic neurons. Thus, we confirm and replicate the finding that PV+ putative GABAergic VP/SI neurons project to the amygdala, and we use this verified information to build our computational model of VP/SI-BLA innervation. On the other hand, we did not observe a single instance of PV+ projection neurons targeting the CeA or the cBNST.

We report a novel CB+ VP neuronal population projecting primarily to the BL (approximately 20% of VP projections), and to a lesser extent to the CeA. (7%). These CB+ neurons were observed to be ChAT- and thus present a putative glutamatergic or GABAergic population of projection neurons. Up to 95% of CB+ BF neurons were shown to be GAD-immunoreactive (Gritti et al. 2003) in the basal forebrain. Therefore, it is possible that only a small subpopulation of amygdala projecting CB+ neurons GABAergic, while the rest are likely to be glutamatergic akin to cortically projecting CB+ BF neurons (Gritti et al. 2003). vGluT2+ neurons were also reported to project to the amygdala (McKenna et al. 2021), but the molecular properties of these neurons are unknown. Nevertheless, we show that putative GABAergic PV+ or glutamatergic CB+ neurons constitute a significant portion of the non-cholinergic VP-amygdala projections.

Unlike the CB+ VP projection neurons selectively targeting the BL and to a lesser extent the CeA, CB+ projection neurons in the SI were found to innervate all studied amygdaloid complex substructures uniformly. The SI projections to the LA, BL, CeA, and cBNST alike had a CB+ component ranging from 5.7% to 7.4%. These neurons constitute another novel putative glutamatergic (Gritti et al. 2003) pathway from the BF to the amygdaloid complex.

No SATB1 immunoreactivity was observed among the long-range projection neurons targeting the cBNST. This suggests one of two options: that either the predominantly non-cholinergic SATB1+ neurons in the BF, specifically located in the hDB (Huang et al. 2011), are local interneurons, or that SATB1 positive neurons do not project to the BNST. These two possibilities should be rigorously tested before any conclusions can be drawn.

Amygdala Network Model

Despite the documented rich diversity of cholinergic, GABAergic, and glutamatergic BF innervation of the amygdaloid complex we have presented here, and others have presented in previous studies (Carlsen et al. 1985; Mascagni and McDonald 2009; McDonald et al. 2011; Agostinelli et al. 2019; McKenna et al. 2021), the functions of the non-cholinergic BF innervation of the amygdala are currently unknown. We set out to test the role of the GABAergic BF-amygdala pathway and its interaction with the cholinergic portion of this innervation on the functioning of the BLA local circuitry by building a biophysically realistic amygdala network model.

Based on our tract-tracing studies, the GABAergic afferents from VP/SI preferentially contact the PV cells (Fig. 4). Our computational model predicts that this biased connectivity causes the PV cells to entrain to the theta rhythm of the afferents (Fig. 6B). The PV cells, in turn, entrain the PNs to the rhythm by providing them with windows of opportunity to fire. Since the excitatory afferents to the PV cells come largely from the PNs, and the PN-PV interactions modulate this rhythm, the resulting LFP reflects broad-band theta (Fig. 6A).

At the microcircuit level, the broad-band theta rhythm arises from a combination of factors that form predictions from the model. One is the need for a weaker PN-PV synapse (see methods) so the PING mechanism of gamma generation (Feng et al., eNeuro, 2019) does not overwhelm the entrained theta rhythm. Another is the potential theta-gamma coupling due to PV cells inhibiting the SOM and CR+ cells.

Fig. 6 shows the phase preferences of firing for the various cell groups. The VP/SI afferent has a narrow-band theta frequency of 8 Hz with jitter (ISI of 125 ± 25 ms) and so does not have a phase preference in the broad-band LFP theta (Fig. 6B, bottom left). This is because the PN-PV interactions modulated LFP theta, as described earlier. In contrast, all the amygdala cell types entrained to LFP theta in specific ways. The PNs fired at the trough of the inhibition, and the PVs followed with a 4.5 ms lag and SOMs with a 6 ms lag (Fig. 7). This suggests that the PING mechanism may be involved in the generation and modulation of frequency via feedback loops involving these two cell types. The CR+ population inhibits both the PV and SOM populations providing a hierarchical level of modulation, possibly via other afferents to the CR+ population.

The phase preference of different cell types in a network model of the hippocampus has been shown to be dependent on the afferents (Mysin et al. (2019)). In particular, they mention that theta will be present even without the other afferents, and that any single afferent from possibly many unknown ones, could disturb the relative phase relationships. The phase preferences we predict in the amygdala network model (Fig. 6) assumes the afferents to be limited to those from the thalamocortical and VP/SI regions. This suggests that the computational model could serve as a test-bed to investigate potentially unknown afferents during a particular brain state if experimental data related to the phase preferences of the amygdala cells are known, as in the hippocampus.

Conclusions

- GABAergic projections originating from the basal forebrain targeting subcortical structures required for different types of memory processes possess similar anatomical features. BF cholinergic innervation of the amygdala have been studied extensively both in terms of its anatomical specifications and its physiological and behavioral functions (Woolf and Butcher 1982; Carlsen et al. 1985; Muller et al. 2011; Unal et al. 2015a; Gielow and Zaborszky 2017; Lee and Kim 2019; Kellis et al. 2020; Crimmins et al. 2022; Bratsch-Prince et al. 2023), and an increase in cholinergic tone in the BLA was recently shown to be associated with increased BLA theta activity (Bratsch-Prince et al. 2023). However, the non-cholinergic (putative GABAergic and glutamatergic) projections of the VPSI to the amygdaloid complex may be numerically underestimated and functionally underemphasized and may have overarching roles in regulating amygdalar functions. Here we assessed one such oscillatory function *in silico*.
- The GABAergic septohippocampal projection leads and modulates theta and supra-theta oscillations in the hippocampus (Hangya et al. 2009; Király et al. 2023). Here, we show in a biophysically realistic network model that structure may guide function in the larger basal forebrain GABAergic projection system: GABAergic VPSI projections to the amygdala may serve a similar purpose of leading the amygdala theta oscillations, which are implicated as causal actors in fear learning and memory (Seidenbecher et al. 2003; Lesting et al. 2011; Stujenske et al. 2014; Davis et al. 2017).

- Our results also present a novel theoretical basis for observations documenting the role of VP/SI GABAergic mechanisms in depression-related behaviors (Skirzewski et al. 2011; Akmese et al. 2023), aversion (Stephenson-Jones 2019; Stephenson-Jones et al. 2020; Farrell et al. 2021), and emotional memories (Skirzewski et al. 2011; Akmese et al. 2023). VP/SI GABAergic manipulations may influence these processes, at least partly, through their innervation of the amygdala and their effects on local amygdala dynamics.
- The results of our amygdala network model point to several hypotheses that should be tested *in vivo*:
 - The BF GABAergic projection system may carry out a single, common function in all the limbic areas that they target, contributing to local network oscillations and the associated memory processes.
 - VP/SI GABAergic and cholinergic innervation of the amygdala may be critical for amygdala oscillations (including theta and theta-modulated gamma rhythms, which were shown to be crucial for amygdala-dependent emotional learning and memory processes)
 - Based on the unit coherence changes and neuronal group ablation results (showing critical involvement of subpopulation of amygdala neurons -say X and Y- in terms of theta:
 - Normal functioning of amygdala neuronal subpopulations X and Y may be required for theta-rhythmic oscillations produced by the presence of theta-modulated VP/SI inputs in the amygdala, and the

groups X and Y may be required in turn for amygdala-dependent memory formation and Pavlovian association processes.

- Similarly, deficits in either the VP/SI GABAergic projections to the amygdala, or functional alterations in amygdala neuronal groups X and Y may possibly underlie amygdala-related problems in fear learning or fear extinction.

Tables

Table I Primary antibodies

Molecule	Host species	Dilution	Source, catalogue #	Immunogen
CB	Mouse	1:1000	Swant, 300	Purified calbindin
CB	Rabbit	1:1000	Swant, CB38	Recombinant rat calbindin D-28k
ChAT	Goat	1:500	Chemicon (Merck), ab144p	Human placental ChAT
Leu-enkephalin	Rabbit	1:1000	Abcam, ab22619	Synthetic peptide corresponding to Leu-enkephalin conjugated to keyhole limpet haemocyanin
PV	Rabbit	1:2000	Abcam, ab11427	Purified parvalbumin
PV	Rabbit	1:5000	Swant, PV27	Purified parvalbumin
SATB1	Goat	1:1000	Santa Cruz, sc-5989	N-terminus of human SATB1

Table II Synaptic connectivity in the network

	Overall connectivity	Unidirectional	Bidirectional
PN to PN	2%	1.96%	0.04%
PN to PV	26.82%	11.24%	15.58%
PN to SOM	31.19%	29.17%	2.01%
PN to CR	18.43%	16.41%	2.02%
PV to PN	52%	36.42%	15.58%
PV to PV	22.92%	17.41%	5.50%
PV to SOM	9.80%	9.80%	--
SOM to PN	6.57%	4.55%	2.01%
CR to PN	11.59%	9.57%	2.02%
CR to PV	29.70%	29.70%	--
CR to SOM	75.25%	75.25%	--

Table III Passive properties and conductance parameters for model cell types

	PV+ interneuron		Type A Principal neuron			Type C Principal neuron			SOM+ interneuron			CR+ interneuron		
V-rest (mv)	-70.0		-70.4			-70.3			-70.0			-60.1		
Input resistance(MΩ)	371		127			128			290			321		
Time Const. (ms)	20		32			32			19			20		
	soma	dendrite	soma	apical	distal	soma	apical	distal	soma	dend1	dend2	soma	dend1	dend2
Cm (μF/cm ²)	1	1	2.4	2.4	2.4	2.4	2.4	2.4	1.3	1.3	1.3	1	1.3	1.3
Ra (Ωcm)	3375	150	150	150	150	150	150	150	150	150	150	150	150	150
Conductance (S/cm ²)														
gNabar	0.035	0.01	0.015	0.015	0.015	0.045	0.015	0.015	--	--	--	--	--	--
gKdrbar	0.008	0.003	0.002	0.002	0.002	0.002	0.002	0.002	0.026	0.026	0.026	0.03	0.03	0.03
gLeak	1	1	2.50E-05	4.71E-05	4.71E-05	2.50E-05	4.71E-05	4.71E-05	6.70E-05	6.70E-05	6.70E-05	6.00E-05	6.00E-05	6.00E-05
gNapbar	--	--	0.00056	0.00045	0.00056	0.000555	0.000444	0.000555	0.0011	0.0011	0.0011	0.0014	0.0014	0.0014
gHdbar	--	--	1.50E-05	1.50E-05	1.50E-05	1.50E-05	1.50E-05	1.50E-05	--	--	--	--	--	--
gCabbar	--	--	5.50E-04	5.50E-04	5.50E-04	5.50E-04	5.50E-04	5.50E-04	--	--	--	--	--	--
gMbar	--	--	0.00224	0.001792	0.00224	0.00224	0.001792	0.00224	0.0015	0.0015	0.0015	0.0015	0.0015	0.0015
gsAHPbar	--	--	0.05	--	--	0.002	--	--	--	--	--	0.0006	0.0006	0.0006
gKapbar	--	--	0.002	--	0.002	0.002	--	0.002	--	--	--	--	--	--
gNat	--	--	--	--	--	--	--	--	0.08	0.08	0.08	0.09	0.09	0.09
gCal	--	--	--	--	--	--	--	--	--	--	--	0.02	0.02	0.02

Table IV Kinetic parameters of current channels

Current	Gating Variable	α	β	x_∞	$\tau_x (\text{ms})$
I_{Na}^1	$p=3$	$\frac{-0.4(V+30)}{\exp[-(V+30)/7.2]-1}$	$\frac{0.124(V+30)}{\exp[(V+30)/7.2]-1}$	$\frac{\alpha}{\alpha+\beta}$	$\frac{0.6156}{\alpha+\beta}$
	$q=1$	$\frac{-0.03(V+45)}{\exp[-(V+45)/1.5]-1}$	$\frac{0.01(V+45)}{\exp[(V+45)/1.5]-1}$	$\frac{1}{\exp[(V+50)/4]+1}$	$\frac{0.6156}{\alpha+\beta}$
I_{Kdr}^1	$p=1$	$\exp[-0.1144(V+15)]$	$\exp[-0.0801(V+15)]$	$\frac{1}{\exp[(-V-15)/11]+1}$	$\frac{50 * \beta}{1 + \alpha}$
I_H^2	$q=1$	$\exp[0.0832(V+75)]$	$\exp[0.0333(V+75)]$	$\frac{1}{\exp[(V+81)/8]+1}$	$\frac{\beta}{0.0081(1+\alpha)}$
I_{KM}^3	$p=2$	$\frac{0.016}{\exp[-(V+52.7)/23]}$	$\frac{0.016}{\exp[(V+52.7)/18.8]}$	$\frac{1}{\exp[(-V-52.7)/10.3]+1}$	$\frac{1}{\alpha+\beta}$
I_{Ca}^3	$p=2$	—	—	$\frac{1}{\exp[(-V-30)/11]+1}$	$\frac{2.5}{\exp\left[\frac{-(V+37.1)}{32.3}\right] + \exp\left[\frac{(V+37.1)}{32.3}\right]}$
	$q=1$	—	—	$\frac{1}{\exp[(V+12.6)/18.9]+1}$	420
I_{Nap}^4	$p=1$	—	—	$\frac{1}{\exp[(-V-48)/5]+1}$	$2.5 + 14 * \exp[- V+40 /10]$
I_{sAHP}^3	$p=1$	$\frac{0.0048}{\exp[-5 \log_{10}([Ca]_{i2}) - 17]}$	$\frac{0.012}{\exp[2 \log_{10}([Ca]_{i2}) + 20]}$	$\frac{\alpha}{\alpha+\beta}$	48
$I_{Na1.2}^5$	$p=3$	$\frac{-0.182(V+30)}{\exp[-(V+30)/7]-1}$	$\frac{0.124(V+30)}{\exp[(V+30)/7]-1}$	$\frac{\alpha}{\alpha+\beta}$	$\frac{1}{\alpha+\beta}$
	$q=1$	$\frac{-0.024(V+50)}{\exp[-(V+50)/5]-1}$	$\frac{0.0091(V+75)}{\exp[(V+75)/5]-1}$	$\frac{1}{\exp[(V+72)/6.2]+1}$	$\frac{1}{\alpha+\beta}$
$I_{Na1.6}^5$	$p=3$	$\frac{-0.182(V+43)}{\exp[-(V+30)/6]-1}$	$\frac{0.124(V+43)}{\exp[(V+30)/6]-1}$	$\frac{\alpha}{\alpha+\beta}$	$\frac{1}{\alpha+\beta}$
	$q=1$	$\frac{-0.024(V+50)}{\exp[-(V+50)/5]-1}$	$\frac{0.0091(V+75)}{\exp[(V+75)/5]-1}$	$\frac{1}{\exp[(V+72)/6.2]+1}$	$\frac{1}{\alpha+\beta}$
I_{NaT}^6	$p=3$	$\frac{Ra(V+15)}{1 - \exp[-(V+15)/7.2]}$	$\frac{Rb(-V-15)}{1 - \exp[-(-V-15)/7.2]}$	$\frac{\alpha}{\alpha+\beta}$	$\frac{1}{\alpha+\beta}$
	$q=1$	$\frac{Rd(V+30)}{1 - \exp[-(V+30)/1.5]}$	$\frac{Rg(-V-30)}{1 - \exp[-(-V-30)/1.5]}$	$1 + \frac{1}{\exp[(V+35)/4]}$	$\frac{1}{\alpha+\beta}$
I_{CaL}^6	$p=2$	$\frac{15.69(-V+81.5)}{\exp[-(V+81.5)/10]-1}$	$0.29 * \exp[-\frac{V}{10.86}]$	$\frac{\alpha}{\alpha+\beta}$	$\frac{1}{\alpha+\beta}$

Table V Number and proportion of retrogradely labeled PV+, CB+ and ChAT+ neurons

Target	Locatio n	Cells tested for PV			Cells tested for CB			Cells tested for ChAT		
		N	PV +	(%)	N	CB +	(%)	N	ChAT+ %	(%)
LA	VP	97	5	5.2	65	0	0.0	61	18	29.5
	SI	31	0	0.0	73	5	6.8	24	7	29.2
	hDB	89	0	0.0	80	1	1.3	61	8	13.1
BL	VP	49	2	4.1	47	10	21.3	42	20	47.6
	SI	40	3	7.5	46	3	6.5	29	13	44.8
	hDB	18	0	0.0	26	0	0.0	16	7	43.8
CeA	VP	118	0	0.0	90	7	7.8	59	9	15.3
	SI	304	0	0.0	270	20	7.4	70	11	15.7
	hDB	65	1	1.5	68	3	4.4	24	5	20.8
cBNST	VP	16	0	0.0	6	0	0.0	16	2	12.5
	SI	127	0	0.0	157	9	5.7	22	4	18.2
	hDB	108	0	0.0	145	1	0.7	65	13	20.0
Total		1062	14	1.3	1073	59	5.5	489	117	23.9

References

- Agostinelli LJ, Geerling JC, Scammell TE (2019) Basal forebrain subcortical projections. *Brain Struct Funct* 224:1097–1117. <https://doi.org/10.1007/s00429-018-01820-6>
- Aitta-aho T, Hay YA, Phillips BU, et al (2018) Basal Forebrain and Brainstem Cholinergic Neurons Differentially Impact Amygdala Circuits and Learning-Related Behavior. *Current Biology* 28:2557-2569.e4. <https://doi.org/10.1016/j.cub.2018.06.064>
- Akmese C, Sevinc C, Halim S, Unal G (2023) Differential role of GABAergic and cholinergic ventral pallidal neurons in behavioral despair, conditioned fear memory and active coping. *Prog Neuropsychopharmacol Biol Psychiatry* 125:110760. <https://doi.org/https://doi.org/10.1016/j.pnpbp.2023.110760>
- Alturki A, Feng F, Nair A, et al (2016) Distinct current modules shape cellular dynamics in model neurons. *Neuroscience* 334:309–331. <https://doi.org/10.1016/J.NEUROSCIENCE.2016.08.016>
- Amir A, Headley DB, Lee SC, et al (2018) VIGILANCE-ASSOCIATED GAMMA OSCILLATIONS COORDINATE THE ENSEMBLE ACTIVITY OF BASOLATERAL AMYGDALA NEURONS. *Neuron* 97:656. <Https://doi.org/10.1016/J.NEURON.2017.12.035>
- Bratsch-Prince JX, I JWWII, Jones GC, et al (2023) Acetylcholine engages distinct amygdala microcircuits to gate internal theta rhythm. *bioRxiv* 2023.02.26.530135. <https://doi.org/10.1101/2023.02.26.530135>
- Buzsáki G (2002) Theta Oscillations in the Hippocampus. *Neuron* 33:325–340. [https://doi.org/10.1016/S0896-6273\(02\)00586-X](https://doi.org/10.1016/S0896-6273(02)00586-X)
- Carlsen J, Záborszky L, Heimer L (1985) Cholinergic projections from the basal forebrain to the basolateral amygdaloid complex: A combined retrograde fluorescent and immunohistochemical study. *Journal of Comparative Neurology* 234:155–167. <https://doi.org/https://doi.org/10.1002/cne.902340203>
- Carnevale NT, Hines ML (2006) The NEURON book. The NEURON Book 1–457. <https://doi.org/10.1017/CBO9780511541612>
- Cauli B, Zhou X, Tricoire L, et al (2014) Revisiting enigmatic cortical calretinin-expressing interneurons . *Frontiers in Neuroanatomy* 8:52
- Crimmins BE, Lingawi NW, Chieng BC, et al (2022) Basal forebrain cholinergic signaling in the basolateral amygdala promotes strength and durability of fear memories. *Neuropsychopharmacology* 2022 1–10. <https://doi.org/10.1038/s41386-022-01427-w>
- Davis P, Zaki Y, Maguire J, Reijmers LG (2017) Cellular and oscillatory substrates of fear extinction learning. *Nat Neurosci* 20:1624–1633. <https://doi.org/10.1038/nn.4651>
- Destexhe A, Mainen ZF, Sejnowski TJ (1994) An Efficient Method for Computing Synaptic Conductances Based on a Kinetic Model of Receptor Binding. *Neural Comput* 6:14–18. <https://doi.org/10.1162/NECO.1994.6.1.14>

- Durstewitz D, Seamans JK, Sejnowski TJ (2000) Dopamine-mediated stabilization of delay-period activity in a network model of prefrontal cortex. *J Neurophysiol* 83:1733–1750. <https://doi.org/10.1152/JN.2000.83.3.1733>
- Einevoll GT, Kayser C, Logothetis NK, Panzeri S (2013) Modelling and analysis of local field potentials for studying the function of cortical circuits. *Nature Reviews Neuroscience* 2013 14:11 14:770–785. <https://doi.org/10.1038/nrn3599>
- Fanselow EE, Richardson KA, Connors BW (2008) Selective, state-dependent activation of somatostatin-expressing inhibitory interneurons in mouse neocortex. *J Neurophysiol* 100:2640–2652. <https://doi.org/10.1152/jn.90691.2008>
- Farrell MR, Esteban JSD, Faget L, et al (2021) Ventral Pallidum GABA Neurons Mediate Motivation Underlying Risky Choice. *The Journal of Neuroscience* 41:4500. <https://doi.org/10.1523/JNEUROSCI.2039-20.2021>
- Feng F, Headley DB, Amir A, et al (2019) Gamma Oscillations in the Basolateral Amygdala: Biophysical Mechanisms and Computational Consequences. *eNeuro* 6: . <https://doi.org/10.1523/ENEURO.0388-18.2018>
- Feng F, Samarth P, Paré D, Nair SS (2016) MECHANISMS UNDERLYING THE FORMATION OF THE AMYGDALAR FEAR MEMORY TRACE: A COMPUTATIONAL PERSPECTIVE. *Neuroscience* 322:370. <https://doi.org/10.1016/J.NEUROSCIENCE.2016.02.059>
- Fink CG, Gliske S, Catoni N, Stacey WC (2015) Network Mechanisms Generating Abnormal and Normal Hippocampal High-Frequency Oscillations: A Computational Analysis. *eNeuro* 2:ENEURO.0024-15.2015. <https://doi.org/10.1523/ENEURO.0024-15.2015>
- Freund TF, Antal M (1988) GABA-containing neurons in the septum control inhibitory interneurons in the hippocampus. *Nature* 336:170–173. <https://doi.org/10.1038/336170a0>
- Frotscher M, Léránth C (1985) Cholinergic innervation of the rat hippocampus as revealed by choline acetyltransferase immunocytochemistry: A combined light and electron microscopic study. *Journal of Comparative Neurology* 239:237–246. <https://doi.org/https://doi.org/10.1002/cne.902390210>
- Fu J-Y, Yu X-D, Zhu Y, et al (2020) Whole-Brain Map of Long-Range Monosynaptic Inputs to Different Cell Types in the Amygdala of the Mouse. *Neurosci Bull* 36:1381–1394. <https://doi.org/10.1007/s12264-020-00545-z>
- Galarreta M, Hestrin S (1997) Properties of GABAA Receptors Underlying Inhibitory Synaptic Currents in Neocortical Pyramidal Neurons. *The Journal of Neuroscience* 17:7220. <https://doi.org/10.1523/JNEUROSCI.17-19-07220.1997>
- Gielow MR, Zaborszky L (2017) The Input-Output Relationship of the Cholinergic Basal Forebrain. *Cell Rep* 18:1817–1830. <https://doi.org/https://doi.org/10.1016/j.celrep.2017.01.060>
- Gold C, Henze DA, Koch C, Buzsáki G (2006) On the origin of the extracellular action potential waveform: A modeling study. *J Neurophysiol* 95:3113–3128. <https://doi.org/10.1152/JN.00979.2005>

- Goto T, Hatanaka R, Ogawa T, et al (2010) An evaluation of the conductivity profile in the somatosensory barrel cortex of wistar rats. *J Neurophysiol* 104:3388–3412. https://doi.org/10.1152/JN.00122.2010/SUPPL_FILE/VIDEO1.WMV
- Gritti I, Manns ID, Mainville L, Jones BE (2003) Parvalbumin, calbindin, or calretinin in cortically projecting and GABAergic, cholinergic, or glutamatergic basal forebrain neurons of the rat. *J Comp Neurol* 458:11–31. <https://doi.org/10.1002/cne.10505>
- Hangya B, Borhegyi Z, Szilágyi N, et al (2009) GABAergic Neurons of the Medial Septum Lead the Hippocampal Network during Theta Activity. *The Journal of Neuroscience* 29:8094. <https://doi.org/10.1523/JNEUROSCI.5665-08.2009>
- Hu W, Tian C, Li T, et al (2009) Distinct contributions of Nav1.6 and Nav1.2 in action potential initiation and backpropagation. *Nature Neuroscience* 2009 12:8 12:996–1002. <https://doi.org/10.1038/nn.2359>
- Huang Y, Zhang L, Song NN, et al (2011) Distribution of Satb1 in the central nervous system of adult mice. *Neurosci Res* 71:12–21. <https://doi.org/10.1016/J.NEURES.2011.05.015>
- Hummos A, Franklin CC, Nair SS (2014) Intrinsic mechanisms stabilize encoding and retrieval circuits differentially in a hippocampal network model. *Hippocampus* 24:1430–1448. <https://doi.org/10.1002/HIPO.22324>
- Hummos A, Nair SS (2017) An integrative model of the intrinsic hippocampal theta rhythm. *PLoS One* 12:e0182648. <https://doi.org/10.1371/JOURNAL.PONE.0182648>
- Kellis DM, Kaigler KF, Witherspoon E, et al (2020) Cholinergic neurotransmission in the basolateral amygdala during cued fear extinction. *Neurobiol Stress* 13:100279. <https://doi.org/https://doi.org/10.1016/j.ynstr.2020.100279>
- Kim D, Pare D, Nair SS (2013) Mechanisms contributing to the induction and storage of Pavlovian fear memories in the lateral amygdala. *Learning & Memory* 20:421. <https://doi.org/10.1101/LM.030262.113>
- Király B, Domonkos A, Jelitai M, et al (2023) The medial septum controls hippocampal supra-theta oscillations. *Nat Commun* 14:6159. <https://doi.org/10.1038/s41467-023-41746-0>
- Lee S, Kim J-H (2019) Basal Forebrain Cholinergic-induced Activation of Cholecystokinin Inhibitory Neurons in the Basolateral Amygdala. *Exp Neurobiol* 28:320–328. <https://doi.org/10.5607/en.2019.28.3.320>
- Lesting J, Narayanan RT, Kluge C, et al (2011) Patterns of Coupled Theta Activity in Amygdala-Hippocampal-Prefrontal Cortical Circuits during Fear Extinction. *PLoS One* 6:e21714-.
- Li G, Nair SS, Quirk GJ (2009) A Biologically Realistic Network Model of Acquisition and Extinction of Conditioned Fear Associations in Lateral Amygdala Neurons. *J Neurophysiol* 101:1629. <https://doi.org/10.1152/JN.90765.2008>

- Lindén H, Hagen E, Łeski S, et al (2014) LFPy: A tool for biophysical simulation of extracellular potentials generated by detailed model neurons. *Front Neuroinform* 7:41. <https://doi.org/10.3389/FNINF.2013.00041/XML/NLM>
- Mahanty NK, Sah P (1998) Calcium-permeable AMPA receptors mediate long-term potentiation in interneurons in the amygdala. *Nature* 394:683–687. <https://doi.org/10.1038/29312>
- Mascagni F, McDonald AJ (2009) Parvalbumin-immunoreactive neurons and GABAergic neurons of the basal forebrain project to the rat basolateral amygdala. *Neuroscience* 160:805. <https://doi.org/10.1016/J.NEUROSCIENCE.2009.02.077>
- McDonald AJ, Muller JF, Mascagni F (2011) Postsynaptic targets of GABAergic basal forebrain projections to the basolateral amygdala. *Neuroscience* 183:144–159. <https://doi.org/10.1016/j.neuroscience.2011.03.027>
- McKenna JT, Yang C, Bellio T, et al (2021) Characterization of basal forebrain glutamate neurons suggests a role in control of arousal and avoidance behavior. *Brain Struct Funct* 226:1755–1778. <https://doi.org/10.1007/s00429-021-02288-7>
- McNaughton N, Ruan M, Woodnorth MA (2006) Restoring theta-like rhythmicity in rats restores initial learning in the Morris water maze. *Hippocampus* 16:1102–1110. <https://doi.org/10.1002/hipo.20235>
- Mesulam MM, Mufson EJ, Wainer BH, Levey AI (1983) Central cholinergic pathways in the rat: An overview based on an alternative nomenclature (Ch1–Ch6). *Neuroscience* 10:1185–1201. [https://doi.org/10.1016/0306-4522\(83\)90108-2](https://doi.org/10.1016/0306-4522(83)90108-2)
- Minneci F, Janahmadi M, Migliore M, et al (2007) Signaling properties of stratum oriens interneurons in the hippocampus of transgenic mice expressing EGFP in a subset of somatostatin-containing cells. *Hippocampus* 17:538–553. <https://doi.org/10.1002/hipo.20291>
- Mongia S, Tripathi A, Mengual E (2016) Arborization patterns of amygdalopetal axons from the rat ventral pallidum. *Brain Struct Funct* 221:4549–4573. <https://doi.org/10.1007/s00429-016-1184-2>
- Muller JF, Mascagni F, McDonald AJ (2011) Cholinergic Innervation of Pyramidal Cells and Parvalbumin-Immunoreactive Interneurons in the Rat Basolateral Amygdala. *J Comp Neurol* 519:790. <https://doi.org/10.1002/CNE.22550>
- Pang KCH, Nocera R, Secor AJ, Yoder RM (2001) GABAergic septohippocampal neurons are not necessary for spatial memory. *Hippocampus* 11:814–827. <https://doi.org/10.1002/HIPO.1097>
- Pape HC, Paré D, Driesang RB (1998) Two types of intrinsic oscillations in neurons of the lateral and basolateral nuclei of the amygdala. *J Neurophysiol* 79:205–216. <https://doi.org/10.1152/JN.1998.79.1.205/ASSET/IMAGES/LARGE/JNP.DE51F7B.jpeg>
- Parasuram H, Nair B, D'Angelo E, et al (2016) Computational Modeling of Single Neuron Extracellular Electric Potentials and Network Local Field Potentials

- using LFPsim. *Front Comput Neurosci* 10:65.
<https://doi.org/10.3389/FNCOM.2016.00065>
- Paxinos G, Watson C (2007) The rat brain in stereotaxic coordinates
- Porter JT, Cauli B, Staiger JF, et al (1998) Properties of bipolar VIPergic interneurons and their excitation by pyramidal neurons in the rat neocortex. *European Journal of Neuroscience* 10:3617–3628. <https://doi.org/10.1046/j.1460-9568.1998.00367.x>
- Power JM, Bocklisch C, Curby P, Sah P (2011) Location and Function of the Slow Afterhyperpolarization Channels in the Basolateral Amygdala. *Journal of Neuroscience* 31:526–537. <https://doi.org/10.1523/JNEUROSCI.1045-10.2011>
- Riedemann T (2019) Diversity and function of somatostatin-expressing interneurons in the cerebral cortex. *Int J Mol Sci* 20
- Roland JJ, Savage LM (2009) The Role of Cholinergic and GABAergic Medial Septal/Diagonal Band Cell Populations in the Emergence of Diencephalic amnesia. *Neuroscience* 160:32.
<https://doi.org/10.1016/J.NEUROSCIENCE.2009.02.044>
- Roland JJ, Stewart AL, Janke KL, et al (2014) Medial Septum-Diagonal Band of Broca (MSDB) GABAergic Regulation of Hippocampal Acetylcholine Efflux Is Dependent on Cognitive Demands. *The Journal of Neuroscience* 34:506.
<https://doi.org/10.1523/JNEUROSCI.2352-13.2014>
- Sah P, Westbrook RF (2008) The circuit of fear. *Nature* 454:589–590.
<https://doi.org/10.1038/454589a>
- Schindelin J, Arganda-Carreras I, Frise E, et al (2012) Fiji: an open-source platform for biological-image analysis. *Nat Methods* 9:676–682.
<https://doi.org/10.1038/nmeth.2019>
- Schomburg EW, Anastassiou CA, Buzsáki G, Koch C (2012) The Spiking Component of Oscillatory Extracellular Potentials in the Rat Hippocampus. *The Journal of Neuroscience* 32:11798. <https://doi.org/10.1523/JNEUROSCI.0656-12.2012>
- Seidenbecher T, Laxmi TR, Stork O, Pape H-C (2003) Amygdalar and Hippocampal Theta Rhythm Synchronization During Fear Memory Retrieval. *Science* (1979) 301:846–850. <https://doi.org/10.1126/science.1085818>
- Shin LM, Liberzon I (2010) The neurocircuitry of fear, stress, and anxiety disorders. *Neuropsychopharmacology* 35:169–191. <https://doi.org/10.1038/npp.2009.83>
- Silberberg G, Markram H (2007) Disynaptic inhibition between neocortical pyramidal cells mediated by Martinotti cells. *Neuron* 53:735–746.
<https://doi.org/https://doi.org/10.1016/j.neuron.2007.02.012>
- Silberberg G, Wu C, Markram H (2004) Synaptic dynamics control the timing of neuronal excitation in the activated neocortical microcircuit. *J Physiol* 556:19–27. <https://doi.org/10.1113/jphysiol.2004.060962>

- Skirzewski M, López W, Mosquera E, et al (2011) Enhanced GABAergic tone in the ventral pallidum: memory of unpleasant experiences? *Neuroscience* 196:131–146. [https://doi.org/https://doi.org/10.1016/j.neuroscience.2011.08.058](https://doi.org/10.1016/j.neuroscience.2011.08.058)
- Stephenson-Jones M (2019) Pallidal circuits for aversive motivation and learning. *Curr Opin Behav Sci* 26:82–89. <https://doi.org/https://doi.org/10.1016/j.cobeha.2018.09.015>
- Stephenson-Jones M, Bravo-Rivera C, Ahrens S, et al (2020) Opposing Contributions of GABAergic and Glutamatergic Ventral Pallidal Neurons to Motivational Behaviors. *Neuron* 105:921–933.e5. <https://doi.org/10.1016/j.neuron.2019.12.006>
- Stujenske JM, Likhtik E, Topiwala MA, Gordon JA (2014) Fear and Safety Engage Competing Patterns of Theta-Gamma Coupling in the Basolateral Amygdala. *Neuron* 83:919–933. <https://doi.org/10.1016/j.neuron.2014.07.026>
- Thomson AM, Deuchars J (1997) Synaptic interactions in neocortical local circuits: dual intracellular recordings in vitro. *Cerebral Cortex* 7:510–522. <https://doi.org/10.1093/cercor/7.6.510>
- Tóth K, Freund TF, Miles R (1997) Disinhibition of rat hippocampal pyramidal cells by GABAergic afferents from the septum. *J Physiol* 500 (Pt 2):463–474. <https://doi.org/10.1113/jphysiol.1997.sp022033>
- Unal CT, Pare D, Zaborszky L (2015a) Impact of basal forebrain cholinergic inputs on basolateral amygdala neurons. *The Journal of Neuroscience* 35:853. <https://doi.org/10.1523/JNEUROSCI.2706-14.2015>
- Unal G, Crump MG, Viney TJ, et al (2018) Spatio-temporal specialization of GABAergic septo-hippocampal neurons for rhythmic network activity. *Brain Struct Funct* 223:2409–2432. <https://doi.org/10.1007/s00429-018-1626-0>
- Unal G, Joshi A, Viney TJ, et al (2015b) Synaptic targets of medial septal projections in the hippocampus and extrahippocampal cortices of the mouse. *Journal of Neuroscience* 35:15812–15826. <https://doi.org/10.1523/JNEUROSCI.2639-15.2015>
- Vega-Flores G, Rubio SE, Jurado-Parras MT, et al (2014) The GABAergic Septohippocampal Pathway Is Directly Involved in Internal Processes Related to Operant Reward Learning. *Cerebral Cortex* (New York, NY) 24:2093. <https://doi.org/10.1093/CERCOR/BHT060>
- Washburn MS, Moises HC (1992) Electrophysiological and morphological properties of rat basolateral amygdaloid neurons in vitro. *J Neurosci* 12:4066–4079. <https://doi.org/10.1523/JNEUROSCI.12-10-04066.1992>
- Weisskopf MG, Bauer EP, LeDoux JE (1999) L-type voltage-gated calcium channels mediate NMDA-independent associative long-term potentiation at thalamic input synapses to the amygdala. *The Journal of Neuroscience* 19:10512 LP – 10519. <https://doi.org/10.1523/JNEUROSCI.19-23-10512.1999>
- Woodruff AR, Sah P (2007) Networks of Parvalbumin-Positive Interneurons in the Basolateral Amygdala. *The Journal of Neuroscience* 27:553. <https://doi.org/10.1523/JNEUROSCI.3686-06.2007>

- Woolf NJ, Butcher LL (1982) Cholinergic projections to the basolateral amygdala: A combined Evans Blue and acetylcholinesterase analysis. *Brain Res Bull* 8:751–763. [https://doi.org/https://doi.org/10.1016/0361-9230\(82\)90102-2](https://doi.org/10.1016/0361-9230(82)90102-2)
- Xu C, Datta S, Wu M, Alreja M (2004) Hippocampal theta rhythm is reduced by suppression of the H-current in septohippocampal GABAergic neurons. *European Journal of Neuroscience* 19:2299–2309. <https://doi.org/10.1111/J.0953-816X.2004.03316.X>
- Yoder RM, Pang KCH (2005) Involvement of GABAergic and cholinergic medial septal neurons in hippocampal theta rhythm. *Hippocampus* 15:381–392. <https://doi.org/10.1002/HIPO.20062>
- Zaborszky L, Csordas A, Mosca K, et al (2015) Neurons in the basal forebrain project to the cortex in a complex topographic organization that reflects corticocortical connectivity patterns: an experimental study based on retrograde tracing and 3D reconstruction. *Cereb Cortex* 25:118–137. <https://doi.org/10.1093/cercor/bht210>
- Zaborszky L, Pang K, Somogyi J, et al (1999) The Basal Forebrain Corticopetal System Revisited. *Ann N Y Acad Sci* 877:339–367. [https://doi.org/https://doi.org/10.1111/j.1749-6632.1999.tb09276.x](https://doi.org/10.1111/j.1749-6632.1999.tb09276.x)
- Zador A, Koch C, Brown TH (1990) Biophysical model of a Hebbian synapse. *Proc Natl Acad Sci U S A* 87:6718. <https://doi.org/10.1073/PNAS.87.17.6718>

Chapter 4 – Pipeline for Biophysical Modeling of a Large Class of Neurons

Tyler J. Banks, Vladimir Omelyusik, Satish S. Nair

In preparation for submission to a methods journal

Affiliation:

Electrical Engineering and Computer Science, University of Missouri, Columbia MO, 65211 USA

Correspondence to:

Satish S. Nair

Department of Electrical Engineering & Computer Science

University of Missouri, Columbia MO 65211

Phone: (573) 882-2964; Fax (573) 882-0397

E-Mail: nairs@missouri.edu

Abstract— Automation of the process of developing biophysical conductance-based neuronal models involves the selection of numerous interacting parameters, making the overall process computationally intensive, complex, and often intractable. A recently reported insight suggested natural grouping of currents into modules associated with specific neurocomputational properties, and incorporation of this insight is shown to make the model development more tractable. Specifically, we show how the proposed grouping of currents into modules facilitates the development of a semi-automated pipeline for the biophysical modeling of single neurons. The pipeline is intentionally designed to incorporate high-level user input to narrow the parameter space and generate higher fidelity models. We also expand the current modules reported previously to include spike frequency adaptation and bursting characteristics.

INTRODUCTION

The question of how single neurons contribute to information processing and ultimately to behavior has fascinated researchers for decades and is central to neuroscience research [1; 2]. The rich dynamic features of neurons make it challenging to unravel their contribution to such information processing. For instance, neurons with complex morphology such as cortical pyramidal neurons have been shown to be capable of performing linear and nonlinear computations in their active dendrites [3], but it is not clear how the computations in dendrites modulate the action potential at the soma, the primary output of the neuron. Enabling this dendritic computation are diverse extrinsic and intrinsic afferents that impinge on a neuron *in vivo*, via complex configurations of excitatory and inhibitory synapses together with various intrinsic conductances distributed non-uniformly along the dendritic tree. Adding to all this are natural and activity-dependent changes in neurons and circuits that include the following: properties of the current channels vary widely, e.g., four to five-fold variations in maximal conductances among similar neurons in the same subject [4], short- and long-term experience-dependent plasticity continually changes neuron/synapse properties and reorganizes micro-circuit configurations, and these properties can be dramatically altered via neuromodulation [5]. Concurrent with this evolving understanding of the *in vivo* characteristics of single neurons, computational models have continued to improve as we briefly review next.

Computational models of single neurons utilize a variety of morphologies depending on the specific application, ranging from single (1) and reduced (<10) to detailed (>1000) compartments, and to cascade and black-box models [1]. And the mathematical

descriptions of such compartmental models have utilized integrate-and-fire, resonate-and-fire, Izhikevich, and Hodgkin-Huxley formulations [6; 7]. The computational model features are then tuned to capture a subset of the neurocomputational properties of neurons relevant to the application. At the basic level, these neurocomputational properties include passive properties of resting membrane potential, input resistance and time constant, and current injection responses in the form of frequency-current (F-I) curves [6; 7]. Other properties include adaptation, bursting, and oscillatory potentials including low- and high-threshold oscillations.

In the present paper we focus on biophysical conductance-based models using the Hodgkin-Huxley formation that can incorporate neurophysiological details that may be relevant for network applications that require such details, i.e., modeling neuronal oscillations [8]. As cited, such network models typically use single cells with 1 to 5 compartments to limit both computational overheads and parametric uncertainties [9]. However, it is important that the reduced order model neuron possesses key neurocomputational properties including passive properties, current injection responses as well as possibly complex oscillatory dynamics. We had previously proposed and successfully tested the hypothesis that in a single neuron, sets of currents may be organized as modules that are responsible for implementing specific neurocomputational properties such as passive properties (resting membrane potential (RMP), time constant and input resistance), sub-threshold oscillations, and various spike waveforms that include tonic, adapting and bursting features [10]. Furthermore, the hypothesis naturally suggested an approach, termed the ‘segregation method’, that was shown to facilitate the selection of

single cell model parameters and to simplify the modeling of single cells. This makes the approach attractive to automation of the modeling of single neurons, as we suggest below.

The rich and complex properties displayed by neurons makes modeling the cellular behaviors of neurons challenging. This makes manual tuning tedious for the parameters related to the current kinetics (e.g., maximal conductances) of such neurons.

Consequently, automated strategies for modeling single cells using biological data exist for specific cell types including simplified spiking models [11] and those with numerous compartments, e.g., [12; 13], but are scarce for general neuron types even at the single compartment level (but see [14]). In the present paper, we explore an automation scheme *Automated Cell Tuner (ACT)* to design a broad range of single neuron computational models using the insight from the segregation method of organizing currents into specific modules for each dynamic features of the neuron. Specifically, the approach links distinct current modules to specific neural signatures and provides a method that utilizes insights to simplify the hand-tuning process by reducing interactions between the current modules [10].

Furthermore, we extended the biophysical-based segregation method [10] to also include another neurocomputational property of spike frequency adaptation and bursting. We illustrate the proposed scheme using an example of a pyramidal neuron in the CA3 region of the hippocampus that responds to stimuli with a rapidly adaptive burst waveform that then reduces to tonic spiking or to a continuously bursting phenotype, both of which are commonly found neural signatures [15]. We then show that such a waveform output of

CA3 neurons plays an important role in the generation of theta oscillations in the model hippocampal network. We will make the automated pipeline for modeling publicly accessible to the neuroscience community to facilitate designing single neuron models.

METHODS

Models of single neurons were developed using experimental parameters from our collaborators and the literature [10], and implemented using the NEURON 7.4 simulator [16] with a fixed time step of 25 μ s. We first describe a brief overview of the mathematical underpinnings of both single cell dynamics and of the segregation approach [10]. That is followed by the procedure used for the development and validation of the proposed pipeline for the biophysical modeling of a class of neurons.

Mathematical equations for voltage-dependent ionic currents.

The dynamics for each compartment (soma or dendrite) followed the Hodgkin-Huxley formulation [15] in eqn. 1,

$$\frac{C_m dV_s}{dt} = -g_{Leak}(V_s - E_{Leak}) - g_c(V_s - V_d) - \sum I_{cur,s}^{int} - \sum I_{cur,s}^{syn} + + I_{inj} \quad (1)$$

where V_s/V_d are the somatic/dendritic membrane potential (mV), $I_{cur,s}^{int}$ and $I_{cur,s}^{syn}$ are the intrinsic and synaptic currents in the soma, I_{inj} is the electrode current applied to the soma, C_m is the membrane capacitance, g_{Leak} is the conductance of the leak channel, and g_c is the coupling conductance between the soma and the dendrite (similar term added for other dendrites connected to the soma). The intrinsic current $I_{cur,s}^{int}$, was modeled as $I_{cur,s}^{int} = g_{cur} m^p h^q (V_s - E_{cur})$, where g_{cur} is its maximal conductance, m its activation variable (with exponent p), h its inactivation variable (with exponent q), and E_{cur} its reversal potential (a similar equation is used for the synaptic current $I_{cur,s}^{syn}$ but without m and h). The kinetic equation for each of the gating variables x (m or h) takes the form but without

m and h . The kinetic equation for each of the gating variables x (m or h) takes the form

$$\frac{dx}{dt} = \frac{x_\infty(V,[Ca^{2+}]_i) - x}{\tau_x(V,[Ca^{2+}]_i)} \quad (2)$$

where x_∞ is the steady state gating voltage- and/or Ca^{2+} - dependent gating variable and τ_x is the voltage- and/or Ca^{2+} - dependent time constant. The equation for the dendrite follows the same format with ‘ s ’ and ‘ d ’ switching positions in eqn. 1. The procedure for selecting the channel currents and their model parameters are described next using an approach we proposed recently.

Segregation hypothesis for single cell design

The segregation hypothesis, in brief, states that distinct current modules, with activation functions segregated on the voltage axis, implement different neurocomputational properties [10]. The implementation of the hypothesis for single cell modeling is illustrated in Box 1. For illustrative purposes, consider the case of a tonic spiker. The segregation of the activation and inactivation functions is shown in cartoon form in Fig. 1, using two modules: passive module (resting membrane potential V_{rest} , time constant τ_m , and input resistance R_{in}) and spiking module. In this case, leak, and the hyperpolarization-activated cation current H are responsible for passive properties, and together constitute the passive module. Similarly, transient sodium Na_t and delayed rectifier K_{dr} currents (together with the leak current) set the spiking properties as a spiking module. The activation functions are segregated to prevent overlap, i.e., the currents of each module start on the voltage axis only after the zone of action of the module to its left. Cut-off values for the gating variables are selected to be within reported ranges of $V_{1/2}$ values [6].

Development of pipeline for the Automated Cell Tuner (ACT)

The pipeline for the ACT is shown schematically in Figure 2, and outlined in steps as follows: (1) The user provides biophysical data related to the neuron. The data includes neuronal type, morphology, conductances present in the soma, axon, and dendrites, and their kinetics, passive properties (resting membrane potential V_{rest} , time constant τ , and input resistance R_{in}), current injection responses (frequency-current, F-I curve), and parameters related to other characteristics such as adaptation, bursting, and oscillatory potentials. If specifics related to any of the parameters are not known, they are retrieved from a library of cell models with parameters, developed from papers and databases. (2) Two training datasets are developed using ranges for selected neuronal parameters. In the present paper, we assume that only maximal conductances of the currents are tuned. However, the pipeline provides provision to tune the current kinetics such as half-activation voltage $V_{1/2}$ and slope k (see Fig. 1). The parameters are sampled randomly from within known ranges (e.g., see Table 2), and then passed to two simulators. One of the simulators uses the original activation/inactivation functions of the currents and accordingly, that pipeline is termed pipeline-*original*, since it ‘estimates’ optimal parameters and current injection levels of the predicted cell model. The other simulator uses the segregated activation/inactivation functions of the currents, and that pipeline is, similarly, termed pipeline-*segregated*. The simulator will then generate a training dataset for use by a machine learning model. The dataset development involves sampling the parameters over the ranges and providing them sequentially to the simulator that then generates voltage traces for specified current injection profiles. (3) This training dataset is

then used to obtain an ‘inverse’ model, i.e., to predict the neuronal parameters and current injection profile given the voltage trace, employing a machine learning (ML) model. The pipeline is designed to use any ML architecture, and here we report results from random forest, fully-connected, and CNN architectures. Once trained fully, the pipeline is designed to provide the user with a computational model of the neuron in the particular software package selected, e.g., NEURON.

The training follows the standard procedure for the pipeline termed *pipeline-original* (using unchanged activation/inactivation functions) and this pipeline estimates/predicts all the parameters of the model cell simultaneously. However, for the *pipeline-segregated* (with segregated activation/inactivation functions), the pipeline has two stages. In the first ‘coarse’ stage, the neuronal parameters are estimated sequentially for each module, starting from the left (see Fig. 1) using a larger range of search space for each parameter of that module. For instance, in the cartoon figure 1, the passive module parameters are determined analytically prior to the simulation stage, and then the spiking parameters and so on. And in a second step, the estimation process begins with the all the parameters assembled from the coarse step (e.g., passive + spiking parameters) and then tuning them together around a narrower user-defined range of values around that coarse parameter set.

Library of neuronal morphology, membrane, current channel, and synaptic properties

A collection of neuronal properties relevant to the model development are available for standard cell types from existing databases, e.g., NeuronDB [17]. Also, information about

how to retrieve them from databases is provided to the user. For this study we procured a small library such sources, kinetics outlined in Table 3.

Machine learning architectures and Input design

ACT's primary machine learning architecture was Random Forest. Random Forests are a type of ensemble learning technique that uses multiple decision trees to compute an average prediction. Due to the spectrum of conductance values possible, this was framed as a regression task. While providing a raw voltage trace as input is possible, a reduced order dataset in the form of summary statistics were computed.

At each stage of segregation, the user can specify which summary stats to use when training the pipeline. An example set would be as follows:

1. ARIMA stats (useful only for HTO and LTO)
2. Number of spikes
3. Spike times (first n, specified by the user). Zero was used in place of a spike time if one of the first n spikes did not exist.
4. Interspike interval
5. Average spike height
6. Average spike trough
7. Frequency of oscillations (HTO/LTO)
8. Amplitude of oscillations (HTO/LTO)
9. Mean voltage potential

User interaction with the pipeline.

To use the pipeline the user must specify a set of parameters in the configuration file.

This includes:

1. Model template
2. Desired passive properties
3. Simulation parameters (initial voltage, current clamp duration)
4. The set of target user traces for the model to learn

5. Amp values that the target user trace was subjected to
6. Parameters to be adjusted (conductance names, and range values that are acceptable)
7. Type of machine learning algorithm to use
8. Segregation stages

Each segregation stage is separate from one another. This provides the user the ability to tune each stage differently, and incrementally. For example, stages where cell spiking does not occur, e.g., LTO/HTO modules, it is possible to omit spike-related summary statistics and include ARIMA statistics. The opposite is true for cases where spiking occurs. In the event a segregation stage does not perform well enough, the user is able to re-run the stage given modified parameters instead of running the whole pipeline again. Parameters such as input ramps (for slowly increasing current injection), machine learning technique, number of epochs and the re-learning of prior parameters on a tighter bound can also be specified here.

Example cases to illustrate functioning of the ACT pipelines.

We consider four example case neurons to illustrate the proposed automated scheme. Two are related to the neurocomputational property of adaptation and bursting, that was not considered in our earlier paper [10]. The other two are representative neurons that exhibit four neurocomputational properties: spiking, adaptation, and a tonic spiker, as well as oscillatory potentials of low-threshold and high-threshold types, involving complex dynamics. The channels and current densities of the tonic spiker and adapting cell were from model LA neurons that were designed to match biological data (Kim et al., 2013). They had the following channels (specific values of the maximal conductance

densities (mS/cm^2) provided in parenthesis): transient sodium Na (27), persistent sodium Nap (0.142), delayed rectifier K_{dr} (1.5), A-type potassium (2), M-type potassium K_M (0.6), slow AHP potassium sAHP (type A – 0.3, type C – 0.115), calcium Ca (0.55), hyper-polarization activated cation channel H (0.015), and leak (0.055). The channel densities were the same for both types except for the sAHP current for which two values are noted in the parenthesis. The time constant for the Ca pool was 1 sec. The passive properties for both cell types was the same with $V_{\text{rest}} = -70 \text{ mV}$, input resistance $R_{\text{in}} = 141 \text{ M}\Omega$ and membrane time constant $\tau = 30.88 \text{ ms}$.

Nap-KM module for adaptation/bursting properties. To design the neurocomputational property of adaptation and bursting, we first add the transient sodium (Nap) and the M type potassium (KM) as a module (known to provide this property to neurons [6]) to the normal ‘passive’ and ‘spiking’ modules, and this is illustrated in Figure 1. An example case hippocampal CA3 neuron with an adapting characteristic [18] is considered to illustrate the procedure. The neuron also has other spiking currents transient sodium (Nat), delayed rectifier potassium (Kdr), hyperpolarization-activated cation current (H) and leak currents, which are kept fixed here. The ranges for the adjustable parameters for Nap-KM modules of the CA3 neuron, based on biological reports, were as follows (units for g is mS/cm^2 and for $V_{1/2}$ is mV): $g_{\text{Nap}} = [1 \times 10^{-5}, 0.005]$, $g_{\text{KM}} = [5 \times 10^{-6}, 0.017]$, $V_{1/2 \text{ Nap}} = [-65, -35]$, $V_{1/2 \text{ KM}} = [-50, 0]$ [6].

Alternative CaS-CaT-sAHP module for adaptation/bursting properties. A second option to implement adaptation and busting is the set of currents that include a low-threshold Ca^{2+}

(CaS), high-threshold Ca^{2+} (CaT) and the calcium-activated potassium (sAHP) currents. A different class of the same hippocampal CA3 neuron that exhibits the bursting characteristic [19] is considered for this option. Like the case above, the ranges for the parameters for this set of current were as follows (units for g is mS/cm^2 and for $V_{1/\text{s}}$ is mV): $g_{\text{CaS}} - [1*10^{-5}, 0.017]$, $g_{\text{CaT}} - [1*10^{-5}, 0.017]$, $g_{\text{sAHP}} - [1*10^{-5}, 0.008]$, $V_{1/2 \text{ CaS}} - [-33]$, $V_{1/2 \text{ CaT}} - [-27.1]$.

Two modules for low- and high-threshold (LTO and HTO) oscillatory potentials.

Example cases 3 and 4 consider The channels and current densities of the tonic spiker and adapting cell were from model LA neurons that were designed to match biological data (Kim et al., 2013). They had the following channels (specific values of the maximal conductance densities (mS/cm^2) provided in parenthesis): transient sodium Na (27), persistent sodium Nap (0.142), delayed rectifier K_{dr} (1.5), A-type potassium (2), M-type potassium K_M (0.6), slow AHP potassium sAHP (type A – 0.3, type C – 0.115), calcium Ca (0.55), hyper-polarization activated cation channel H (0.015), and leak (0.055). The channel densities were the same for both types except for the sAHP current for which two values are noted in the parenthesis. The time constant for the Ca pool was 1 sec. We found that the persistent sodium Nap and the M-type potassium and K_M formed the LTO module, and that Ca, sAHP, K_M , and K_{dr} currents formed the HTO module.

RESULTS

Using insights related to potential grouping of currents into modules to implement function [20], we developed a pipeline to develop biophysical models of a large class of neurons. Four example cases illustrate the diversity of neurons that could be modeled as well as how the user can interact with the pipeline. We then illustrate how the parameter space of the conductances narrows with the sequential tuning of each module, providing further insights into the biophysics of the neuron.

ACT pipeline to automate modeling for a large class of neurons

We developed a pipeline to automate the biophysical modeling of single neuron using the Hodgkin-Huxley formulation and tested it with various examples. In brief, the proposed pipeline has the following structure (Fig. 2): (i) The user provides the passive and current injection properties, as well as any other relevant neurocomputational property of their neuron. And can optionally provide parameters related to morphology, and biological ranges for the kinetics for the various currents; (ii) The information is used to design two pipelines to estimate model parameters, one that uses the original current kinetics (termed *-original*) and the other using the kinetics after the activation/inactivation functions have been segregated [10] to modularize the currents (termed *-segregated*). (iii) A training dataset is developed for pipeline-*original* by sampling the conductance parameter space randomly within ranges (specified by the user or obtained from biology) and passing the parameter vector to the simulator to generate voltage traces for specified current injection profiles. This process is repeated until sufficiently large training samples (candidate parameters and voltage traces) are acquired. This training dataset is used to design pipeline-*original*, by inverting the relationship as outlined in Fig. 2, using an ML

architecture. We used several architectures including random forest, fully connected networks, and a convolutional neural network (CNN) but primarily report results from random forest. (iv) The same process as in the previous case is used to design pipeline-*segregated* but in two-stages. In stage 1, the parameters are estimated module-by-module as outlined in Fig. 2 starting with coarser bounds on the parameters, and then we combine all the parameters in stage 2 to obtain better estimates using finer bounds. Note that each module uses ML architectures, including different ones as appropriate, to estimate the parameters related to the module. This is illustrated below via example cases.

Model with segregated estimator provides better match compared to that with original estimator. For the statistical modeling using ML architectures, the tuning for the *original* case followed the standard approach using the training dataset for that case. For the segregated case, we propose a procedure involving two steps. In the first coarse tuning step, we tuned the maximal conductances associated with each current module separately, starting with the passive module, and progressing to the last module (as illustrated using example cases below). This provides a starting set of parameters for the maximal conductances ('operating point') for the second fine tuning step. Also, we provide ranges for each parameter around this set of parameters, based on experience with coarse tuning. This information is used to then generate a second training dataset for all conductances simultaneously to implement fine tuning of all the parameters.

Example cases. We consider four example cases to illustrate the functioning of the proposed pipeline. The first two example cases represent burster cells that utilize different

currents to implement the bursting characteristic. In example case 1 of a hippocampal CA1 neuron, bursting is implemented by the Nap,Km module, while a different combination of currents CaS, CaT, sAHP implement bursting in a CA3 hippocampal neuron of case 2. Results of *the hippocampal CA1 simulation are shown* in Figure 3 and the Hippocampal CA3 in Figure 4. Example cases 3 and 4 are a tonic spiker (type C) and highly adaptive (type A) variants of the lateral amygdala pyramidal cells in [10]. These cell types exhibit oscillatory potentials of the low-threshold and high-threshold types reported in the literature [8; 21]. Comparison of results for the tonic spiker are shown in Figure 5, and the highly adaptive cell is shown in Figure 6. Using the passive properties provided by the user, the following cellular parameters are determined for pipeline-*segregated*: $E_{leak} = V_{rest}$; $G_{leak} = I/R_{in}$; $C = \tau/R_{in}$. The same values are also used for the pipeline-*original*, except for E_{leak} since it is a function of the activation functions in this case. In case the H current is present, the equations for the segregated case are modified to the following: G_{leak} and C using the same equations. However, E_{leak} is obtained by solving the nonlinear equation $V_{rest} + m_H(V_{rest}) = G_{leak}*E_{leak} + G_H*E_H$.

Comparison of the performance of the automated scheme in matching passive properties and F-I curve for the tonic spiker and adapting cell types with 9 conductances is shown in Table 1. Also shown is the error in conductance parameters which were available since we used known model cells as the ‘user’ data in these cases. The segregated model outperformed the original one for both cell types. For the tonic spiker cell which exhibited adaptation and had numerous conductances, with much lower errors in passive properties and in the estimation of parameter values.

Permissible conductance space for neurons. The step-by-step addition of modules and tuning the conductances permit the evaluation of the process by which the conductance space is narrowed by each of the neurocomputational properties. Considering the example case of burster-1, we have a 4-dimensional 4-D) space of maximal conductances of the N_{ap} , K_M , Na_t and K_{dr} currents. We tune all the conductances simultaneously since they are all interacting and share the same ‘zone’ of segregation, to the right of the passive module. Fig. X shows the convergence of tuning process. Next we consider the LA-A cell which has several modules, to illustrate the process module by module. In this case, we tune the LTO module, after the passive one, and then move on to the spiking/adapting module and then to the HTO module. Fig. X shows how the conductance space narrows after each module is tuned.

Two current modules enable incorporation of additional neurocomputational properties

We extended the results in our previous paper by explicitly designing the passive module for a single compartment model using the biological data, as follows: Given V_{rest} , time constant τ_m , and input resistance R_{in} , we set the reversal potential of leak current as $E_{leak} = V_{rest}$, maximal conductance of leak channel as $G_{leak} = 1/R_{in}$, and membrane capacitance $C_m = \tau_m/R_{in}$. If the H-current is present, these equations are modified as follows: We use the same procedure equations for G_{leak} and C_m , and for E_{leak} , we solve the nonlinear equation iteratively to find a solution for V_{rest} and E_{leak} simultaneously using the equation $V_{rest} + m_H(V_{rest}) = G_{leak} * E_{leak} + G_H * E_H$, where m is the activation function for the H channel, and the other terms as defined in earlier sections.

Nap-KM module. This module adds the neurocomputational property of adaptation and bursting, depending on the parameters of the two currents. Both channels can be segregated up to \sim 60 mV in this model. Optimizing the parameters after implementing the segregation (Fig. 1) resulted in the following parameter set that provided the adapting characteristic shown in Fig. 2A that matches the biological current injection (Fig. 2C) response in [6] well: $g_{Nap} = 0.0005$, $g_{KM} = 0.017$, $V_{1/2\ Nap} = -48$, $V_{1/2\ KM} = 35$.

Adaptation happens when KM current builds up enough to counteract the Nap current. The time constant of KM controls the duration of the initial high frequency of the adapting characteristic. On the other hand, increasing g_{KM} and g_{Nap} together (~ 0.17 and 0.001 , respectively) shuts off spiking and results in a bursting characteristic. Importantly, without such a segregation of the current modules, it was very difficult to hand-tune the parameters due to the interactions between the currents. Such interaction effects resulted in changes to spiking properties affecting passive properties, and so on. This makes the tuning process very difficult, for both hand- and automated-tuning scenarios [10]. This neuron becomes an endogenous spiker if segregation is not implemented (Fig. 2B).

CaS-CaT-sAHP module. This second option to add adaptation/bursting involves three currents. CaS is segregated at -64 mV; CaT and sAHP remain unsegregated (Fig. 3A). The parameter set after implementing the segregation scheme (Fig. 3A) and tuning are as follows: $g_{CaS} = 0.00425$, $g_{CaT} = 0.001$, $g_{sAHP} = 0.005$. These resulted in a bursting profile. Without segregation, the CaS-CaT-sAHP module will offset V_{rest} by around 0.3mV. Eleak can be altered to account for this change; however, altering Eleak will result

in a change in both inter-burst interval (IBI) and spikes per burst. Fixing this involves a time-consuming retuning of the cell which is less preferable compared to the alternative of segregating the CaS channel appropriately. Bursting is controlled in this module by t_{sAHP} and $t_{Ca\text{-pool}}$. t_{sAHP} can be increased or decreased largely independently to increase or decrease, respectively, the number of spikes per burst. Similarly, $t_{Ca\text{-pool}}$ can be increased or decreased almost independently to increase or decrease, respectively, the inter-best interval.

Some interesting **neural dynamic characteristics** for the Nap-KM and CaS-CaT-sAHP modules were as follows (Fig. 3B): (i) the ranges of IBI for the Nap-KM module are set by the lower/higher biological ranges for the time constant of the KM current, of 46 ms and 120 ms, respectively. The maximum spike frequency was 125 Hz. (ii) For the CaS-CaT-sAHP module, the minimum IBI was 120 ms, set by the minimum time constant for the Ca²⁺ pool to permit sAHP to activate. Ranges were not found to set the maximum on the IBI in this case. The maximum spiking frequency for this module was 77 Hz, set by the competing effects of CaS that raised the membrane potential to allow for faster spiking but also simultaneously increases activation of sAHP activation that causes inhibition.

Model complexity and run times

The approximate times to run each stage is highly dependent on the number of parameters the pipeline is trying to learn. With 6 parameters split 5 times, across 5 different amp input profiles we generate 5^*5^6 (78,125) parameter sets. Each parameter is then simulated with

neuron for a user specified period of time (1 second by default). Without MPI parallelization this simulation can take anywhere from 1 hour to 4 hours on a single core machine. With MPI (48 cores) this takes less than 5 minutes.

If ARIMA stats are generated for each trace as a summary statistic, this can take more than 24 hours on a single core machine. ACT utilizes parallel processes to generate the ARIMA stats, and on a 48-core machine this can take roughly 4 hours. Finally, when running the simulation to generate the resulting parameters, selection of the machine learning algorithm and hyperparameters plays a big role in the time it takes to run. Using Random Forest, we can generate traces in less than 5 minutes (single core). Using a torch neural network, this can take more than an hour to train the network if the machine is not GPU enabled.

DISCUSSION AND CONCLUSION

Modeling single cells with multiple neurocomputational properties poses challenges at both theoretical and application levels. For instance, at the theoretical level it is not clear how the plethora of current channels coordinate to implement the seemingly distinct neural signatures. At the application level, procedures to select parameters including automated schemes, typically result in multiple parameter sets for the same solution (e.g., [4]). Moreover, automated schemes such as genetic algorithm searches (e.g., [23]) cannot provide mechanistic insights into the interactions among the channels. We developed pipelines that permitted the user to interact and configure the pipeline using neurophysiological insights.

Automated pipeline for developing biophysical models of neurons

The segregation method with its lack of interaction among the various current modules makes the tuning process more efficient and facilitates automation via the machine learning package. Automation of the simple spiking module was shown in the Results section.

The modules are designed to be flexibly configurable so that the user can be involved in incorporating neurophysiological as well as training insights. A neurophysiological insight might be having tighter bounds on some parameters, and a training insight could lead to reconfiguring the sequence of modules. We also note that the execution times are very reasonable with end-to-end run of a pipeline taking ~ 30 minutes on average for the training part, which could possibly be further reduced with a higher degree of parallel processing.

Insights into features of modules that implement spike-frequency adaptation and bursting

The neurocomputational property of spike frequency adaptation and bursting was implemented via two known current modules, the distinct characteristics of which are highlighted by our approach. Parameters of the Nap-KM module was found to have several functional implications. Time constant t_{Nap} was found to be restricted to a small range suggesting that it might not vary much, and this time constant controls the rapid response of the burst. The initial high frequency of the burst was controlled by g_{Nap} . The time constant t_{KM} controlled the duration of the burst and its conductance g_{KM} controlled spikes per burst. In the two-current module, g_{Nap} and g_{KM} together controlled the frequency of the burst. And g_{KM} and t_{KM} together controlled the duration of the burst and the inter-burst interval. This made it difficult to independently set both burst duration and inter-burst interval with the Nap-KM module, suggesting that it may be better suited primarily for the adaptation characteristic. On the other hand, the CaS-CaT-sAHP module had additional degrees of freedom which made it possible to independently vary both burst duration and inter-burst interval. However, the Nap-KM module seems to allow for a faster burst spiking profile than the CaS-CaT-sAHP module which may mean it is necessary in cells that display this characteristic.

Also, the analysis suggests **user tuning guidelines** for the Nap-KM module as follows: increasing t_{KM} and g_{KM} increases inter-burst interval; an increase in g_{Nap} increases the spike frequency; number of spikes per burst can be increased by increasing g_{Nap} , increasing t_{KM} , or decreasing g_{KM} with the latter being the least effective. Similar

guidelines for tuning the CaS-CaT-sAHP module are as follows: increasing t_Ca2+pool and t_sAHP increase IBI; spike frequency can be increased by gCaS; spikes per burst can be increased by decreasing gCaT or gsAHP, or by increase t_sAHP.

As expected with an evolving field with dynamics and parametric features still being understood, questions have been raised whether detailed realistic modeling of single neurons is indeed realistic [24]. Such questions are also suitable for study using machine learning models. Indeed, a recent study found that up to 8 layers are required in a deep neural network to faithfully represent a morphologically complex neuron [25], illustrating the complexity in the modeling process. We tried a recently reported machine learning scheme that includes Bayesian and fully connected neural network modules (simulation-based inference, sbi; [14]) to estimate all parameters simultaneously but were unsuccessful possibly due to the large set of parameters and/or the complexity of the dynamic interactions, and existence of multiple solutions. As we have shown, incorporating neural insights into the pipeline via the segregation technique, and adopting a two-stage estimation procedure is capable of developing neuron models that exhibit diverse dynamics ranging from tonic spiking and adaptation to low- and high- threshold oscillatory potentials. The next steps are to extend the pipeline to semi-automatically design neuron models with 2-5 compartments, and then to morphologically detailed models with over 1000 compartments.

Future Work

To further improve prediction accuracy of the pipeline may be beneficial or necessary to allow for some parameters to have a higher level of resolution than others when generating

the initial training data. Currently, all parameters are split equally, regardless of importance, difference in output, or absolute conductance space. For example, the spiking dynamics are highly responsive to Na and sAHP conductance changes, a higher resolution in the conductance values for these two channels would ensure these dynamics are captured. Improvements to developer and user experience will be necessary for general adoption. This includes automated testing, detailed usage documentation, advertising, and refactoring to include additional utility scripts.

Considering more complex morphology, i.e., cells with 2-5 compartments, and morphologically realistic ones with over 1000 compartments would be another fruitful direction to pursue. Data are beginning to emerge on the morphological details, conductance distributions, and other properties of such cells that affect the function of synaptic integration.

Table titles

Table 1. Comparison of errors (%) between the original and proposed modeling schemes

Table 2. Parameter values of estimated current channel parameters for the four example cases

Table 3. Kinetics of the currents in the various example cases

Figure titles

Figure 1. Cartoon illustrating segregation of currents into three modules – passive (H), adapting/bursting (Nap, KM) and Spiking (Nat, Kdr) for the example case 1 burster neuron

Figure 2. Structure of the simulation-based inference pipeline for ACT

Figure 3. Comparisons between predicted models from the two pipelines for example case 1 (Burster-1) with 5 channels – leak, Nap, KM, Nat, Kdr

Figure 4. Comparisons between predicted models from the two pipelines for example case 2 (Burster-2) with 5 channels – Leak, CaS, CaT, sAHP, Nat, Kdr

Figure 5. Comparisons between predicted models from the two pipelines for example case 3 (tonic spiker with oscillatory potentials) – type C pyramidal neuron in the rodent lateral amygdala

Figure 6. Comparisons between predicted models from the two pipelines for example case 3 (highly adaptive cell with oscillatory potentials) – type A pyramidal neuron in the rodent lateral amygdala

REFERENCES

1. Herz AV, Gollisch T, Machens CK, Jaeger D (2006) Modeling single-neuron dynamics and computations: A balance of detail and abstraction, *Science* 314, 80-85.
2. Brunel N, Hakim V, Richardson MJE (2014) Single neuron dynamics and computation, *Curr Opin Neurobiol* 25, 149-155.
3. London M, Häusser M (2005) Dendritic computation, *Annu Rev Neurosci* 28, 503-532.
4. Prinz AA, Bucher D, Marder E (2004) Similar network activity from disparate circuit parameters, *Nat Neurosci* 7, 1345-1352.
5. Marder E (2012) Neuromodulation of neuronal circuits: Back to the future, *Neuron* 76, 1-11. PMC3482119.
6. Izhikevich (2007) Dynamical systems in neuroscience the geometry of excitability and bursting In Computational neuroscience (Cambridge, Mass., MIT Press).
7. Dayan P, Abbott LF (2005) Theoretical neuroscience: Computational and mathematical modeling of neural systems (Cambridge, MA: MIT Press).
8. Feng F, Headley DB, Amir A, Kanta V, Chen Z, Paré D, Nair SS (2019) Gamma oscillations in the basolateral amygdala: Biophysical mechanisms and computational consequences, *eNeuro* 6, ENEURO.0388-0318.2018.
9. Borgers C (2017) An introduction to modeling neuronal dynamics (Springer International Publishing).
10. Alturki A, Feng F, Nair A, Guntu V, Nair SS (2016) Distinct current modules shape cellular dynamics in model neurons, *Neuroscience* 334, 309-331. PMC5086448.
11. Pozzorini C, Mensi S, Hagens O, Naud R, Koch C, Gerstner W (2015) Automated high-throughput characterization of single neurons by means of simplified spiking models, *PLoS Comput Biol* 11, e1004275. PMC4470831.
12. Bahl A, Stemmler MB, Herz AVM, Roth A (2012) Automated optimization of a reduced layer 5 pyramidal cell model based on experimental data, *J Neurosci Methods* 210, 22-34.
13. Huys QJM, Ahrens MB, Paninski L (2006) Efficient estimation of detailed single-neuron models, *J Neurophysiol* 96, 872-890.
14. Gonçalves PJ, Lueckmann J-M, Deistler M, Nonnenmacher M, Öcal K, Bassetto G, Chintaluri C, Podlaski WF, Haddad SA, Vogels TP, Greenberg DS, Macke JH (2020) Training deep neural density estimators to identify mechanistic models of neural dynamics, *eLife* 9, e56261.
15. Byrne JH, Roberts JL, Waxham MN (2014) From molecules to networks: An introduction to cellular and molecular neuroscience, 3rd edn (Elsevier).
16. Carnevale N, Hines M (2006) The neuron book (UK: Cambridge University Press).
17. al. Me (2023) Database of three types of neuronal properties, NeuronDB <https://senselabmed.yale.edu/neurondb>.
18. Sun Q, Sotayo A, Cazzulino AS, Snyder AM, Denny CA, Siegelbaum SA (2017) Proximodistal heterogeneity of hippocampal ca3 pyramidal neuron intrinsic properties, connectivity, and reactivation during memory recall, *Neuron* 95, 656-672.e653.
19. Staff NP, Jung H-Y, Thiagarajan T, Yao M, Spruston N (2000) Resting and active properties of pyramidal neurons in subiculum and ca1 of rat hippocampus, *J Neurophysiol* 84, 2398-2408.
20. Hummos A, Franklin CC, Nair SS (2014) Intrinsic mechanisms stabilize encoding and retrieval circuits differentially in a hippocampal network model, *Hippocampus* 24, 1430-1448. PMC24978936.
21. Faber ES, Sah P (2003) Ca²⁺-activated K⁺ (BK) channel inactivation contributes to spike broadening during repetitive firing in the rat lateral amygdala, *J Physiol* 552, 483-497.
22. Hummos A, Nair SS (2017) An integrative model of the intrinsic hippocampal theta rhythm, *PLoS One* 12, e0182648. PMC5546630.
23. Achard P, De Schutter E (2006) Complex parameter landscape for a complex neuron model, *PLoS Comput Biol* 2, e94.
24. Almog M, Korngreen A (2016) Is realistic neuronal modeling realistic?, *J Neurophysiol* 116, 2180-2209.
25. Beniaguev D, Segev I, London M (2021) Single cortical neurons as deep artificial neural networks, *Neuron* 109, 2727-2739.e2723.

Box 1. Implementation of the segregation hypothesis for automated modeling (updated from [10])

User input: Cell type, morphology; neurocomputational properties of interest, e.g., passive properties, current injection responses, oscillatory potentials; known currents; known ranges of parameters

Biological data: If not provided by the user, find the ranges of parameters for each current channel, e.g., maximal conductance, activation/ inactivation functions (see Fig. 1) from biological ranges (e.g., Fig 2.21 in [6], and other sources).

Zones of operation for current modules: The gating kinetics may be available as experimental or mathematical curves. Using a plot of the activation functions of the currents as a function of voltage, estimate the zones of operation for each neuronal signature, to minimize overlap. For instance, the passive module (leak and H) is shown in the area shaded blue in Fig. 1, below the right edge of the blue area. The bursting module currents (Na_p and K_M) activate to the right of the blue area, followed by the spiking module (Na_t and K_{dr}) that activate further to the right as indicated in Fig. 1. The activation functions for currents within the module start at the beginning of the zone for that module. Activation functions of the Boltzmann type will require reshaping the ‘tails’ (shown as dashed lines in Fig. 1) to avoid overlap. In this case we set the value in the dashed region to 0 to avoid overlap. Alternatively, the user can reshape the function to the right to have a smoother rather than abrupt drop as detailed in [10]. Experimental activation curves typically have such sharp cut off already and so these or similar mathematical curves can be used directly. The parameters half-activation voltage $V_{1/2}$ and slope k for each current are then restricted to these ranges, defining their parameter spaces.

Selecting the parameters. With the information above, a semi-automated modeling approach can search over the parameter space of activation kinetics ($V_{1/2}$ and k) and maximal conductance densities or can fix the activation kinetics (as typically performed and done in the present paper) and search only over the space of maximal conductance densities. As a more efficient alternative reported in the present paper, an automated pipeline tunes the segregated modules sequentially, starting with the one furthestmost to the left on the voltage axis, and then progresses (right) to more depolarized levels. For instance, in the example case provided in the present paper of an LA neuron, the approach would follow the sequence: passive module, LTO module, spiking/adaptation module, and HTO module. The procedure has built-in flexibility for the user including decide on the sequence of the modules, select individual ranges for each parameter, and also specify different weighting of the errors for the loss function for each module.

Table 1. Comparison of errors (%) between user data and predictive model developed using *original* and *segregated* pipelines

Cell/Properties	Error in passive properties (%)		Error in F-I curve		Other properties – LTO/HTO	
	Original	Segregated	Orig.	Seg.	Original	Segregated
	Vrest, Rin, Tau	Vrest, Rin, Tau				
1. Hipp Burster-1	-2.04%, 4.17%, -16.57%	0,0,0	6.4	2.4	N/A	N/A
2. Hipp Burster-2	11.36%, -64.98%, -67.78	0,0,0	7.2	2.0	N/A	N/A
3. Amygdala spiker	-0.47%, -34.78%, -41.06	0,0,0	5.4	2.4	Absent	Present
4. Amygdala adaptive	0.91%, -44.68%, 48.83	0,0,0	1.6	1.6	Absent	Present

Table 2. Parameter values of estimated current channel parameters for the four example cases

	Example case 1 Burster - 1	Example case 2 Burster - 2	Example case 3 Tonic spiker with 4 properties	Example case 4 Adapting with 4 properties
V-rest (mv)	-75	-49	-70	-70
Input Resistance (MΩ)	260	90	141	141
Time Const. (ms)	102	43	31	31
Cm (μF/cm²)	2.5	1	2.5	2.5
R_a (Ωcm)	200	35.4	200	200
Conductance (S/cm²)				
gNabar	0.03	0.13	0.03	0.03
gKdrbar	0.028	0.01	0.009	0.03
gLeak	3.5E-05	4.0E-05	4.0E-05	3.5E-05
gNapbar	0.0003	--	0.00014	0.0003
gHdbar	--	--	2.3E-05	2.3E-05
gCabbar	--	--	7.0E-5	6.0E-5
gMbar	0.0033	--	0.001	0.002
gsAHPbar	--	--	0.00025	0.009
gKapbar	--	0.17	0.000843	0.000843
gNat	--	--	--	--
gKCabar	--	0.02	--	--
gCasbar	--	0.01	--	--
gCatbar	--	0.005	--	--
gCal	--	--	--	--

Table 3. Kinetics of the currents in the various example cases

Current	Gating Variable	α	β	x_∞	$\tau_x (\text{ms})$
I_{Na}^1	$p=3$	$\frac{-0.4(V+30)}{\exp[-(V+30)/7.2]-1}$	$\frac{0.124(V+30)}{\exp[(V+30)/7.2]-1}$	$\frac{\alpha}{\alpha+\beta}$	$\frac{0.6156}{\alpha+\beta}$
	$q=1$	$\frac{-0.03(V+45)}{\exp[-(V+45)/1.5]-1}$	$\frac{0.01(V+45)}{\exp[(V+45)/1.5]-1}$	$\frac{1}{\exp[(V+50)/4]+1}$	$\frac{0.6156}{\alpha+\beta}$
I_{Kdr}^1	$p=1$	$\exp[-0.1144(V+15)]$	$\exp[-0.0801(V+15)]$	$\frac{1}{\exp[(-V-15)/11]+1}$	$\frac{50*\beta}{1+\alpha}$
I_H^2	$q=1$	$\exp[0.0832(V+75)]$	$\exp[0.0333(V+75)]$	$\frac{1}{\exp[(V+81)/8]+1}$	$\frac{\beta}{0.0081(1+\alpha)}$
I_{KM}^3	$p=2$	$\frac{0.016}{\exp[-(V+52.7)/23]}$	$\frac{0.016}{\exp[(V+52.7)/18.8]}$	$\frac{1}{\exp[(-V-52.7)/10.3]+1}$	$\frac{1}{\alpha+\beta}$
I_{Ca}^3	$p=2$	—	—	$\frac{1}{\exp[(-V-30)/11]+1}$	$\frac{2.5}{\exp\left[\frac{-(V+37.1)}{32.3}\right]+\exp\left[\frac{(V+37.1)}{32.3}\right]}$
	$q=1$	—	—	$\frac{1}{\exp[(V+12.6)/18.9]+1}$	420
I_{Nap}^4	$p=1$	—	—	$\frac{1}{\exp[(-V-48)/5]+1}$	$2.5 + 14 * \exp[- V+40 /10]$
I_{sAHP}^3	$p=1$	$\frac{0.0048}{\exp[-5\log_{10}([Ca]_{i2})-17.5]}$	$\frac{0.012}{\exp[2\log_{10}([Ca]_{i2})+20]}$	$\frac{\alpha}{\alpha+\beta}$	48
$I_{Na1.2}^5$	$p=3$	$\frac{-0.182(V+30)}{\exp[-(V+30)/7]-1}$	$\frac{0.124(V+30)}{\exp[(V+30)/7]-1}$	$\frac{\alpha}{\alpha+\beta}$	$\frac{1}{\alpha+\beta}$
	$q=1$	$\frac{-0.024(V+50)}{\exp[-(V+50)/5]-1}$	$\frac{0.0091(V+75)}{\exp[(V+75)/5]-1}$	$\frac{1}{\exp[(V+72)/6.2]+1}$	$\frac{1}{\alpha+\beta}$
$I_{Na1.6}^5$	$p=3$	$\frac{-0.182(V+43)}{\exp[-(V+30)/6]-1}$	$\frac{0.124(V+43)}{\exp[(V+30)/6]-1}$	$\frac{\alpha}{\alpha+\beta}$	$\frac{1}{\alpha+\beta}$
	$q=1$	$\frac{-0.024(V+50)}{\exp[-(V+50)/5]-1}$	$\frac{0.0091(V+75)}{\exp[(V+75)/5]-1}$	$\frac{1}{\exp[(V+72)/6.2]+1}$	$\frac{1}{\alpha+\beta}$
I_{NaT}^6	$p=3$	$\frac{Ra(V+15)}{1-\exp[-(V+15)/7.2]}$	$\frac{Rb(-V-15)}{1-\exp[-(-V-15)/7.2]}$	$\frac{\alpha}{\alpha+\beta}$	$\frac{1}{\alpha+\beta}$
	$q=1$	$\frac{Rd(V+30)}{1-\exp[-(V+30)/1.5]}$	$\frac{Rg(-V-30)}{1-\exp[-(-V-30)/1.5]}$	$1 + \frac{1}{\exp[(V+35)/4]}$	$\frac{1}{\alpha+\beta}$
I_{CaL}^6	$p=2$	$\frac{15.69(-V+81.5)}{\exp[-(V+81.5)/10]-1}$	$0.29 * \exp[-\frac{V}{10.86}]$	$\frac{\alpha}{\alpha+\beta}$	$\frac{1}{\alpha+\beta}$

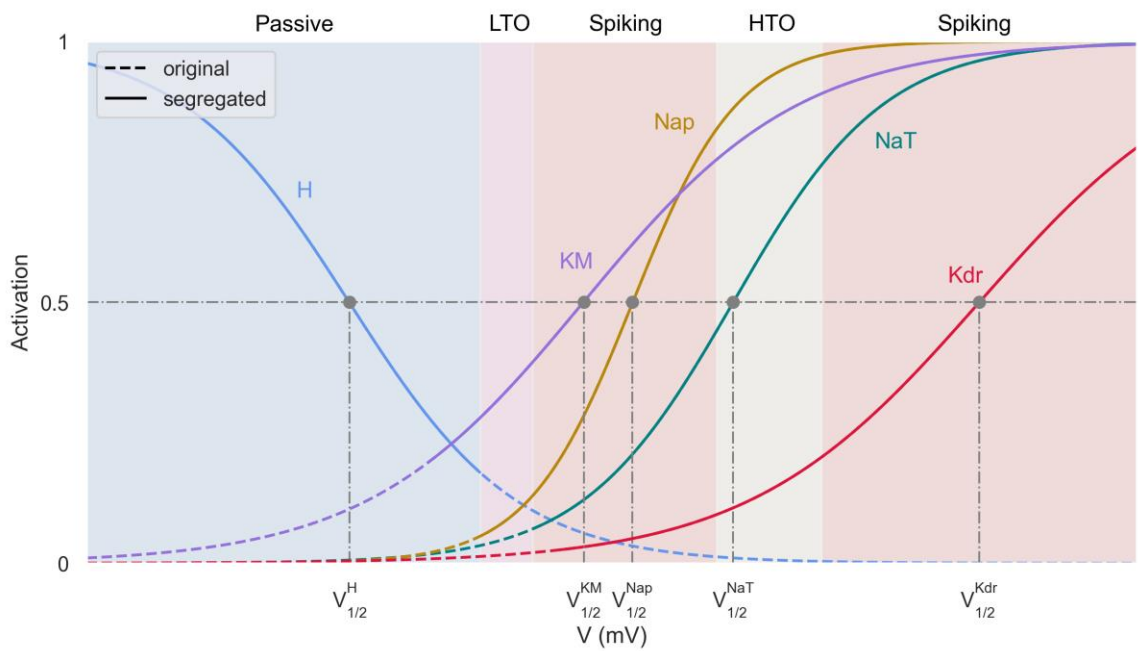


Figure 1. Cartoon illustrating segregation of currents into three modules for example case 1 of burster neuron – passive (leak, H), adapting/ bursting (Nap, KM) and Spiking (Nat, Kdr)

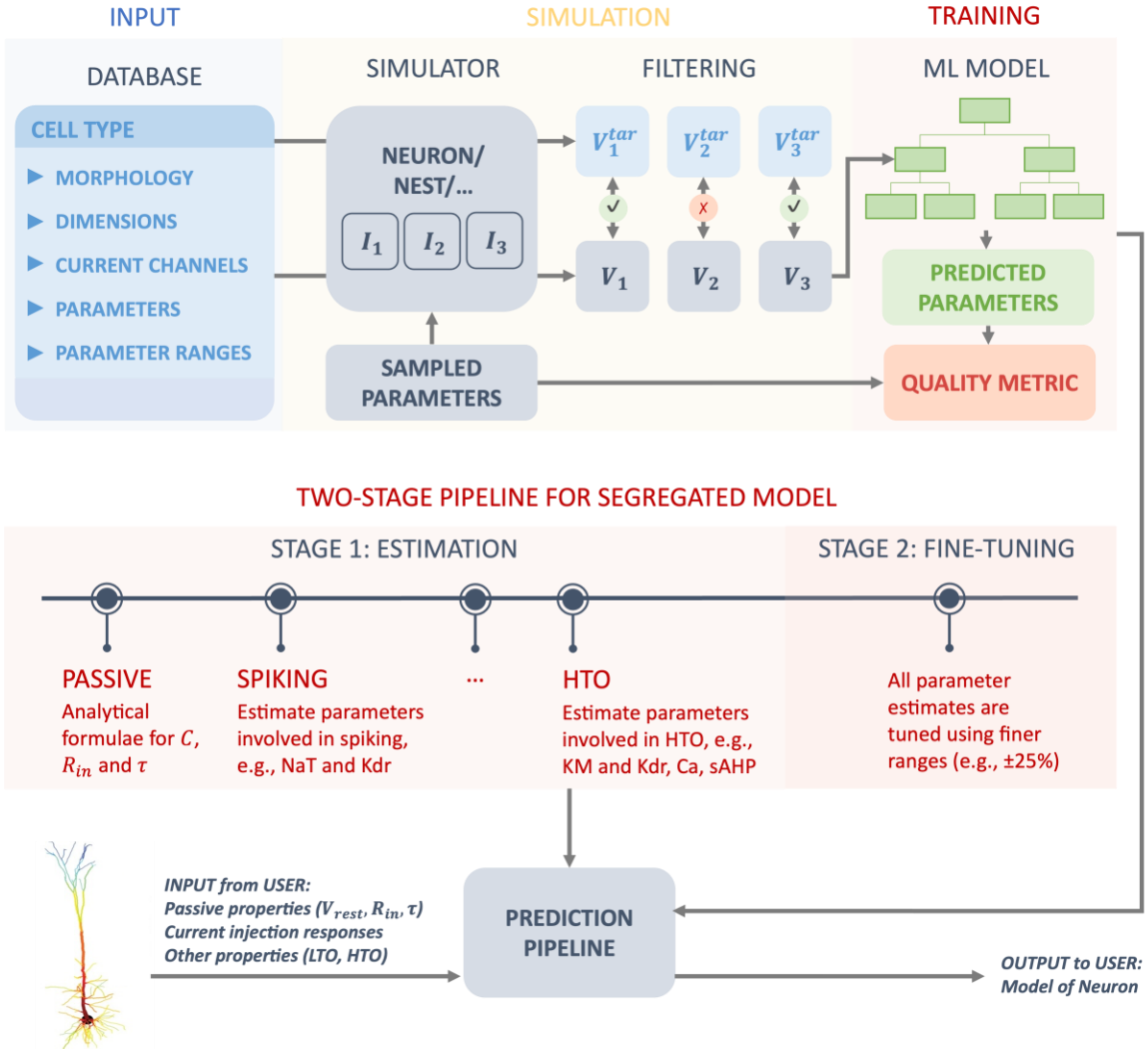


Figure 2. Schematic of the two ACT prediction pipelines. The first pipeline has only one stage of tuning and is represented in the top part of the figure. With user input about the cellular characteristics, a complete set of features for the model cell is assembled by supplementing user input from a library (see box titled ‘Database’). This is fed to the simulator which then randomly selects parameters and generates training data for the full cell model and produces the estimator-*original* which uses the ML model to predict the parameters given the voltage traces (see methods). The second pipeline performs the prediction of neuronal parameters in two stages: in stage 1, a coarse prediction of parameters is done module by module, starting with the passive, spiking, etc. modules, and the stage 1 predictions are assembled to then predict all the parameters in stage 2 which implements fine tuning. The parameters are then used to develop the model of the neuron in the software preferred by the user.

Spiking with Bursting

FI Curve

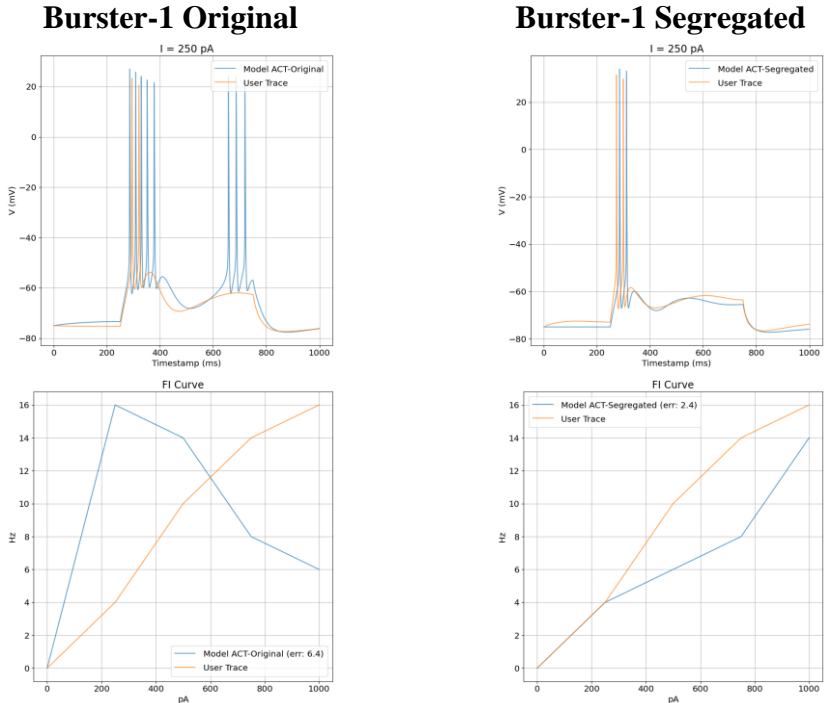


Figure 3. Comparisons between predicted models from the two pipelines for example case 1 (Burster-1) with 5 channels – leak, Nap, KM, Nat, Kdr.

Spiking with Bursting

FI Curve

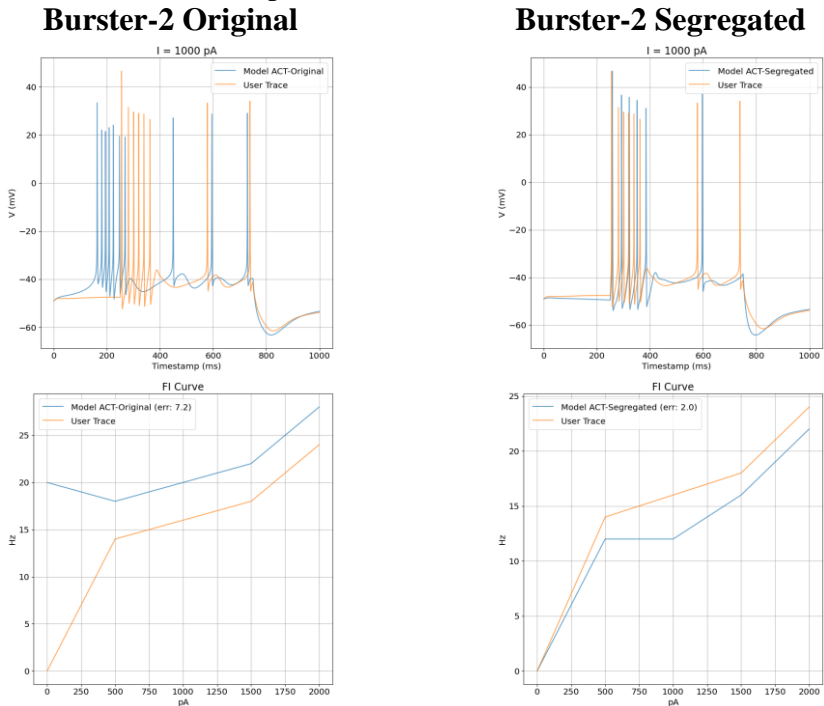


Figure 4. Comparisons between predicted models from the two pipelines for example case 2 (Burster-2) with 6 channels – Leak, CaS, CaT, sAHP, Nat, Kdr.

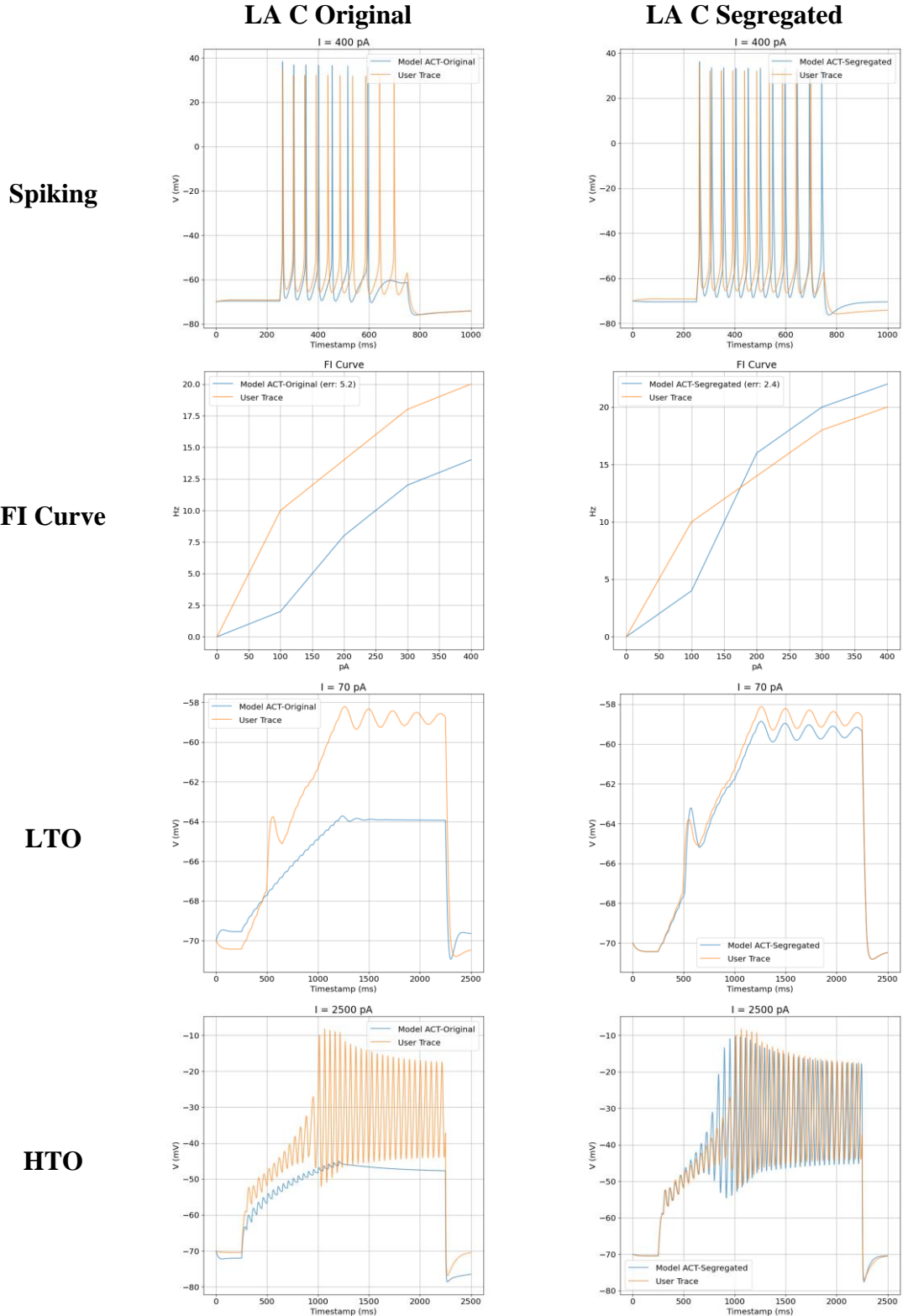


Figure 5. Comparisons between predicted models from the two pipelines for example case 3 (tonic spiker with oscillatory potentials) – type C pyramidal neuron in the rodent lateral amygdala.

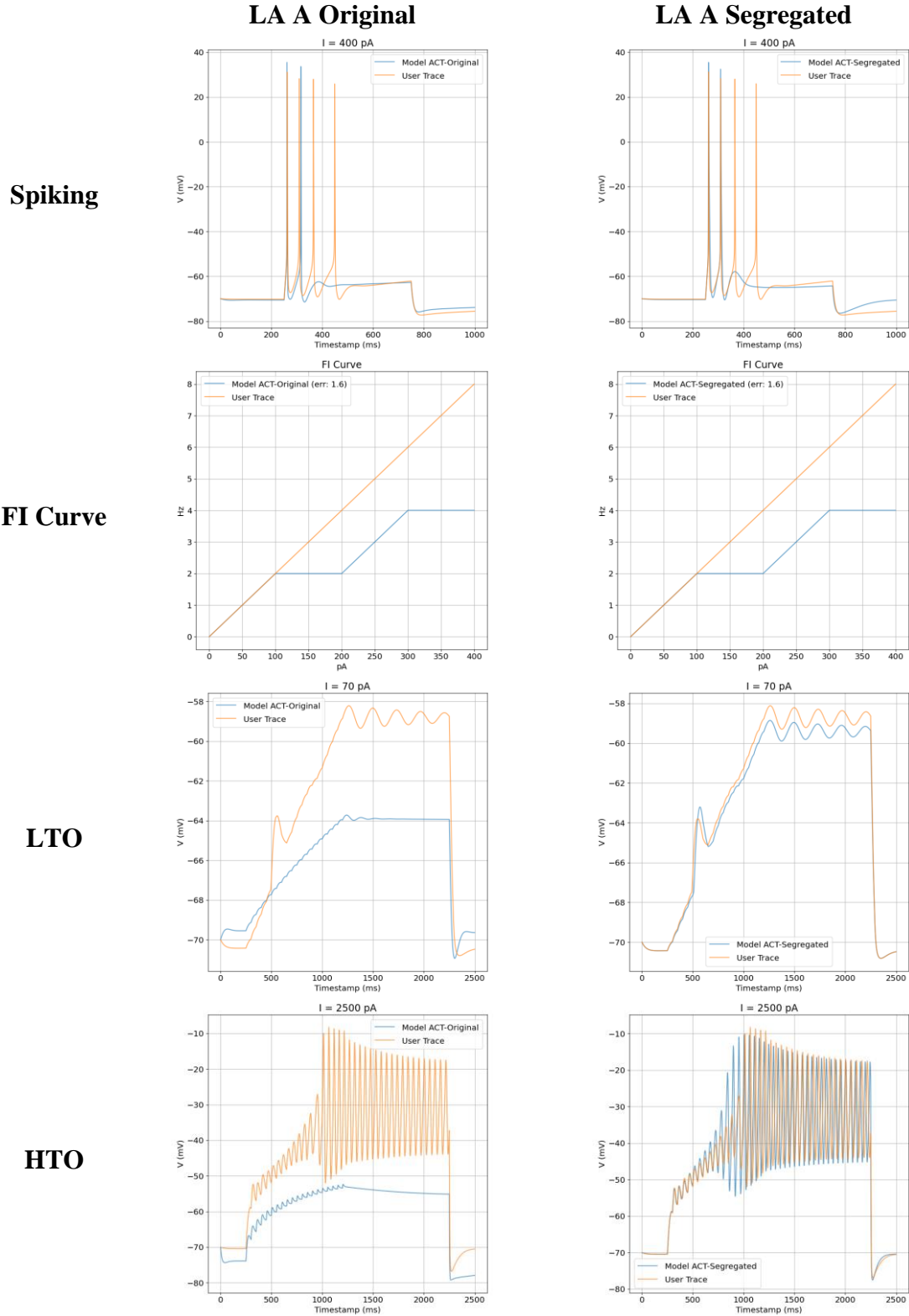


Figure 6. Comparisons between predicted models from the two pipelines, for example case 4 (highly adaptive cell with oscillatory potentials) – type A pyramidal neuron in the rodent lateral amygdala.

CHAPTER 5 – SUMMARY, CONTRIBUTIONS, AND FUTURE

WORK

SUMMARY

Here we have presented three studies that demonstrate the utility of modeling in both the machine learning and computational neuroscience spaces to address hypotheses in several systems at various levels of detail.

CHAPTER 2

In Chapter 2, our results point to modifiable prescribing behavior as the key contributor to OUD. Replication in other healthcare systems is needed and comparisons to data driven models warranted. Overall, results hold promise that machine learning models can reasonably predict OUD and could be incorporated in the electronic health record as a clinical decision aid.

Future work:

- Further research is needed to compare the utility of predictive algorithms that are completely data driven and those that are developed with user input.

CHAPTER 3

In Chapter 3, we developed a biophysical model of the rodent amygdala to explore the genesis of the theta rhythm.

We show that GABAergic VP/SI input should strengthen the theta-range oscillatory power albeit sufficient network resonance arising from thalamic/cortical and BF cholinergic input. However, when these excitatory inputs fail to produce theta-genesis, GABAergic afferents may provide no additional effect. Intrinsic oscillatory mechanisms in the model included the PN-SOM+ and PN-CR+ cell loops. Our results show that this

mechanism is indeed capable of increasing power in the theta range as reflected in the PSD plot of the LFP. While cholinergic modulation is thought to further strengthen resonance in these cell loops and contribute to the theta-frequency oscillation in the BLA, the extrinsic GABAergic projection from VP/SI provides an independent, possibly overarching resonant mechanism. Although there should be sufficient resonance in the network arising from non-rhythmic thalamic/cortical and modulatory cholinergic input, GABAergic VP/SI input should strengthen the theta-range oscillatory power.

However, when these non-rhythmic excitatory inputs fail to produce theta-genesis in the BLA, GABAergic afferents may provide no additional effect, as in the hippocampus.

Future work:

- The present network contained 1000 cells, which was scaled down from the estimated 27,000 in the BLA. By scaling the network up, the assertions made can be further validated.

CHAPTER 4

In Chapter 4, we developed and utilized the Automated Cell Tuner (ACT).

Future work:

- Additional improvements to the pipeline should increase predictive ability. Improvements could include changing the training data resolution on a per-conductance basis, implementing additional machine learning algorithms or extracting other summary features.
- Development for this software is ongoing and will be supported for the foreseeable future.

PUBLICATIONS

Refereed Journal and Conference Articles

- Banks T, Scherrer J, Tung T, Uhlmann J, Nair SS (2023) Predicting opioid use disorder before and after the opioid prescribing peak in the United States: a machine learning tool using electronic healthcare records, *Health Informatics Journal* Apr-Jun; 29(2): 14604582231168826. doi: 10.1177/14604582231168826
- Tuna T#, Banks T#, Glikert G, Sevinc C, Nair SS, Unal G, “Anatomical and Computational Investigation of Basal Forebrain Innervation of the Amygdala” (to be submitted to *Brain Structure and Function*)
- Banks T, Vladimir (Walt) Omelyusik, Nair S, “ACT Automated Cell Tuner – Pipeline for Biophysical Modeling of a Large Class of Neurons” (Manuscript fully drafted)
- Opsal N, Canfield P, Banks T, Nair S, “An Efficient Pipeline for Biophysical Modeling of Neurons,” IEEE EMBS Conference on Neural Engineering (NER’21), 4-page peer-reviewed paper, May 4-6, 2021

Posters and Presentations

- Banks T, Tuna T, Canfield P, Unal G, Nair SS “**Model of the Generation of the Amygdala Theta Rhythm**” IEEE EMBS Conference on Neural Engineering (NER’21), Poster, May 4-6, 2021
- Banks T, Guntu V, Hummos A M, Nair S, “**Resonant and synchronizing mechanisms in a hippocampal theta model,**” Japan Neuroscience Society Presentation and Poster, Kobe, Japan, Jul 31, 2020
- Wei Q, Banks T, Latimer B, Chen Z, Nair S, “**Automating development of biophysical single cell models**” Society for Neuroscience Poster, Chicago, IL, Oct 21, 2019
- Nair S, Banks T, Latimer B, Chen Z, Lyu Z, Chen Z, Dopp D, Fotoohighiam A, Calyam P, Joshi T, Xu D, “**Software automation for research and training in neural engineering,**” Society for Neuroscience Poster, Chicago, IL, Oct 21, 2019
- Banks T, Guntu V, Hummos A M, Nair S, “**Characterizing resonant and synchronizing mechanisms in a hippocampal theta model,**” Society for Neuroscience Poster, Chicago, IL, Oct 20, 2019
- Dopp D, Banks T, Samarath P, Kick D, Schulz D, Nair S, “**Detailed biologically realistic model of a crustacean cardiac ganglion network,**” Society for Neuroscience Poster, Chicago, IL, Oct 20, 2019
- Latimer B, Banks T, Gahl M, Guntu V, Schulz D, Nair S, “**Computational modeling of the neural circuit of rodent lower urinary tract,**” Society for Neuroscience Poster, Chicago, IL, Oct 19, 2019

- Latimer B, Chen Z, Banks T, Ho D, V Kanta Chantzi, D B Headly, D Pare, Nair SS, “**Artificial neural networks for prediction of the local field potential,**” Society for Neuroscience Poster, San Diego, Ca, Nov 7, 2018.
- Banks T, Wang J, Samarth P, Kick D, Schulz DJ, Nair SS, “**Structure of large cells in crab cardiac ganglion - a computational study,**” Society for Neuroscience Poster, San Diego, Ca, Nov 5, 2018.
- Latimer B, Banks T, Ankathatti A, Calyam P, Nair SS, “**Software automation for biologically realistic neuro big data simulations,**” Big Data Neuroscience Workshop: Organized by the Advanced Computational Neuroscience Network (ACNN), Cleveland, OH, Sept 6-7, 2018
- Banks T “**CNN-Fold: Protein Fold Recognition by Deep Convolutional Neural Networks**”, Unpublished Master Thesis Project, University of Missouri, Columbia, Missouri, May 2016